UNIVERSITY OF CALIFORNIA SAN DIEGO

Tools to investigate composite receptive fields in songbird auditory region

A dissertation submitted in partial satisfaction of the
requirements for the Degree Doctor of Philosophy

in

Electrical Engineering (Medical Devices and Systems)

by

Nasim Winchester Vahidi

Committee in charge:

Professor Timothy Q. Gentner, Chair
Professor Shadi A. Dayeh, Co-Chair
Professor Duygu Kuzum
Professor Tina Ng
Professor Donald J. Sirbuly

2019

The Dissertation of Nasim Winchester Vahidi is approved, and it is acceptable in quality and form for publication on microfilm and electronically:

_____

_____

_____

_____
Co-Chair

_____
Chair

University of California San Diego

2019

DEDICATION

This thesis is dedicated to:

My great parents, Nabi and Jamileh, who never stop giving of themselves in countless ways and their inspiration and constant love have sustained me throughout my life.

My beloved husband, Shannon, whose unconditional support and encouragement makes this scientific work to be what it is today.

My dear brothers, Pedram and Daniel, who inspired me and have stood by me through years of study.

My beloved son, Sasha, whose hugs and love energized me and assured me I am on the right path.

To all my family whom always are there for me with patience and love.

To my friends whose conversations, laughter, and coffee sustained me throughout the entire doctorate program.

Finally, this thesis is dedicated to all those who believe in the richness of learning.

EPIGRAPH

"Everything we do, every thought we've ever had, is produced by the human brain. But exactly how it operates remains one of the biggest unsolved mysteries, and it seems the more we probe its secrets, the more surprises we find"

-Neil deGrasse Tyson

TABLE OF CONTENTS

LIST OF TABLES

LIST OF FIGURES

ACKNOWLEDGEMENTS

Foremost, I would like to thank my PhD advisor, Dr. Timothy Gentner for support of my Ph.D study and research, for his patience, motivation, and immense knowledge.

I would also like to acknowledge my co-advisor, Dr. Shadi Dayeh, for his guidance, encouragement, and insightful comments throughout my study.

Besides my advisers, I would like to express my sincere gratitude to Dr. Yu-Hwa Lo who initially guided me to begin my doctoral degree.

I would like to acknowledge my committee members Dr. Duygu Kuzum , Dr. Tina Ng, and Dr. Donald Sirbuly for their supervision and advice.

Also, I would like to acknowledge my Master researcher advisor, Dr. Sam Kassegne at San Diego State University, for instilling me with a strong passion for learning and research.
I thank all my lab-mates for their intuitive comments and support especially Marvin Thielk.

Chapter 2, in full, is in preparation for publication as: Nasim W. Vahidi., and Timothy Q. Gentner. “Neural population coding by composite receptive fields in songbird auditory region”. The dissertation author was the primary investigator and author of this manuscript.

Chapter 3, in full, is in preparation for publication as: Mehran Ganji, Angelique C. Paulk, Jimmy C. Yang, Nasim W. Vahidi, Sang Heon Lee, Ren Liu, Lorraine Hossain, Ezequiel M. Arneodo, Martin Thunemann, Michiko Shigyo, Atsunori Tanaka, Sang Baek Ryu, Seung Woo Lee, Martin Marsala, Anna Devor, Daniel Cleary, Vikash Gilja, Timothy Q. Gentner, Shelly I. Fried, Eric Halgren, Sydney S. Cash, and Shadi A. Dayeh. “Selective Formation of Porous Pt Nanorods for Highly Electrochemically Efficient Neural Electrode Interfaces”. The dissertation author was the co-primary investigator of this chapter.

Chapter 4, in full, is a reprint of materials as it appears in Elisa Castagnola, Nasim W.Vahidi, Surabhi Nimbalkar, Srihita Rudraraju, Marvin Thielk, Elena Zucchini, Claudia Cea, Stefano Carli, Timothy Q. Gentner, Davide Ricci, Luciano Fadiga, and Sam Kassegne (2018). "In Vivo Dopamine Detection and Single Unit Recordings Using Intracortical Glassy Carbon Microelectrode Array" *in MRS Adv.3,* p. 1629–1634, doi:10.1557/adv.2018.98. The dissertation author was the co-primary author of this paper.

Chapter 5, in full, is in preparation for publication as: Nasim W.Vahidi, Surabhi Nimbalkar, Elisa Castagnola, Srihita Rudraraju, Claudia Cea , Shadi A. Dayeh, Timothy Q. Gentner, and Sam Kassegne. "Epi-Intra device with glossy carbon electrodes: A tool for neural coding". The dissertation author was the primary investigator and author of this manuscript.

VITAE

2000	Bachelor of Science in Biomedical Engineering (Bioelectric), Shariati-Azad University, Tehran, Iran
1999-2000	Medical device quality control and repair, Alipayam Co., Tehran, Iran
2000-2001	Electronics lab instructor, University of Abhar, Iran
2000-2006	Business entrepreneur and owner, Managing Director, Nasim Shargh Medical devices Co. Ltd., Tehran, Iran
2008-2009	Research associate, Cardiac Mechanics, University of California San Diego
2011	Master of Science in Bioengineering (Bio-MEMS), San Diego State University
2011-2012	Product development Intern, NxGen Electronics and Lumedyne Technologies.
2011-2013	Research associate, Neural probes, San Diego State University
2013-2019	Research assistant, Neuroscience, University of California San Diego
2019	Doctor of Philosophy in Electrical Engineering (Medical Devices and Systems), University of California San Diego

PUBLICATIONS

Castagnola, E., Vahidi, W. N., Nimbalkar, S., Rudraraju, S., Thielk, M., Zucchini, E., Kassegne, S., 2018, . In Vivo Dopamine Detection and Single Unit Recordings Using Intracortical Glassy Carbon Microelectrode Array. MRS Adv.3, 1629–1634

Vahidi, W. N., Hirabayashi, M., Mehta, B, Khosla, A., and Kassegne, S., 2014, Bionanoelectronics Platform with DNA Molecular Wires Attached to High Aspect-Ratio 3D Metal Microelectrodes, ECS Journal of Solid State Science and Technology 3 (3), Q29-36 2014.

Vahidi, W. N., McDowell, T., and Kassegne, S., 2013, Carbon-MEMS Based Multi-Site Electrode Array Fabric for Neural Sensing & Recording, 224th ECS Meeting, San Fran., CA.

Hirabayashi, M., Mehta, B., Vahidi, N., Khosla, A., and Kassegne, S., 2013, Functionalization and Characterization of Pyrolyzed Polymer Based Carbon Microstructures for Bionanoelectronics Platform, Journal of Micromechanics and Microengineering, 23(11), 115001.

Vahidi, W.N., 2010, Electrical Characterization of Three Dimensional DNA-Based Bionanoelectronics Platforms. Masters' Thesis, San Diego state university, 141p.

ABSTRACT OF THE DISSERTATION

Tools to investigate composite receptive fields in songbird auditory region

by

Nasim Winchester Vahidi

Doctor of Philosophy in Electrical Engineering (Medical Devices and Systems)

University of California San Diego, 2019

Professor Timothy Q. Gentner, Chair

Professor Shadi A. Dayeh, Co-Chair

Neural coding is primarily concerned with characterizing the relationship between stimulus and neuronal responses and is classified to stimuli encoding and brain response decoding. Although there are existing models for neural coding, most are not sophisticated enough to describe the relationship of population of neural responses to natural stimuli such as human speech

or bird songs. In this study we propose utilizing composite receptive fields (CRF) as a new tool for neural coding. CRFs are quadratic receptive fields which are built from mutual information between stimuli and related brain responses. Here we create a pool of 3080 CRFs from a population of 154 cells recorded from the brain auditory region of European starling songbirds. Following, this pool of CRFs is used to build a spatial-temporal map for the population of cells along the brain coronal plane in respect to bird song stimuli. This map has revealed novel information about the relationship between neural responses and related stimuli such as: 1) Natural sound stimuli can be encoded by populations of neurons. 2) The number of cells needed to encode the stimuli can be quantified. 3) Stimuli encoding mechanisms of the brain appeared to be uniform and independent of cells' topology and their locations. 5) From this map, connectivity between cells as well as their response plasticity to diverse stimuli were observed. 6) CRFs were used as intermediate tools to reconstruct stimuli and predict brain responses. These results have confirmed that quadratic receptive fields can be a novel candidate for population neural coding. Testing neural coding by CRFs was originally performed on cells recorded from the brain coronal depth plane. We expanded this coding method and evaluated CRFs mapping on cells recorded from two novel in-house fabricated electrodes: a surface electrode and a combination of surface and depth electrodes. The CRFs extracted from cells recorded by these electrodes can be employed to create a 2D and 3D spatial-temporal map which is useful to explore neural information distribution and their perception mechanisms from deep brain to cortical surface. Furthermore, the CRF neural coding method and the brain implants described in this study have potentials to be used in BCI prosthetics.

CHAPTER 1

Introduction to the Dissertation

1.1 General scope and outline of the dissertation

Neural coding is the study of information processing by neurons. Such study seeks to explain the type of information and mechanism of information transmission and perception throughout the brain. Neural coding can be categorized into two interconnected mechanisms: stimuli encoding and brain response decoding (Koyama S. , 2012). Stimuli encoding is referred to as mapping stimuli to brain response and is primarily used to reconstruct stimuli from neural responses (Mesgarani, 2009) . The phenomena of stimuli reconstruction is a vital step towards creating a new memory by neurons (Baddeley, 2009). On the other hand, neural decoding is a reverse mapping that maps and reconstructs brain response from stimuli and has applications related to Brain Computer Interface (BCI) and brain response prediction (Taylor, 2002).

There are exciting models for neural coding such as spike rate coding (Adrian, 1926), spike time coding (Dayan & Abbott, 2001), or local field potential (LFP) coding (Lowet, 2018). These tools provided a wealth amount of information about neural coding although there are limitations associated with them. Spike rate concept which is based on temporal averaging is not sophisticated enough to describe brain activity (Stein, 2004). On the other hand, temporal coding usually treats each spike independent from the others which makes the model weak when analyzing populations of neurons. Furthermore, in this study we have shown that although LFPs contain a great amount of information about underlying neural activities and brain responses in general, correlations between them do not hold for large distance between recording sites. Similar finding have been reported in other studies ((Destexhe, 1999) & (Bedard, 2004)).

To overcome these limitations, **in chapter 2**, we propose utilizing composite receptive field (CRF) as a new tool for neural coding. The receptive field of a cell in a sensory system is the area of the periphery whose stimulation impacts the response of a sensory nerve cell (Sherrington,

1960). In this study we concentrate on auditory receptive fields recorded from the auditory region of European starling bird brains. Auditory receptive field refers to the region in auditory space where a sound can evoke a neuronal response. The sensory organs in the auditory system is the cochlea. The hair cells in cochlea are stimulated by sound waves and detect sound frequencies (Mann, 2014).

Some examples of broadly used models to generate receptive fields are spike trigger average (STA) to build STRFs (Spatio-temporal receptive fields) ((Aertsen, 1981), (DeAngelis, 1995), (De Boer & Kuyper, 1968), (Gosselin, 2002), (Arun, 2006)) , spike-triggered covariance (STC) (Schwartz, 2002), and maximally informative dimensions (MID) (Sharpee, 2004). These models, although offering rich information about receptive fields, suffer from a number of drawbacks such as inability to characterize nonlinear information of stimuli (Thunissen, 2000), limitation working with natural stimuli e.g. human speech and bird song ((Schwartz, 2006) & (Eggermont, 1983b)), and limitation identifying large numbers of relevant receptive field features (Kozlov & Gentner, 2016).

A complimentary model to these models, Maximum Noise Entropy (MNE), utilized in this study, overcomes most of these limitations ((Fitzgerald, 2011a), (Sharpee, 2004) , and (Bialek, 2006)). The MNE model looks for mutual information between audio stimuli and the brain responses in the form of CRFs. Recently, we have shown that neurons in the auditory region of starling songbirds have CRFs with various acoustic features which drive increases and decreases in their firing rate (Kozlov & Gentner, 2016). Here in this study we have recorded populations of cells from the NCM auditory region of five birds via commercial depth electrodes and subsequently utilized the MNE model to extract a large pool of CRFs from multiple populations of cells. These large pools of CRFs then were used to create spatial-temporal maps in respect to

birdsong stimuli.

From the spatial-temporal map we inferred novel information such as natural sound stimulus not only can be encoded by populations of neurons, but also the number of cells needed to encode the stimulus can be quantified. Furthermore this encoding mechanism and consequently perception of natural sound by the brain appeared to be uniform and independent of cell locations and their topology. Moreover, through this map, connectivity between cells as well as their plasticity in response to diverse stimuli was observed. Additionally, we proved CRFs can be used as intermediate tools to reconstruct stimuli and predict brain response.

In chapter 2 we investigate spatial-temporal maps of CRFs from cells recorded from deep brain by commercial electrodes. Inspired by this map, we further scrutinized neural coding, propagation, and distribution mechanism of CRFs across this coronal plane. In **chapter 3**, we introduce a novel surface array for a similar investigation to chapter 2. This in-house fabricated surface array is made of a highly pliable parylene C substrate with embedded recording sites made of platinum nanoscale rods (PtNR). Through this study we demonstrated PtNRs are biocompatible, robust, and minimally invasive. Analyzing electrical recordings from this new ECOG surface array have shown this device is capable of capturing cell action potentials from the cortical surface as well being able to generate CRFs from these captured cells. This creates an opportunity to generate a spatial-temporal CRFs map of cells on the brain surface to study information distribution and propagation mechanisms on the cortical surface (horizontal plane).

These results encouraged us to investigate neuron data distribution mechanisms in horizontal and coronal planes simultaneously by combing a surface array with a depth shank. **In chapter 5**, we introduce this novel electrode combination (Epi-Intra). The Epi-Intra device contained homogenous recording sites made of glassy carbon (GC) on both flexible surface array

and on its reinforced depth shank. GC sites are chemically inert, biocompatible, and have low impedance ((Vomero, 2017) & (Goshi, 2018)).

In chapter 4, we demonstrate the GC sensing sites not only have great potential to record high fidelity, low noise signals from bird brain, but also are able to clearly record neurotransmitters such as dopamine (Castagnola, 2018).

Continuing in **chapter 5**, by analyzing electrical recordings via the Epi-Intra device, we demonstrate this device has potential to record high quality stimulus-locked cells simultaneously from cortical surface and deep brain regions. The pool of CRFs extracted from these cells can be used to create a 3D spatial-temporal map which covers a volume of tissue from cortical surface to deep brain.

Ultimately, a 2D CRF map of the cortical surface or deep brain as well as a 3D CRF map from a combination of surface and depth electrodes, offer great potential for neural coding and investigating information distribution mechanisms from deep brain to cortical surface and vice versa. Furthermore, the novel devices discussed in this study have potential for chronic implants and recordings and consequently can be used as BCI prosthetics.

1.2 References

Adrian, E. D., & Zotterman, Y. (1926). The impulses produced by sensory nerve-endings: Part II. The response of a Single End-Organ. *The Journal of Physiology*, *61*(2), 151. Retrieved from https://www.ncbi.nlm.nih.gov/pmc/articles/PMC1514782/

Aertsen, A. M., & Johannesma, P. I. (1981). The spectro-temporal receptive field. A functional characteristic of auditory neurons. *Biological Cybernetics*, *42*(2), 133–143. Retrieved from http://www.ncbi.nlm.nih.gov/pubmed/7326288

Baddeley, A. (2013). *Essentials of Human Memory (Classic Edition)*. https://doi.org/10.4324/9780203587027

Bédard, C., Kröger, H., & Destexhe, A. (2004). Modeling extracellular field potentials and the frequency-filtering properties of extracellular space. *Biophysical Journal*, *86*(3), 1829–1842. https://doi.org/10.1016/S0006-3495(04)74250-2

Bialek, W., De Ruyter Van Steveninck, R. R., & Tishby, N. (2006). Efficient representation as a design principle for neural coding and computation. *2006 IEEE International Symposium on Information Theory*, 659–663. https://doi.org/10.1109/ISIT.2006.261867

Castagnola, E., Winchester Vahidi, N., Nimbalkar, S., Rudraraju, S., Thielk, M., Zucchini, E., … Kassegne, S. (2018). In Vivo Dopamine Detection and Single Unit Recordings Using Intracortical Glassy Carbon Microelectrode Arrays. *MRS Advances*, *3*(29), 1629–1634. https://doi.org/10.1557/adv.2018.98

Dayan, P., & Abbott, L. F. (2001). *Theoretical neuroscience : computational and mathematical modeling of neural systems*. Massachusetts Institute of Technology Press.

DeAngelis, G. C., Ohzawa, I., & Freeman, R. D. (1995). Receptive-field dynamics in the central visual pathways. *Trends in Neurosciences*, *18*(10), 451–458. https://doi.org/10.1016/0166-2236(95)94496-R

Destexhe, A., Contreras, D., & Steriade, M. (1999). Spatiotemporal analysis of local field potentials and unit discharges in cat cerebral cortex during natural wake and sleep states. *The Journal of Neuroscience : The Official Journal of the Society for Neuroscience*, *19*(11), 4595–4608. Retrieved from http://www.ncbi.nlm.nih.gov/pubmed/10341257

Eggermont, J. J., Epping, W. J. M., & Aertsen, A. M. H. J. (1983). Stimulus dependent neural correlations in the auditory midbrain of the grassfrog (Rana temporaria L.). *Biological Cybernetics*, *47*(2), 103–117. https://doi.org/10.1007/BF00337084

Fitzgerald, J. D., Rowekamp, R. J., Sincich, L. C., & Sharpee, T. O. (2011). Second Order Dimensionality Reduction Using Minimum and Maximum Mutual Information Models. *PLoS Computational Biology*, *7*(10), e1002249. https://doi.org/10.1371/JOURNAL.PCBI.1002249

Fitzgerald, J. D., Sincich, L. C., & Sharpee, T. O. (2011). Minimal Models of Multidimensional Computations. *PLoS Computational Biology*, *7*(3), e1001111. https://doi.org/10.1371/journal.pcbi

Goshi, N., Castagnola, E., Vomero, M., Gueli, C., Cea, C., Zucchini, E., … Fadiga, L. (2018). Glassy carbon MEMS for novel origami-styled 3D integrated intracortical and epicortical neural probes. *Journal of Micromechanics and Microengineering*, *28*(6), 065009. https://doi.org/10.1088/1361-6439/aab061

Gosselin, F. S. (2002). *Learning and memory : a comprehensive reference*. *Trends Cog.*

Koyama, S. (2012). On the Relation Between Encoding and Decoding of Neuronal Spikes.

Neural Computation, *24*(6), 1408–1425. https://doi.org/10.1162/NECO_a_00279

Kozlov, A. S., & Gentner, T. Q. (2016). Central auditory neurons have composite receptive fields. *Proceedings of the National Academy of Sciences*, *113*(5), 1441–1446. https://doi.org/10.1073

Lowet, E., Gips, B., Roberts, M. J., De Weerd, P., Jensen, O., & van der Eerden, J. (2018). Microsaccade-rhythmic modulation of neural synchronization and coding within and across cortical areas V1 and V2. *PLOS Biology*, *16*(5), e2004132. https://doi.org/10.1371/journal.pbio.2004132

Mann, Z. F., Thiede, B. R., Chang, W., Shin, J.-B., May-Simera, H. L., Lovett, M., … Kelley, M. W. (2014). A gradient of Bmp7 specifies the tonotopic axis in the developing inner ear. *Nature Communications*, *5*(1), 3839. https://doi.org/10.1038/ncomms4839

Mesgarani, N., David, S. V., Fritz, J. B., & Shamma, S. A. (2009). Influence of Context and Behavior on Stimulus Reconstruction From Neural Activity in Primary Auditory Cortex. *Journal of Neurophysiology*, *102*(6), 3329–3339. https://doi.org/10.1152/jn.91128.2008

Schwartz, O., Chichilnisky, E. J., & Simoncelli, E. P. (2018). Characterizing neural gain control using spike-triggered covariance. *Advances in Neural Information Processing Systems 14*, pp. 269–27

Schwartz, O., Pillow, J. W., Rust, N. C., & Simoncelli, E. P. (2006). Spike-triggered neural characterization. *Journal of Vision*, *6*(4), 13. https://doi.org/10.1167/6.4.13

Sharpee, T., Rust, N. C., & Bialek, W. (2004). Analyzing Neural Responses to Natural Signals: Maximally Informative Dimensions. *Neural Computation*, *16*(2), 223–250. https://doi.org/10.1162/089976604322742010

Sherrington, C. S. (1906). Observations on the scratch-reflex in the spinal dog. *The Journal of Physiology*, *34*(1–2), 1–50. Retrieved from http://www.ncbi.nlm.nih.gov/pubmed/16992835

Sripati, A. P., Yoshioka, T., Denchev, P., Hsiao, S. S., & Johnson, K. O. (2006). Spatiotemporal Receptive Fields of Peripheral Afferents and Cortical Area 3b and 1 Neurons in the Primate Somatosensory System. *The Journal of Neuroscience : The Official Journal of the Society for Neuroscience*, *26*(7), 2101. https://doi.org/10.1523/JNEUROSCI.3720-05.2006

Stein, R. B., Gossen, E. R., & Jones, K. E. (2005). Neuronal variability: noise or part of the signal? *Nature Reviews Neuroscience*, *6*(5), 389–397. https://doi.org/10.1038/nrn1668

Taylor, D. M., Tillery, S. I. H., & Schwartz, A. B. (2002). Direct Cortical Control of 3D Neuroprosthetic Devices. *Science*, *296*(5574), 1829–1832. https://doi.org/10.1126/science.1070291

Theunissen, F. E., Sen, K., & Doupe, A. J. (2000). Spectral-temporal receptive fields of

nonlinear auditory neurons obtained using natural sounds. *The Journal of Neuroscience : The Official Journal of the Society for Neuroscience*, *20*(6), 2315–2331. Retrieved from http://www.ncbi.nlm.nih.gov/pubmed/10704507

Vomero, M., Castagnola, E., Ciarpella, F., Maggiolini, E., Goshi, N., Zucchini, E., Ricci, D. (2017). Highly Stable Glassy Carbon Interfaces for Long-Term Neural Stimulation and Low-Noise Recording of Brain Activity. *Scientific Reports*, *7*(1), 40332. https://doi.org/10.1038/srep40332

CHAPTER 2

Neural population coding by composite receptive fields in songbird auditory region

2.1 Abstract

In the field of neural coding of sensory information there are questions that still need to be answered. Some of these questions are include: How to encode and map neural responses to their complex natural stimulus such as human speech and bird song? What intermediate tool can be used to achieve such an encoding mechanism to assist us to reconstruct stimulus from neural responses? How sensory information decodes stimuli to neural response? Answers to these questions will aid us to not only understand how neurons respond to a variety of stimuli but also it can be used to predict neural responses. Recently, we showed that neurons in the auditory region of starling songbirds have composite receptive fields (CRF) with many different acoustic features driving increases and decreases in their firing rate (Kozlov & Gentner, 2016). Here in this study we have used CRF as a tool to investigate spatial-temporal map of receptive field of neuron cells in secondary auditory cortical region of starling songbirds, in respect to natural stimuli. Although there are existing models which attempt to create receptive fields and their map across cortical regions, these models suffer from inability to analyze nonlinear information, they have constraints identifying large number of relevant receptive field features, and they have limitation working with natural stimuli. This study overcame these limitations by adopting a quadratic model to create CRFs. By creating spatial-temporal maps generated from a pool of CRFs, we implied novel information such as: (1) Natural sound can be encoded by populations of neurons. (2) This encoding mechanism and subsequently perceiving natural sound stimuli by brain appears to be uniform while there are some emphasis on parts of stimuli. (3) Perception of natural sound by brain is independent of topography and location of cells. (4) Number of cells needed to encode entire stimuli can be quantified. (5) Connectivity map between cells as well as their plasticity in response to diverse stimuli can be observed. (6) Reconstruction of stimuli as well as prediction of brain

response by CRFs are possible.

2.2 **Introduction**

The mechanism the brain utilizes to encode input stimuli such as sound by population of neurons and the way this encoded information is combined to create a response output are important questions in sensory neuroscience. Neural encoding is referred to as mapping stimuli to response and is primerly used to recostruct stimuli from neural responses (Mesgarani, 2009) . The phenomena of stimuli reconstruction is a first and decisive step towards creating a new memory (Baddeley, 2009) . On the other hand, neural decoding is a reverse mapping that maps and recostructs response from stimuli (Koyama ,2012).

Recently, we showed that single neurons in secondary auditory cortical regions of european starlings song birds have composite receptive fields (CRF) (Kozlov & Gentner, 2016). In this study we aim to generate a pool of CRFs from a large population of cells in the higher auditory region of starling bird brains in order to investigate auditory processing, natural song encoding, and neural response decoding mechanisms in birdsong.

Since avian and mamals such as hummans are proccesing auditory data in a very similar way at cells level ((Karten, 2013) & (Harris K. , 2015)), outcomes of this study might be applicable to mamals and human.

There are existing models to create receptive fields of neurons such as spike trigger average (STA) to build STRFs (De Boer & Kuyper, 1968), spike-triggered covariance (STC) (Schwartz O. C., 2002), and maximally informative dimensions (MID) (Sharpee, 2004). These models although have provided a wealth of information about receptive fields, stimuli, and response characteristics, they suffer from a number of drawbacks such as inability to characterize nonlinear information of

stimuli (Thunissen, 2000), limitation working with natural stimuli e.g. human speech or bird song ((Schwartz O. P., 2006)& (Eggermont, 1983b)), and limitation identifying large number of relevant receptive field features with respect to natural stimuli (Kozlov & Gentner, 2016). In contrast the Maximum Noise Entropy model (MNE), utilized in this study, overcomes most of these drawbacks ((Kozlov & Gentner, 2016), (Fitzgerald, 2011a), (Sharpee, 2004) , (Bialek W. D., 2006), and (Fitzgerald J. S., 2011b)). The MNE model looks for mutual information and highest correlation between audio stimuli and the brain response in the form of composite receptive fields at the cellular level.

To map CRFs of a population of cells with respect to stimuli, we have recorded action potentials through nine recording sections across five birds from their higher-level auditory cortex, Caudomedial Nidopallium (NCM), during playback of starling bird songs with high density electrodes. After sorting and extracting neuron cells, MNE has been performed on 154 cells and the ten most significant facilitatory and ten most significant suppressive CRFs have been extracted for each cell. Significant CRFs are generated from spikes with the highest probability of occurrence (facilitatory) and lowest probability of occurrence (suppressive) through the MNE logistic quadratic model. The first ten significant CRFs for both facilitatory and suppressive features contained the least amount of noise on average across 154 cells.

After generating a large pool of CRFs (20*154=3080) for a population of 154 cells, now we are able to map these neural cells and their significant facilitatory and suppressive CRF features along implanted electrodes (Spatial map) and also with respect to the audio stimuli time (Temporal map). The spatial map is based on the location of each cell corresponding to an electrode channel. Each cell location along the depth electrode is calculated based on the reverse amplitude of its action potential (Rossant, et al., 2016). On the other hand, temporal information of each cell and

its CRFs, with respect to bird song stimuli, can be characterized by cross-correlation of CRFs with spectrogram of bird songs.

It appears that we can capture several useful data points from this map:
For the first time this map can be utilized to encode natural sound by populations of neurons. Furthermore, the process of encoding and perceiving natural sound stimuli by the brain appears to be uniform (temporal mapping) while there are some emphasis and weights on parts of stimuli (spatial mapping). Also, through the spatial map we have concluded that stimuli perception by the brain is independent of topography and location of cells (similarity of CRFs in-between cells versus cells relative distances). Moreover, from the projection of location of CRFs to the temporal map we have discovered the percentage of encoded stimuli by certain cell numbers and consequently were able to predict number of cells needed to encode entire stimuli.

Additionally through this map we witness a connectivity map between cells in response to stimuli by monitoring when cells have common CRFs and when they have unique CRFs. Also, some parts of stimuli does not trigger any cells and CRFs. These facts may accentuate to phenomena where a network of neurons, actively process part of stimuli and disregard the rest of it to avoid over use of memory ((Anderson, 2004) & (Johnson, 2004)). Furthermore, this connectivity map across cells, changing by changes in stimuli which this is an indication of cell response flexibility and short-term plasticity ((James, 1890) & (Pascual, 2005)). All these phenomena are observed for both facilitatory and suppressive responses.

An advantage of composite receptive fields generated from the MNE quadratic model versus receptive fields generated by linear models is that CRFs captures many of the variations of natural stimuli therefore their spectrograms look similar especially if cells are stimulus-locked with low noise. Employing this fact we have reconstructed bird song stimuli from the pool of existing

CRFs. Furthermore, we have pushed the limit to reconstruct novel stimuli by this CRF pool. Here we attempted to reconstruct forty nine novel songs and even with a relativity small pool of CRFs the result showed we are able to reconstruct up to 4.3% of each of the 49 novel bird songs.

Finally we were able to predict the spike train response of neurons in response to forty nine novel songs by employing MNE model. The result showed a median response prediction of 60% across multiple cells.

Overall, these outcomes demonstrate that composite receptive field can be used as a tool for brain mapping, encoding stimuli, and decoding populations of neural activity to aid us in understanding brain neural coding mechanisms. Composite receptive fields generated from neural responses also can have practical applications such as reconstructing human speech to design better hearing aid devices (Schäfer, 2018) as well as speech decoders to help speechless patients communicate to the outside world ((Rieke F. B., 1995), (Stanley, 1999), and (Zion Golumbic, 2013)).

2.3 **Methods**

2.3.1 ***Animal preparation and Surgery***

In this study, nine neuronal recordings are performed on five European starling adult male birds under a protocol approved by the Institutional Animal Care and Use Committee of the University of California, San Diego. The birds weighed 90 g±10% fasting an hour before applying anesthesia. Urethane 7 mL/kg was administered in three separate doses. Urethane is used to achieve long stimulus presentation in this study (Masamoto & Kanno, 2012). Following that a short dose of isoflurane was administered to transition the subjects into an anesthetized state. Subjects were then placed in a stereotaxic bed, the oxygen flow was set to 11.5L/min and isoflurane

set to 1%. The subjects head was secured between ear bars and their beaks set at a 45 degree angle. The feathers were removed on the head, scalp was cut away, and the upper skull removed. A fixation pin was secured in a holder and lowered into place while dental cement was applied to the base to secure it. After completion of the recordings, postoperative butorphanol 25 mg/kg was administered.

2.3.2 *Electrophysiology*

After placing the subjects into the recording chamber, a region of skull over the NCM (Caudomedial Nidopallium) auditory region was removed. A small opening was made in the Dura and a ground wire inserted below the surface, after which the exposed brain is covered by a silicone barrier. Following, a 32 channel electrode site (NeuroNexus A1x32-Edge-10mm-20-177), made of iridium with 20µm spacing and 177 μm^2 surface area was employed for neural recording. The electrode was mounted in a stereotaxic probe holder and moved to a coordinate of AP=20-2500 µm caudal and ML=500-1700 µm lateral right of Y-sinuous with depth Z=1100-3200 µm across five subjects.

The following table describes how individual recordings were performed. The second column of Table 2-1 displays individual penetration locations for five subjects.

Table 2-1: Subjects database used in this study.
First column: Number of birds. Second column: Number of electrode penetrations (Pen) per subject and their recording locations. Third column: Number of single cells (S) and multi-units (M) used in this study from population of recorded cells for each recording. Fourth column: Songs which were played 20 times for each subject.

Subjects	Recording location	(Used cells)/(Recorded cells)	Stimuli
1	Pen 1_Lft_AP2000_ML700_Z1900 Pen 2_Lft_AP2000_ML700_Z2200	(30:4S-26M)/(50S-100M) (20:3S-17M)/(45S-50M)	Song 1 Song 2 Song 3
2	Pen 1_Lft_AP20_ML1700_Z2500 Pen 2_Lft_AP20_ML1680_Z2581	(10:3S+7S)/(27S-32M) (30:9S-21M)/(36S-40M)	Song 1 Song 2 Song 3
3	Pen 1_Lft_AP2500_ML500_Z3200	(8:5S-3M) /(9S-11M)	Song 1 Song 2 Song 3
4	Pen 1_Lft_AP750_ML1750_Z1100 Pen 2_Lft_AP750_ML1750_Z1500 Pen 3_Lft_AP750_ML1750_Z2000	(10:6S-4M)/(13S-34M) (30:2S-28M)/(15S-50M) (10:3S-7M)/(12S-32M)	Song 1 Song 2 Song 3 Song 4 Song 5
5	Pen 1_Lft_AP500_ML500_Z1700	(6:4S-2M)/(7S-17M)	Song 1 Song 2 Song 3 Song 4 Song 5

2.3.3 *Auditory stimulation*

The stimuli are recorded from adult starling male songs at 44.1 thousand samples/s and played back at a 60-dB mean level. Three or five songs were played for each subject (Table 2-1 column 4). The songs were approximately one minute long and played 20 times during each recording sessions. 49 other songs were also played one time randomly for subjects for further analysis as well as preventing stimulus selectivity by subjects (Yaneri & Manuel, 2013).

2.3.4 *Data acquisition*

While stimulus is presented to the subjects in a sound attenuation box, neural action potentials are recorded with the 32 channel electrode and amplified by an A-M amplifier system (model 3600). The recordings were performed with a 20 KHz sample rate with a low-pass filter of 20Hz and high-pass filter of 20 KHz. The recordings then are converted to Matlab files with Spike2 software (CED) after which spike sorting is completed by Klustakwik software. The Klustakwik program can deal with high-dimensional data and works by fitting a mixture of Gaussian curves along with an Expectation–Maximization algorithm with unconstrained covariance matrices. Furthermore, for spike detection this program uses a flood-fill algorithm between two thresholds and clusters similar spikes as one neuron (Rossant, et al., 2016).

Table 2-1 displays the overall recording information of five subjects. Columns of table show: 1) Number of electrode penetrations per subject. 2) Electrodes recording locations. 3) Number of single cells (S) and multi-units (M) employed from population of recorded cells from each recording sessions. 4) Number of songs which were played 20 times for each subject.

2.3.5 *Data Preparation*

During each recording sessions 24 to150 single cells and multi-units are extracted which are differentiated mostly based on their refractory period 1-2ms (Dayan & Abbott, 2000). The cells that are employed for this study are primarily stimulus locked and contain low noise. Different cell population sizes are chosen from a pool of recorded cells per penetration (Table 2-1, column 3) to give us the ability to further investigate the effect of cell population sizes on various analysis that we perform in this study.

Figure 2-1B-C display examples of a single and multi-unit cells used in this study. To

compute CRFs via the MNE model we need to construct two inputs per cell: response (trials average) and stimuli (power spectral density (PSD) of a spectrogram of bird songs).

To create the input stimuli, we concatenated the bird song waveforms that were played for the subjects, down-sampled to 24 KHz, and then by use of spectrogram function in Matlab it is converted into a spectrogram. The spectrogram parameters are nfft=128, Hanning window of 128 with 50% overlap (Figure 2-1B and Figure 2-1C first rows). Through this process the DC part of signal is removed. Following, the adjacent 64 frequencies are averaged pairwise twice from 32 to 16 frequency bands with band ranges of 750-12KHz (Nyquist frequency). Similar to frequency, the adjacent spectrogram time bins are averaged three times to a size of approximately 20 bins, which is a common bin size to calculate receptive fields. Finally, power spectral density of this down-sampled spectrogram is extracted and saved as MNE stimuli input. The bird song stimuli has been repeated 20 times and the cells response has been recorded as spike trains. Figure 2-1B-C second row demonstrates raster plots of spike train responses of 20 trials for single and multi-unit cells. To compute the average of the spike train responses we first divide the repeated 20 trials to 4 groups of five trials then we calculate the trial average of each 5 trials and concatenate those (Figure 2-1B-C third row). Finally, the concatenated trial averages are down-sampled three times. A magnified 5 second window of both Figure B and C are shown underneath the respective figures. Additionally, the action potential waveforms of a single and multi-unit cells are shown in Figure 2-1D-E. Now, both stimuli and trial average responses are ready to be processed by the MNE model.

2.3.6 *Composite receptive field analysis based on Maximum Noise Entropy Model (MNE)*

Maximum noise entropy model attempts to extract receptive fields of each cells based on

mutual information and highest correlation between response and its stimuli. It is based on probability of spikes/response given stimuli and described as the following logistic function:

Equation 1

$$\mathrm{P(Response|Stimuli)} = \frac{1}{1+e^{(a+h.s+s^{T}Js)}}$$

By minimizing the quadratic polynomial equation $f(s) = (a + h.s + s^T Js)$, we obtain a, h, and J parameters. Where a, h, and J are correspond to a constant number, linear part, and quadratic part of receptive field features. To extract these parameters we pick 1/4 of the trial averages as a test set and 3/4 of the trial averages as training set. This process is repeated for stimuli as well. Next, theses sets are used to estimate a, h, and J parameters. For regularization early stopping has been utilized to prevent overfitting. Following, the parameter estimation repeats four times. Each estimation uses one of the trial averages against the other three trial averages (Figure 2-2A). The reasons trial averages are resampled through the trails and parameters are estimated four times are to reduce the bias and to increase the possibility of locating and removing noisy trials.

Figure 2-2B demonstrates a technique to remove noisy trials from noisy cells. Through four times resampling, every time a set of J-matrix and consequently sets of CRFs are created per cell. If we repeat this process for the population of cells, e.g. 30 cells in Figure 2-2B, by use of the t-SNE technique (Van der Maaten & Hinton, 2008) similar CRFs cluster together for each cell. Subsequently similar CRFs in clusters can be extracted by the HDBSCAN method (Ester, 1996) while noisy CRFs produced by noisy spike trains, are separated from clusters and show up as outliers.

To extract composite receptive fields we focus on the weight matrix J of the quadratic model. Diagonalizing matrix J yields to two main factors, eigenvalues (D) and eigenvectors (V).

Each eigenvector (V) corresponds to a receptive field whereas the eigenvalues point to the significance of receptive fields. To control statistical significance, 500 symmetrical random Gaussian matrices with size and moments equal to Js are created and then the distribution of their eigenvalues are calculated. This distribution is used to verify eigenvalues that are significant. Significant eigenvalues are the ones that have the highest or lowest probability of occurring on the logistic function. In addition, negative eigenvalues and their related eigenvectors correspond to facilitatory CRFs of neurons. Vice versa, positive eigenvalues and their related eigenvectors correspond to suppressive CRFs. Figure 2-1F from right to left show an example of CRFs extracted from a single cell with ten most significant negative (facilitatory) and ten most significant positive (suppressive) features. Each CRF contains power modulation in the frequency band from 0-16 (750-12KHz) across 20 time bins (400s).

The reasons ten most positive and ten most negative significant eigenvectors are extracted from each cells are: first, these twenty eigenvectors contain lower noise than the rest of eigenvectors on average across 154. Second this low quantity of features, 20, can provide a better prediction model, by ignoring the noisy features, in comparison with employing all the features of full rank MNE (320 features) (see section 2.4.7) (Kaardal, 2017). More details about the MNE model are explained in ((Kozlov & Gentner, 2016) and (Fitzgerald , 2011b)).

Figure 2-1: Extracting CRFs from recorded cells.
(A) Action potentials recording paradigm: A high density recording electrode is implanted in the NCM auditory area of a starling bird brain. While bird songs play for the subject, spikes are recorded from single and multi-unit cells. The red circle demonstrates location of the implanted electrode. Spike waveforms of cells recorded from subject 4-Pen1 are shown in the rectangular box. (B) Example of a single cell. Top row: A bird song spectrogram. The color bar on right indicates power density. Second row: Raster plot of spiking activities of 20 trials. Third row: Trial average/spike train of the 20 trials. Underneath magnification of five second of spectrogram, raster, and trial average has been shown. C) Example of a multi-unit activity: Figure descriptions are same as (B). (D) Action potential waveform of the single cell. The black bar indicates the amplitude of waveform. (E) Action potential waveform of multi-unit activity. (F) Example of estimated CRFs of the single cell using MNE model: Right: 10 suppressive CRFs extracted from the 10 most significant positive eigenvalues and their corresponding eigenvectors of J-matrix. Left: 10 facilitatory CRFs extracted from the 10 most significant negative eigenvalues and their corresponding eigenvectors of J-matrix. Each CRF contains power modulation in frequency band from 0-16 (750-12KHz) across 20 time bins (400s). The color bar on the right displays the power density of CRFs.

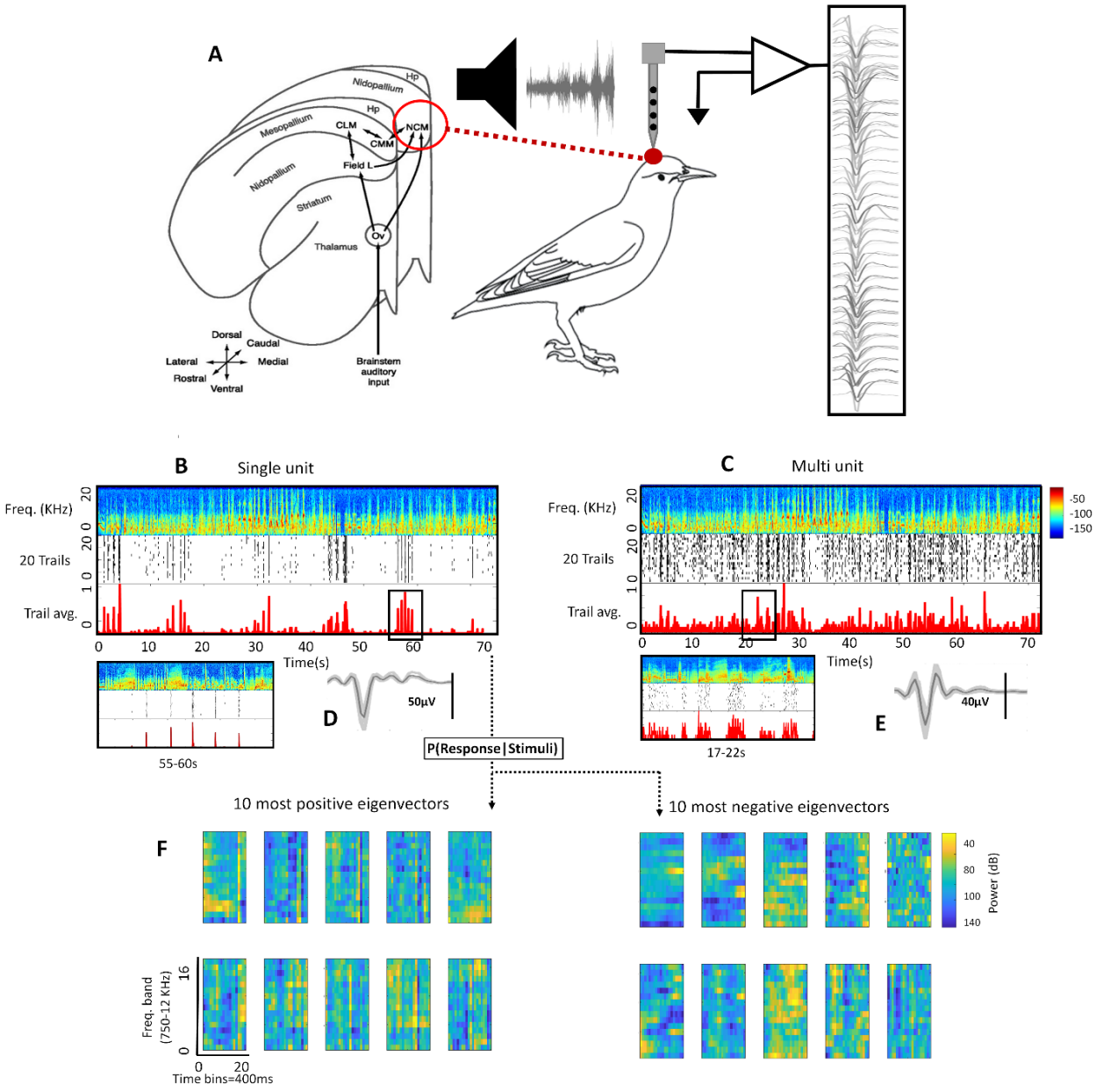
A
Hp
Nidopallium
Hp
Mesopallium
CLM
NCM
CMM
Field L
Nidopallium
Striatum
Thalamus
Ov
Dorsal
Caudal
Lateral
Medial
Rostral
Ventral
Brainstem auditory input
B
Single unit
Freq. (KHz)
20 Trails
Trail avg.
Time(s)
55-60s
50µV
D
C
Multi unit
Freq. (KHz)
20 Trails
Trail avg.
Time(s)
17-22s
40µV
E
-50
-100
-150
P(Response|Stimuli)
10 most positive eigenvectors
10 most negative eigenvectors
F
Freq. band (750-12 KHz)
Time bins=400ms
Power (dB)

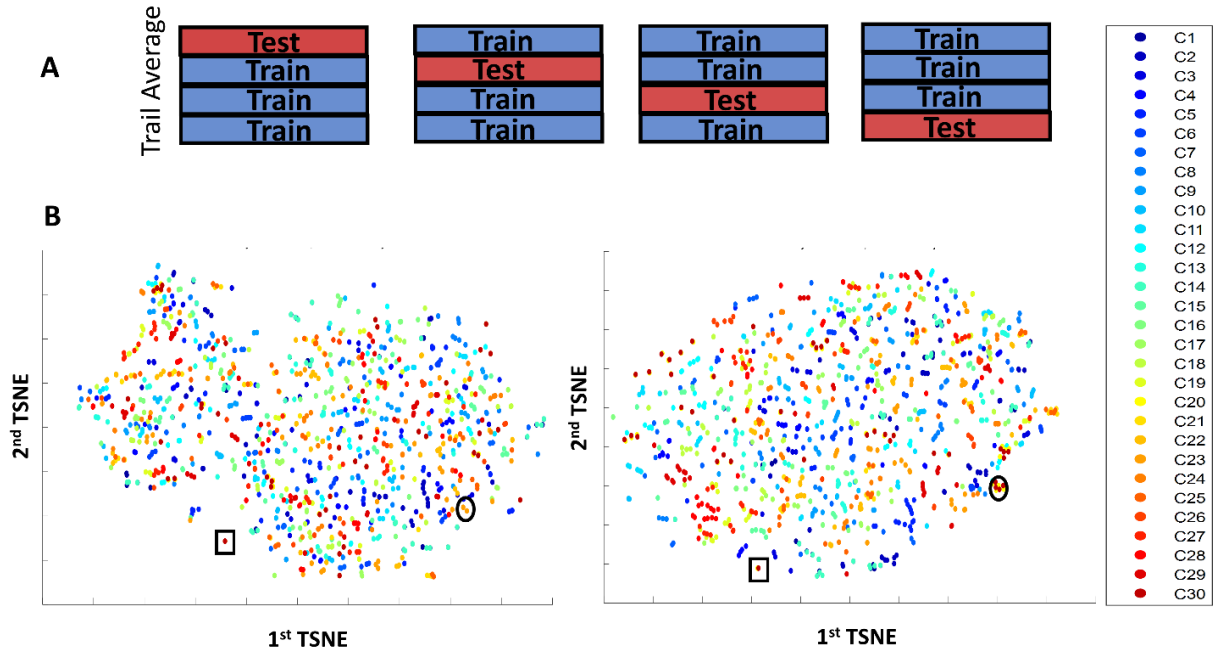

Figure 2-2: Identifying cells noisy trials by t-SNE.
(A) Demonstration of resampling method through the trial averages. (B) Right: Clustering similar CRFs by t-SNE for 30 cells (subject 2, Pen2) with 10 facilitatory features across four resampled data sets. As an example a set of four related CRFs are shown by a black circle. The noisy CRFs are separated as outliers which mostly show up as one dot. An example of one of these outliers has been framed in the black square. Left: similar clustering for suppressive CRFs. The color bars demonstrate 30 cells arranged based on their depth along dorsoventral plane in NCM.

2.4 Result

2.4.1 *Spatial and temporal mapping of pick activation of CRFs in respect to stimuli*

To investigate the spatial-temporal map of CRFs we first need to extract the CRFs from a population of cells. In this study we have chosen 154 cells from nine penetrations across five subjects (Table 2-1).Then we have extracted the ten most negative (facilitatory) and ten most positive (suppressive) CRF features of each cell and created a pool of 3080 CRFS ((10f+10s)*154 cells=3080). To achieve the spatial mapping, first cells are organized based on their locations along the dorsal-ventral (Z) axis in the NCM auditory area. The spatial (depth location) information of cells are calculated via the Klustakwik program (Rossant, et al., 2016). The cell locations are

calculated based on their inverse action potential amplitude of each cell in reference to the z-axis (depth) of the electrode shank. To compute the cells' CRFs temporal map, normalized cross-correlation method is used. This model cross-correlates the power spectrogram of each CRFs with the power spectrogram of stimuli through a sliding window to locate maximum cross-correlation of each CRFs with the stimuli. Ultimately, maximum correlations (pick activations) are tested to be more than 60%. With this method we were able to find the location of CRFs corresponding to specific portions of vocal elements of stimuli.

Figure 2-3 demonstrates a spatial-temporal map of pick activation of a pool of 3080 CRFs with stimuli. Figure 2-3A displays the location of implanted electrodes along the dorsoventral plane in the NCM for nine penetrations across five subjects. Next to each penetration the recorded cells are shown which are organized spatially by their depth locations. The cells are either single cells in green or multi-units in black (Figure 2-3B). Figure 2-3C displays a spectrogram of three concatenated bird songs and underneath, Figure 2-3D, shows a temporal map of the 154 cells with 3080 CRFs in respect to the stimuli. The facilitatory CRFs are shown in red dots (3080/2=1540) and the other 1540 suppressive CRFs are shown in blue dots. Each dot corresponds to the maximum correlation (pick activation) of each CRF with a spectrogram of songs. The Temporal map can be a method to decode stimuli by CRFs. Figure 2-3E demonstrates projections of facilitatory (in red dots), suppressive (in blue dots), and their joint (red and blue dots) CRF locations in respect to stimuli as flat distributions along the x-axis. This demonstrates that even a small sample, e.g. 50 cells (from subject 1), can provide a temporally dense representation of natural song.

To investigate temporal distribution of CRFs with more details, we have created a histogram of temporal distribution of CRFs of cells for each subject (Figure 2-3F). Red bars

correspond to facilitatory CRFs and blue bars correspond to suppressive CRFs with bin sizes of 20. Sections 2.4.2 to 2.4.7 discuss the properties of this spatial-temporal map in more details. Some of these properties include the possibility of utilizing CRFs' histogram and their flat distribution as a tool to compute the quantity of CRFs and cells needed to encode entire stimuli. Also, the amplitude/weight of each bar in the histogram (spatial information) demonstrates the number of repeated (similar) or unique CRF features across all the cells. This information can aid us to find a connectivity map between cells. Additionally, from CRFs temporal information and their corresponding locations to the stimuli we are able to find where in the stimuli CRFs are originated from. This map not only can be used as a stimuli encoding tool by CRFs but also, lead us to examine the possibility of reconstructing stimuli via CRFs and furthermore predict brain responses.

Figure 2-3: Spatial-Temporal map of peak activation of CRF features in respect to stimuli. (A) Location of implanted electrode in NCM for nine penetrations across 5 subjects. (B) Spatial location of 154 single cells (green dots) and multi-units (black dots) used in this map. Population of cells in subject1 is 50, in subject 2 is 40, in subject 3 is 8, in subjects 4 is 50, and subject 5 is 6 (C) Spectrogram of three concatenated bird songs. (D) Temporal location of CRFs in respect to bird song stimuli. There are 1540 facilitatory (red dots) and 1540 suppressive (blue dots) CRFs across 154 cells in this map. Each dot corresponding to the maximum correlation (pick activation with r>60%) of each CRF with song spectrograms. (E) Flat projections of all the facilitatory CRFs (red line), suppressive CRFs (blue line), and their joint (red and blue) CRFs location onto the x-axis. (F) Histogram of CRFs across cells for each subject (bin size=20). Red bars correspond to facilitatory CRFs and blue bars correspond to suppressive CRFs.

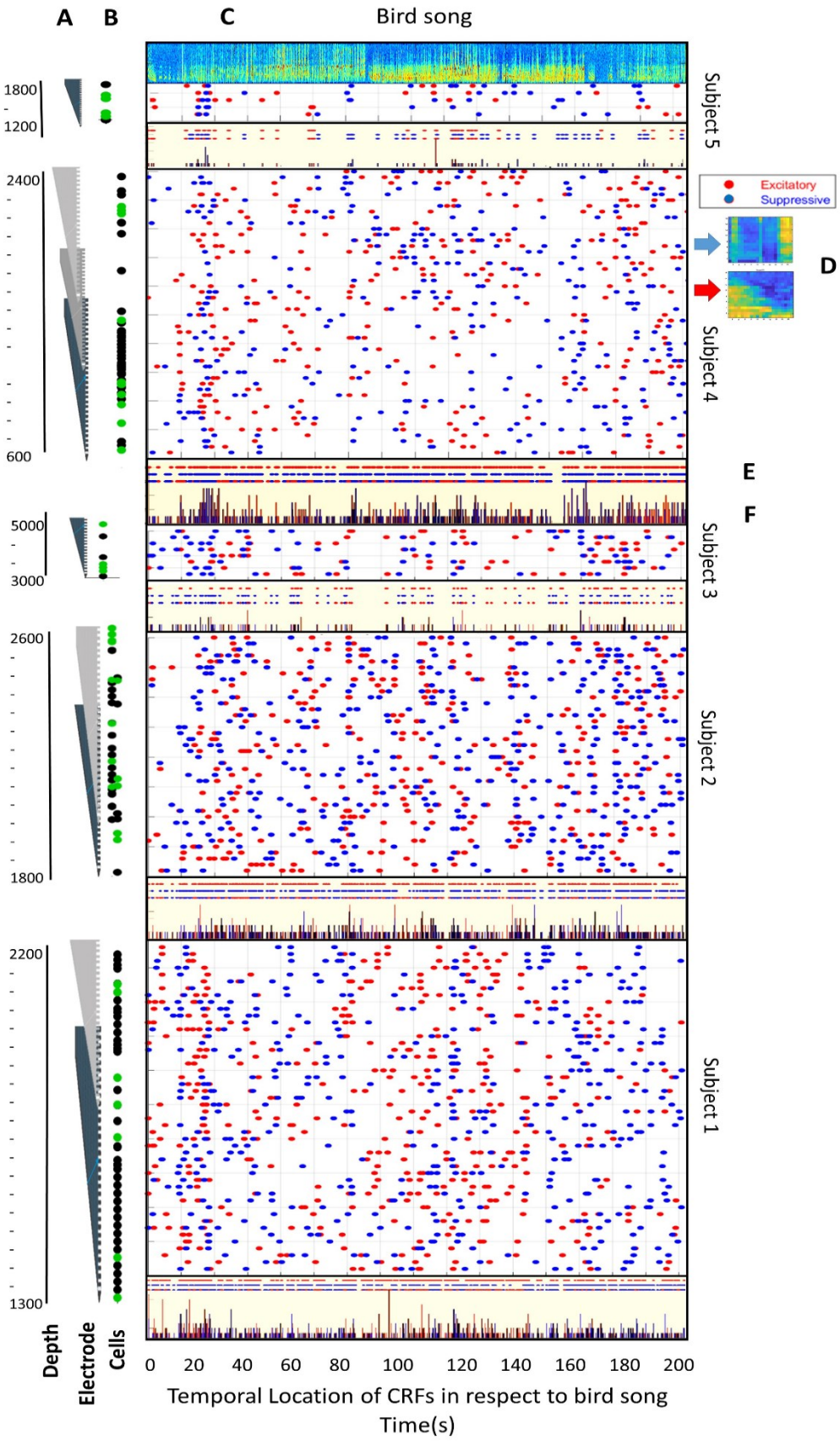
A
B
C
Bird song
1800
1200
2400
600
5000
3000
2600
1800
2200
1300
Subject 5
Subject 4
Subject 3
Subject 2
Subject 1
Excitatory
Suppressive
D
E
F
Depth
Electrode
Cells
0
20
40
60
80
100
120
140
160
180
200
Temporal Location of CRFs in respect to bird song
Time(s)

2.4.2 *Spatial and Temporal distribution of CRFs*

In Figure 2-4 we collapse CRFs histograms of all 154 cells across all the subjects from Figure 2-3 into two histograms. The histogram with red bars belongs to facilitatory CRFs. Projection of bars on to X temporal axis results 497 points. These points are belong to 497 CRFs that are shared across cells from default pool of 1540 facilitatory CRFs. Similarly, the second histogram with blue bars corresponds to suppressive CRFs with 509 shared CRFs from default pool of 1540 suppressive CRFs. In third row we can observe comparison of these two facilitatory and suppressive distributions in one plot. If we combine amplitude of these two plots we will receive the black distribution graph on forth row with 649 shared CRFs from default pool of 3080 facilitatory and suppressive CRFs.

Overall, in all these plots, the x-axis demonstrate temporal distribution of CRFs of 154 cells in respect to the stimuli. Each bin belongs to a location of one CRF and its bar amplitude on the y-axis indicates the number of cells that are sharing a particular CRF. Observing these plots, although CRFs distributions are temporally uniform (based on one-sample Kolmogorov-Smirnov with rejection significance level of 5%), the amplitude (weight) of number of cells with common CRFs ,triggred by specifc part of stimuli, varies. These facts are true for both facilitatory, suppressive, and their combinatins distributions.

From these observations one might conclude that while the brain perceives sensory stimuli in a temporally uniform way, there are emphasis (weights) on the explicit parts of stimuli.

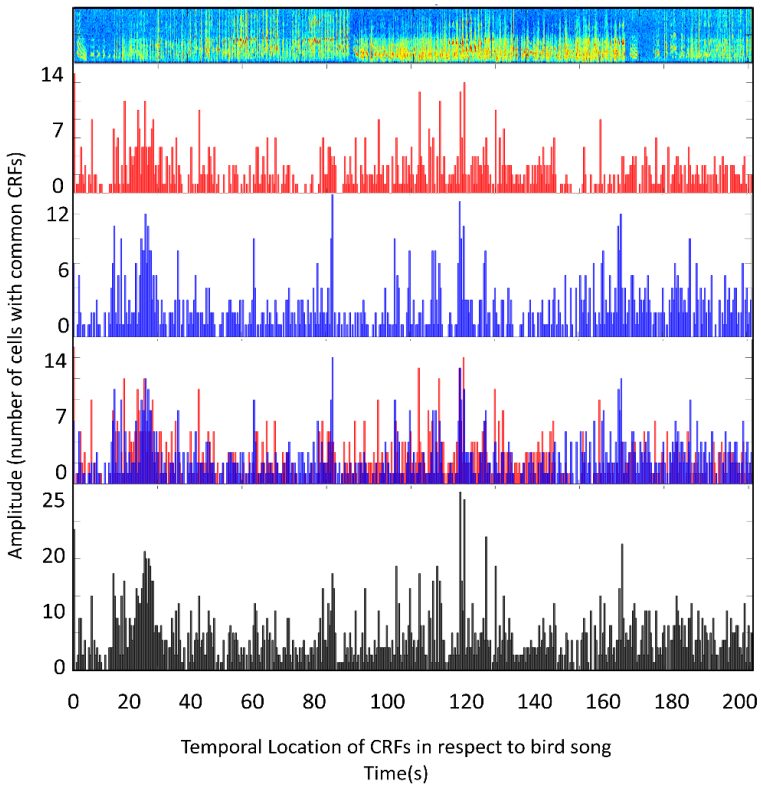

Figure 2-4: Spatial and Temporal distributions of CRF features in respect to stimuli. Top: Spectrogram of stimuli. Second row: Temporal distribution of facilitatory CRFs for 154 cells across five subjects in respect to 200s stimuli is shown on the x-axis. The y-axis displays amplitude and weight of cells containing common CRFs. Third row: Temporal and amplitude distributions of suppressive CRFs. Fourth row: Comparison of combination of temporal and amplitude distributions of facilitatory and suppressive CRFs.

2.4.3 *In-between cells' CRF similarity versus cell distances*

From histogram of the spatial-temporal map in Figure 2-3F we can detect some CRFs similarity between cells of each penetration across five subjects. This fact inspired us to further investigate if the CRF similarity between cells are dependent on the relative distance between cells along the dorsoventral plane. To statistically determine the answer to this question, autocorrelation method has been used on the CRFs of cells of each subject. Figure 2-5A shows an example of a matrix of autocorrelation on 30 cells from subject2-pen2. Each cell contain 10 facilitatory CRFs. Following, the correlation coefficients (corrcoef) are extracted from the matrix except the diagonal

cells to only evaluate in-between cells' CRFs' similarity. This process has been repeated to extract in-between cells CRFs' similarity information for both facilitatory and suppressive response of all the subjects. Following, relative distances between cells for each subject is calculated. The colored circles in the transparent background in Figure 2-5B demonstrate the similarity (corrcoef) of CRFs between cells for five subjects versus their cells relative distances. Subject 1 in green contains 50 cells, subject 2 in blue contains 40 cells, subject 3 in black has 6 cells, subject 4 in red has 50 cells, and subject 5 contains 8 cells. The fitted regression lines of each subject are shown on top. The legend bar on the right side shows the five subjects color code as well as facilitatory regression lines (n) as circled lines and suppressive regression lines (p) as squared lines. The distance between circles in facilitatory regression lines as well as squares in suppressive regression lines indicate CRFs similarity density which is high around zero and decreases toward 1. Most of the regression line slopes are constant around a point in the y-axis (distance), this is true for both facilitatory and suppressive. There is a slight slope angle for subject 3 (black regression lines) which could be due to the fact that subject 4 cells contain more noise than other subjects' cells. Overall, what we observe from these regression lines are that CRFs' similarity in-between cells is independent of relative cell distances along the dorsoventral plane for both facilitatory and suppressive responses across all subjects. In other words, stimuli encoding of population of neurons is independent of the neurons locations and topology.

Secondly, end of the regression lines in positive side of the graph present the most similar CRFs between cells in different subjects. Figure 2-5C shows an example of six cells with 10 similar CRFs between each two (C1&C13, C20 & C30, and C21 & C13) for subject 2 as well as 10 similar CRFs between (C15-C17) for subject 1.

Since these cells are mostly multi-units and not neighbors, this high similarity between

their CRF populations for every two units indicates that these units are synchronized in response to stimuli. Moreover, this high similarity between units are observed in cell populations equal or more than 30. To understand and draw a more accurate conclusion about this observation, similarity between cells' CRFs of larger cell populations is suggested.

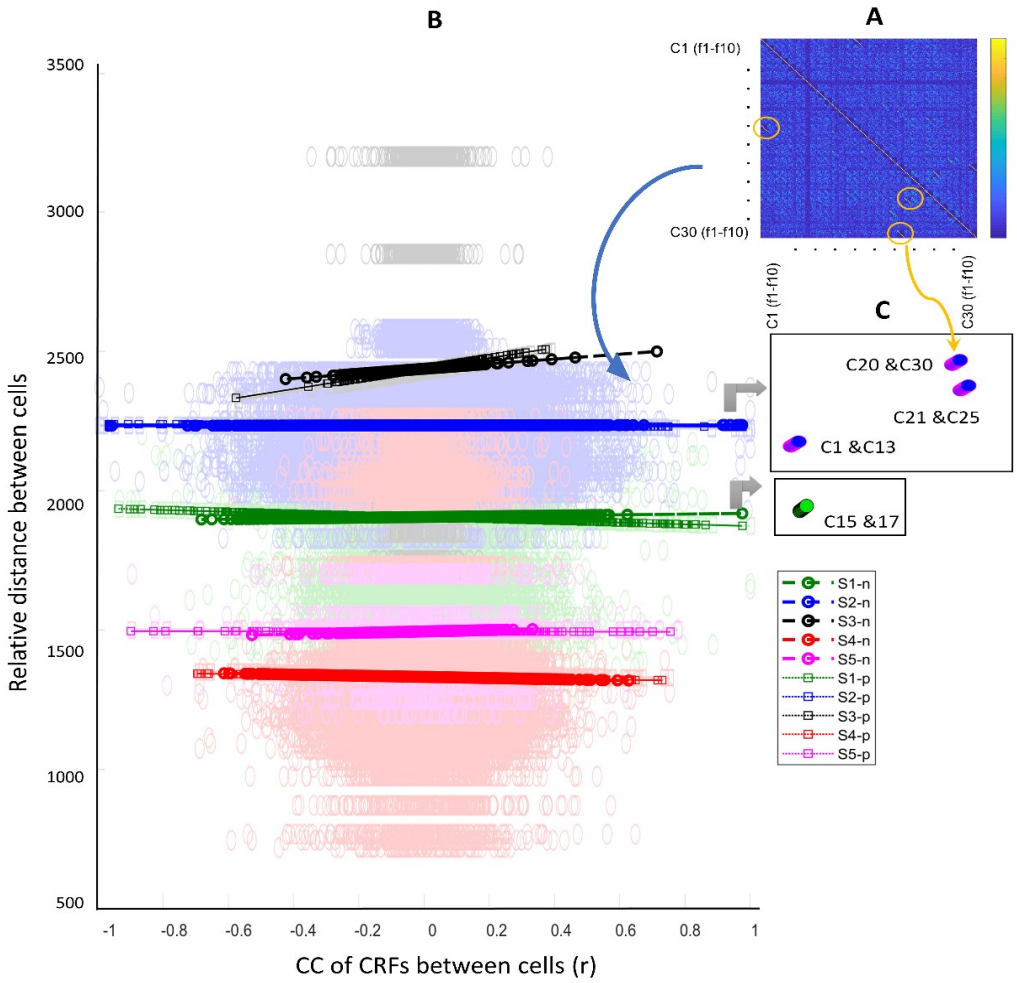

Figure 2-5: CRFs similarity in-between cells (r) versus relative cell distances.
(A) Example of autocorrelation matrix for CRFs of 30 of cells from subject 2. Each cell contains 10 facilitatory CRFs. The correlation coefficients are extracted from the matrix except the diagonal cells to only evaluate in-between cells similarity information. (B) The same process has been performed on facilitatory and suppressive responses of the five subjects. The result of similarity between cells' CRFs for each subject versus their relative cell distances is represented by colored circles with a transparent background. The fitted regression lines of each subjects' data is shown in a darker color on top. (B) The legend bar on the right side shows the five subjects' respective color codes. The facilitatory regression lines (n) is shown with circled lines and suppressive regression lines (p) are displayed as squared lines. The distance between circles in facilitatory regression lines as well as squares in suppressive regression lines indicate CRFs similarity density along the x-axis. (C) 100% CRFs' similarity between sets of two cells have been observed at the positive end of regression lines as well as different cell populations' autocorrelation. For example (C1 & C13), (C20 & C30), and (C21 & C13) from Matrix in (A) encompass 100% similarity between their CRFs.

2.4.4 *How many cells and CRFs can encode entire stimuli?*

To investigate the number of cells and CRFs needed to encode the stimuli for each recording, we have calculated the number of facilitatory and suppressive CRFs that are encoding sections of stimuli by counting their flat, temporal location points (flat means: projection of histogram bars as points to one dimensional x-axis) (Figure 2-3E). Since each CRF has 20 bins, by multiplying the CRFs number by their respective 20 bins and dividing the results by the stimuli length, we can find the percentage of stimuli encoding by the CRFs and consequently find the number of cell needed to encode the entire stimuli. In Table 2-2 we have calculated stimuli encoding percentage for nine recordings. An example for such a calculation is, if we consider subject1-penetration1 (S1-P1) with 30 cells, from the pool of 600 CRFs of this recording (30 cells*(10 faciliatory+10supprasive)), 348 CRFs are temporally encoding the songs and since each CRF point has 20 time bins therefore all 348 CRFs together cover 6960 time bins (348*20 bins). If we compare this number with the length of stimuli for this study, 16100 time bins (equal to 207 second), we can find the percentage of stimuli decoding by these 348 CRFs extracted from 30 cells which will be 43.2%.

Figure 2-6 demonstrates a relationship between the cell numbers of nine recordings with their stimuli encoding percentages. Cell quantities exhibit an approximate linear relationship to the stimuli encoding percentages. The red line fit is based on power law. The green dot, corresponding to the x-y green lines, is a prediction of amount of cells needed to cover and encode the entire stimuli by the CRFs. Here 100% of the stimuli (207s) predicated to be encoded by 90 cells.

It is worth pointing out that having different sizes of cell populations assist us to create this prediction paradigm. In addition, choosing same size cell populations from different recordings resulted in a similar stimuli encoding percentage range (e.g. a cell population size of 10 for three

recordings of S2-P1, S4-P1, and S4-P3 all lead to similar average encoding of 20%. Similarly, in a cell population size of 30, all three recordings of S1-P1, S2-P1, and S4-P2 correspond to average encoding of 45%. This fact emphasizes the accuracy of this stimuli encoding mechanism by CRFs. Based on this method we should be able to investigate stimuli encoding percentage of just facilitatory CRFs or suppressive CRFs alone if needed (Table 2-2).

Table 2-2: Number of cells and CRFs vs encoding stimuli percentages.
First column: Nine penetrations across five subjects. Second column: Number of cells for each penetration. Third column: Number of facilitatory CRFs (f) and suppressive CRFs (s) calculated from temporal flat distribution of Figure 2-3E (top red and middle blue plots) versus default CRFs (Number of cells *10 CRFs). Forth column: Number of concurrent facilitatory and suppressive CRFs adopted from Figure 2-3E. Fifth column: Encoding stimuli percentages for different cell population sizes.

Subject-Penetration	Cells	Encoding CRFs/Default CRFs	Encoding concurrent F&S CRFs	Stimuli encoding %
S1-P1	30	F=190/300 S=218/300	348/600	43.2
S1-P2	20	F=141/200 S=150/200	255/400	31.7
S2-P1	10	F=90/100 S=90/100	167/200	20.7
S2-P2	30	F=226/300 S=234/300	356/300	44.2
S3-P1	8	F=69/80 S=73/80	135/160	16.7
S4-P1	10	F=86/100 S=94/100	168/200	20.8
S4-P2	30	F=217/300 S=219/300	371/600	46.1
S4-P3	10	F=93/100 S=90/100	172/200	21.4
S5-P1	6	F=49/60 S=50/60	93/120	11.5

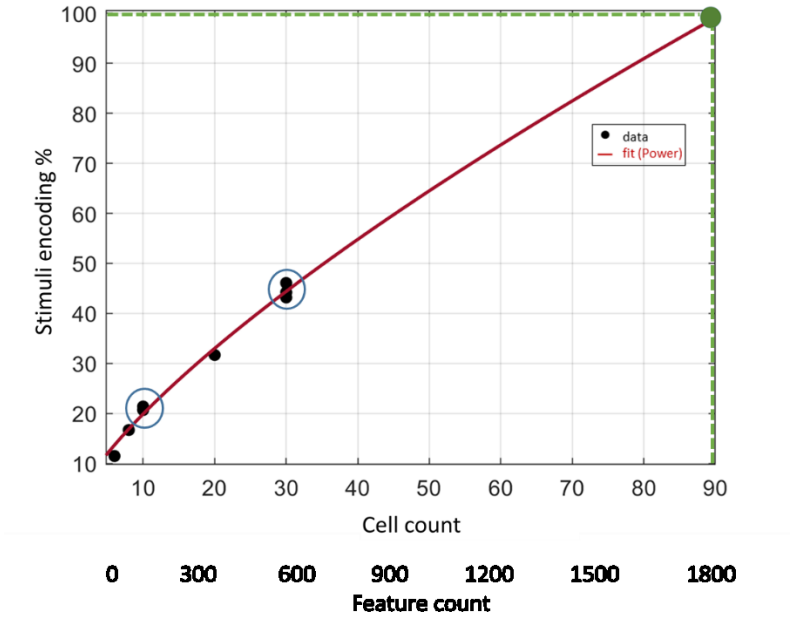

Figure 2-6: Prediction of amount of cells needed for encoding entire stimuli.
Demonstration of relationship between cell numbers of nine recordings versus their stimuli encoding percentage (black dots) adopted from Table 2-2. The red dotted line is a power fit and has been used to predict number of cells needed to encode entire stimuli (green dot). The predicated green dot here points to about 90 cells as the required quantity of cells needed to encode the stimuli (contains three bird songs=207s). Out of the two blue circles marked here, one is pointing to three recordings with the same number of cells (10 cells) and the other is pointing to three recordings with 30 cells that correspond to similar encoding percentages.

2.4.5 *Reconstruction of encoded stimuli by CRFs*

Through CRFs spatial-temporal map, we were able to encode the stimuli by spotting pick activation of receptive fields with their corresponding stimuli portions. In this section we demonstrate practically what this encoding mechanism does.

Figure 2-7 displays an example of this method to find a portion of stimuli related to a pool of CRFs. Here 20 CRF features, 10 facilitatory and 10 suppressive, have been adopted from one cell (subject2-pen2-cell#1). By spotting pick activations of CRFs we are able to define stimuli corresponding time windows (Figure 2-7A). Time windows in red belong to facilitatory responses

and the ones in blue belong to suppressive responses. Figure 2-7B displays the 20 facilitatory and suppressive CRFs of cell#1. CRFs corresponding stimuli locations are shown in Figure 2-7C. Lastly stimuli portions associated with each CRF are displayed in Figure 2-7D. If we stitch these CRFs together based off their temporal organization and compare them with their corresponding stimuli portions, it appears that the stitched CRFs contain a fair amount of information about their corresponding stimuli potions (Figure 2-8B-C). This is due to the fact that we captured the receptive field responses by use of the quadratic MNE model.

Figure 2-8D displays a linear receptive field (LRF) of 12 cells from the same subject and penetration. As it appears, quadratic CRFs contain considerable information from stimuli compared to LRF and this might offer a possibility of rebuilding and reconstructing stimuli from CRFs especially from a large population of cells. On the other hand, LRFs that are extracted from linear parameter of the MNE model (h), not only do not capture enough variations from the stimuli but also are limited to one feature per cell as opposed to CRFs that can be extracted in large numbers from each cell.

If we extend this idea and locate portions of stimuli related to each CRF for a population of cells, we able to produce a connectivity map between cells (Figure 2-8A). Likewise, this connectivity map can be observed from histogram of spatial-temporal map. Figure 2-8A demonstrate an example of a snap shot of connectivity map between small populations of 10 cells. Here it can be observed that some cells are sharing similar CRF features (e.g. C7, C8, and C10 in second column), some cells are containing one unit CRF (e.g. C5 in forth column), and some cells are not exhibiting any CRF responses towards parts of stimuli (white empty spaces).

This observation draw attention to the fact where a network of neurons, actively process part of stimuli and ignore the rest of it to avoid over use of memory ((Anderson, 2004) & (Johnson,

2004)). In addition, this connectivity map across cells, varying by changes in stimuli which this can be indications of cell response flexibility and short-term plasticity ((James, 1890) & (Pascual, 2005)). All these facts are observed for both facilitatory in red frames and suppressive responses in blue frames.

Furthermore, we predict the dotted lines will be filled more, as the population of cells grow e.g. to 90 cells (Figure 2-6). This means that with an appropriate size neuron population, we possibly able to encode entire stimuli with sufficient accuracy. Overall, comparison of B, C, and D rows of Figure 2-8 show receptive fields created by a full MNE model capture much more spectro-temporal modulation from the stimulus compared to the linear receptive fields. This fact indicates that composite receptive field is a candidate for reconstructing stimuli.

Figure 2-7: Finding portions of stimuli related to each CRF.
(A) Time window (20 bins=400ms) where each CRF exhibits peak activation with a portion of stimuli. Time windows in red are facilitatory and time windows in blue are suppressive responses. (B) 20 CRFs extracted from one cell (subject 2- pen2-cell #1) with 10 facilitatory and 10 suppressive responses. (C) Top: Spectrogram of 3 bird songs. Bottom: CRFs temporal location based on their pick activation with stimuli (r >60%). (D) Corresponding stimuli portions to CRFs based on their temporal locations.

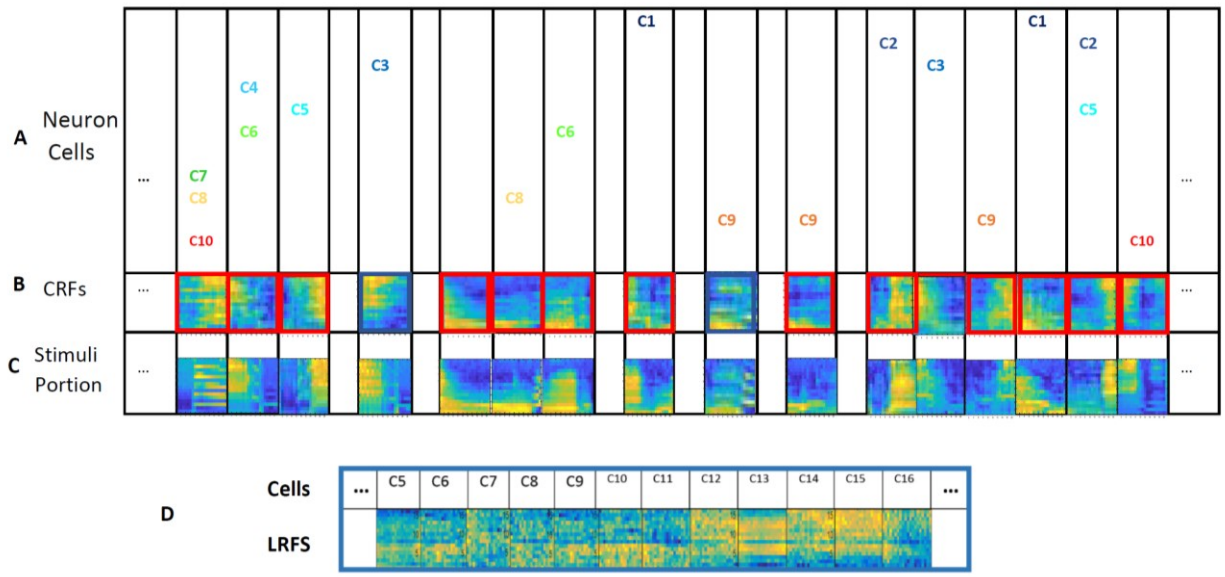

Figure 2-8: Cells connectivity map and reconstruction of stimuli by CRFs.
(A) A snap shot of connectivity map between small populations of 10 cells. Some cells are sharing similar CRF features (e.g. C7, C8, and C10 in second column), some cells are containing one unit CRF (e.g. C5 in forth column), and some cells are not exhibiting any CRF responses towards parts of stimuli (white empty spaces). (B) Temporally organized CRF features. Facilitatory CRFs are shown by red frames and suppressive CRFs are shown by blue frames. (C) Stimuli reconstruction: Stimuli portions corresponding to each individual CRF are found by the method from Figure 2-7 and stitched together. Dotted lines will be further populated as the population of cells grow. (D). Linear receptive fields (LRFs) of 12 cells extracted from a first order MNE model (h parameter).

2.4.6 *Reconstruction of novel stimuli with CRFs*

From the previous section we learned CRFs embody a sufficient amount of information about the stimuli. This has encouraged us to test the hypotheses of whether we are able to utilize the existing CRFs pool to rebuild portions of novel stimuli. To begin, we obtain 49 novel songs which have already been played for the subjects during brain response recordings. These songs are considered novel since we have not tested them in our analysis. These novel songs are of different lengths and vary from 30s to 90s (Figure 2-9). They were concatenated and divided into 49 equal lengths. These 49 song pieces are tested against 646 CRFs. The 646 CRFs are the shared CRFs between cells across pool of 3080 CRFs (see sections 2.4.1& 2.4.2)) and they are generated from

training set of concatenated three bird songs. These CRFs are tested on each piece of novel stimuli separately. Cross correlation has been used, as the prediction model, between 646 CRFs and each piece of 49 novel stimuli to find the number of existing CRFs in each piece of novel stimuli (Figure 2-9). Figure 2-9A displays the 49 novel song spectrograms. Figure 2-9B illustrates the percentage of CRFs which exist in the 49 novel stimuli in the form of bar graphs. Existing CRFs and their corresponding stimuli portions can be pull out and reconstructed from each bar. Figure 2-9C (top) displays an example of the temporally organized CRFs pulled out from a bar related to song portion #6. The CRFs corresponding stimuli portions are shown underneath.

In conclusion, in this section it is proven that our hypothesis is correct and we are able to rebuild portions of stimuli for each of 49 novel songs by utilizing rather small pool of CRFs generated from 3 songs. The percentage of novel song reconstructions vary from 0.5 % to 4.3 %. To increase reconstruction percentage, CRFs should be extracted from a larger training set (larger song populations) and be tested on one novel song at a time.

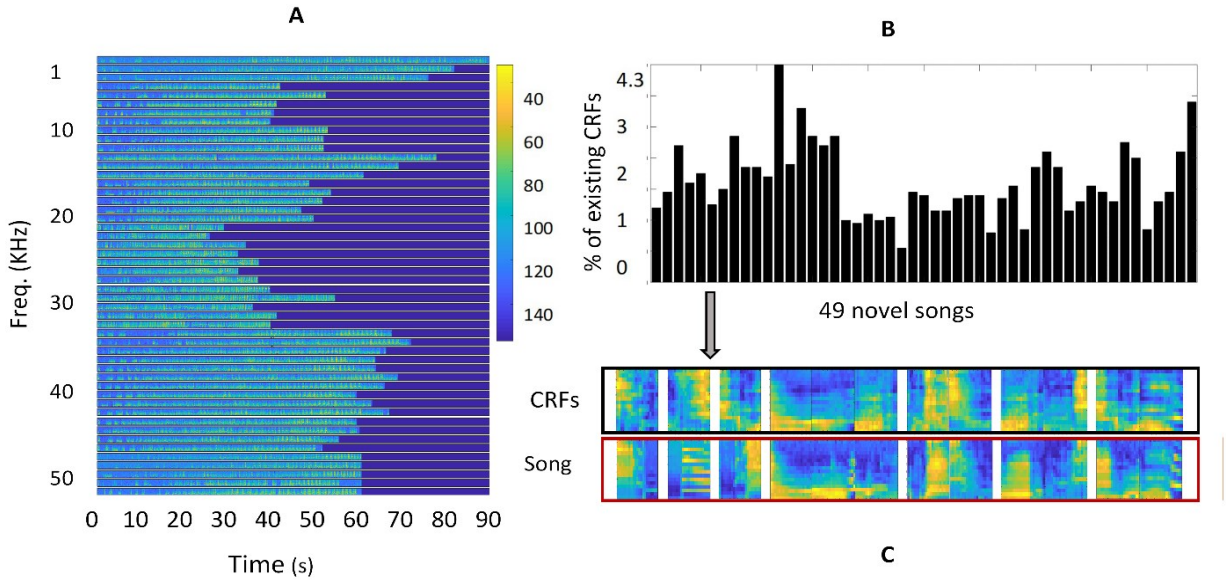

Figure 2-9: Reconstructing of novel stimuli from pool of existing CRFs.
(A) Spectrogram of 49 novel bird songs 30s to 90s long with frequency range 750-12KHz. (B) Barographs display percentage of existing CRFs in each pieces of 49 equal length novel song (trained on 3 songs and tested on one novel song at a time). (C) Top: Demonstration of reconstruction of a portion of a novel stimuli (song # 6) from figure B (indicated by a gray arrow) based on existing CRFs. The white regions will be further populated by utilizing CRFs from larger training sets (bird songs). Bottom: Corresponding CRF stimuli portions identified and temporally organized to rebuild a portion of song#6.

2.4.7 *Prediction of brain responses by CRFs*

In this section we examine another hypothesis to test whether we can use CRFs as a tool to predict brain responses. To create and investigate CRFs properties through this study, we have concentrated on the first 20 significant facilitatory and suppressive CRFs. On average, among the cells, the first 20 features contain the least amount of noise. In order to predict brain response we first need to extract CRFs from the J-matrix. Since the J-matrix design in this study originally has 320 dimensions (16 freq.*20 time bins) we need to lower its rank to 20 to generate the first 20 CRFs. Here singular value decomposition (SVD) has been employed to reduce the rank of the J-matrix. Figure 2-10A displays the original J-matrix (320) and its singular values for a cell. Underneath the reduced rank J-matrix from 320 to 20 (J_r) has been shown. By utilizing SVD we

first deconstruct the J-matrix then reconstruct it with a reduced set of singular values. The equation bellow briefly explains this process.

Equation 2

$$[\mathbf{U}, \mathbf{S}, \mathbf{V}] = \mathbf{svd}(\mathbf{J})$$
$$\boldsymbol{U}(\mathbf{320}\boldsymbol{x}\mathbf{320}) * \boldsymbol{S}(\mathbf{320x320}) * \mathbf{V}'(\mathbf{320x320}) \rightarrow \boldsymbol{U}(\mathbf{320}\boldsymbol{x}\mathbf{20}) * \boldsymbol{S}(\mathbf{20x20}) * \mathbf{V}'(\mathbf{20x320})$$

Where:
S: Singular values (square roots of the eigenvalues in decreasing order)
U: Left singular vectors
V: Right singular vectors

After obtaining low rank J (J_r), the below equation is used to predict spike train response.

Equation 3

$$\text{Prediction of response (control)} = \frac{\mathbf{1}}{\mathbf{1}+\boldsymbol{e}^{(\mathbf{a}+\mathbf{stimuli}*\mathbf{h}\prime+\mathbf{sum}\,(\mathbf{stimuli}.*(\mathbf{stimuli}*\mathbf{J}-\mathbf{r})))}}$$

Where: a, h, and J_r are belong successively to a constant, linear, and quadratic parameters of receptive fields. To examine this prediction equation we first run a control test on it. For this, a cell that has responded to three original bird songs with 20 response trials is chosen. Subsequently, 15 of these trials were used for training and parameters a, h, and J were estimated. These parameters then have been utilized to predict the 5 remaining trial averages (Figure 2-10C). In this figure, the black curve demonstrates the trial average of original brain response to one bird song (60s) and the red curve is the predicted response. This prediction control test has been conducted on 10 cells. The average response prediction range is 65% (Figure 2-10E).

After testing the reliability of the prediction equation now we aim to predict brain responses to 49 novel stimuli. To perform this test, a cell with 49 response trials to 49 novel songs is chosen. 48 of these trials are used for training and parameters a, h, and J are estimated. Next, these parameters are used to test and predict one remaining trial response (Equation 4).

Equation 4

$$\text{Prediction of response for one novel song from 49 novel songs} = \frac{\mathbf{1}}{\mathbf{1}+e^{(\mathbf{a}+\mathbf{one\ novel\_stimuli}*\mathbf{h}\prime+\mathbf{sum}(\mathbf{one\ \ novel\_stimuli}.*(\mathbf{one\ \ novel\_stimuli}*\mathbf{J})))}}$$

Subsequently this prediction process is repeated for all 49 novel responses. Figure 2-10D demonstrates the concatenated 49 predicted responses for one cells in red curve versus the concatenated original 49 responses for one cell. Finally this test has been conducted on 10 cells. In Figure 2-10E the bar graph on the right side displays the range of response prediction for 49 novel songs across 10 cells. Although the prediction median is about 60%, the predication range varies mostly from 25% to 85%.

This result indicates our hypothesis is correct and we are able to predict brain responses by use of CRFs although in a wide range.

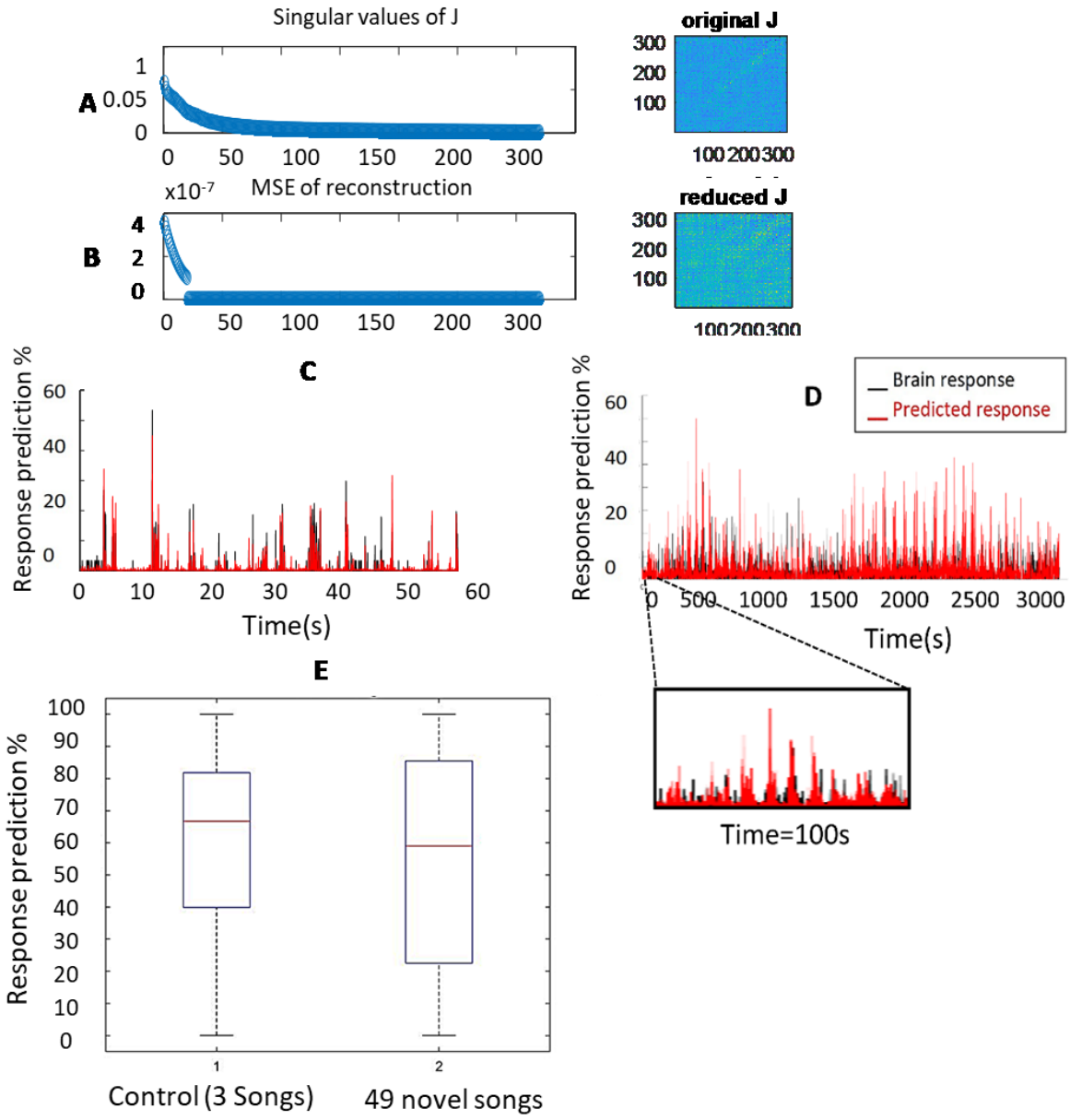

Figure 2-10: Prediction of brain response by CRFs.
(A) Reducing rank of J-matrix from 320 to 20. Left: singular values of J. Right: Full rank J-matrix with 320 dimensions (CRFs). (B) Left: Mean square error between (J, J_r) drops after 20 significant CRFs. Right: Reconstructed low rank J-matrix. (C) Example of a prediction of a cell response as a control test based on its response trials (train on 15 trials and test on 5 trials) for 3 song stimuli. The black curve shown is the original cell response. The red curve is the predicted response. (D) Example of prediction of a cell response for 49 novel songs (train on 48 songs and test on one song). Repeated predictions of response of all 49 songs concatenated here. Zoom into first 100s of the figure has been displayed underneath. (E) Prediction of control response on 3 known songs compared with the prediction of response for 49 novel songs across 10 cells in box-plot forms. Prediction of response for control test has median of 65% and prediction of response for 49 novel songs has median of 60% with wider range than control test.

2.5 Conclusion

Population coding is a technique to process joint activates of populations of neurons in order to represent and reconstruct stimulus. Each individual neuron has a unique distribution of output in response to input stimuli however, studies have shown that it is the combination of neuron responses, in a population that carry the most amount of information about the input stimuli ((Wu, 2002) , (Rieke F. W., 1997) & (Machens, 2004)).

Although there are studies have been done on this area still we lack the tools to comprehend this coding mechanism (Yildiz, 2016) & (Badel, 2008). Recently, we've shown that neurons in secondary auditory cortical regions of European starling song birds have composite receptive fields (CRF) (Kozlov & Gentner, 2016) .In this study we have utilized a population of CRFs as a tool to investigate neural population encoding and decoding for first time.

To generate CRFs from neuron cells Maximum noise entropy model (MNE) has been adopted (Fitzgerald, 2011a). The MNE quadratic model has proved most effective compared with some of the existing models such as STA, STC, and MID ((Bialek, 2005), (Steveninck, 1988), and (Sharpee, 2004)). The MNE model does not have a limitation working with natural stimuli and can extract a large number of CRF features from cell responses ((Sharpee, 2004) & (Kell, 2018)).

By utilizing the MNE model, a large pool of facilitatory and suppressive CRFs are created from 154 auditory NCM cells from nine recording sessions across five European starling birds. Since high quality CRFs generated from stimuli-locked cells with low noise are preferred, a combination of techniques are suggested to remove noisy trials from cells if required ((Van der Maaten & Hinton, 2008) & (Ester, 1996)).

To investigate the decoding and encoding mechanism, first a spatial-temporal map was

created from the assembled CRF pool. Spatial term of map is referred to the dorsal-ventral organizations of population of 154 cells and temporal term denoted to location of pick activation of each CRF with specific part of stimuli. The CRFs spatial-temporal map reveals that neurons are encoding stimuli, temporally uniform however their emphasis on of each encoded stimuli portion varies. Besides, investigating relationship between similarities of CRFs of cells and the relative distances of cells revealed that cells' relative distances along dorsoventral plan is independent of cell response similarities. This suggests stimuli encoding by a population of neurons is independent of neuron locations and their topology.

Besides introducing this novel encoding mechanism, the spatial-temporal map contains other remarkable properties. For instance, by counting flat temporal location of CRFs, not only do we find the percentage of stimuli encoding for different population sizes but also we are able to predict number of cells needed to encode entire stimuli.

Another property of CRFs found in this study is their ability to practically reconstruct stimuli. In this study we have shown CRFs contains a sufficient amount of information about their corresponding stimuli portions. This is due to the fact that we captured CRFs by use of a quadratic MNE model instead of a linear model. Thus, by monitoring pick activation of CRFs with the stimuli, we can locate encoded corresponding stimuli portions to each CRF. With this information not only we were able to rebuild and reconstruct stimuli from CRFs for individual cells as well their population but also we were able create a connectivity map between these cells population.

The cells connectivity map have revealed, some cells are sharing similar CRF features, some cells are containing one unit CRF, and some cells are not exhibiting any CRF while stimuli is presenting. This observation accentuate the fact where a network of neurons, actively process part of stimuli and overlook the remaining to avoid over consumption of memory ((Anderson,

2004) & (Johnson, 2004)). Moreover, this connectivity map across cells, varying by changes in stimuli which this can be indications of cell response flexibility and short-term plasticity ((James, 1890) & (Pascual, 2005)).

To push the boundaries of understanding CRF properties further, we have utilized them to predict novel stimuli as well as novel brain responses. The result showed novel stimuli can be predicated and reconstructed with a fair accuracy, especially if stimuli training set is large enough. Likewise, brain responses were predicated and reconstructed with a reasonable accuracy by CRFs.

Finally, all these facts were tested on both facilitatory and suppressive CRF responses and the results have been revealed a similar neural coding mechanisms between both of these responses.

Overall, this study has shown composite receptive fields can be used as a new tool to unlock abundant information about neural coding mechanisms in a population of neurons.

2.6 **Acknowledgements**

Chapter 2, in full, is in preparation for publication as: Nasim W. Vahidi., and Timothy Q. Gentner. “Neural population coding by composite receptive fields in songbird auditory region”. The dissertation author was the primary investigator and author of this manuscript.

2.7 **References**

Anderson, J. R. *Cognitive psychology and its implications*. 2C J. (2004). Cognitive Psycho

Ayala, Y. A., & Malmierca, M. S. (2012). Stimulus-specific adaptation and deviance detection in the inferior colliculus. *Frontiers in Neural Circuits*, *6*, 89. https://doi.org/10.3389/FNCIR.2012.00089

Baddeley, A. (2013). *Essentials of Human Memory (Classic Edition)*. https://doi.org/10.4324/9780203587027

Badel, L., Lefort, S., Berger, T. K., Petersen, C. C. H., Gerstner, W., & Richardson, M. J. E. (2008). Extracting non-linear integrate-and-fire models from experimental data using dynamic I–V curves. *Biological Cybernetics*, *99*(4–5), 361–370. https://doi.org/10.1007/s00422-008-0259-4

Bialek, W., De Ruyter Van Steveninck, R. R., & Tishby, N. (2006). Efficient representation as a design principle for neural coding and computation. *2006 IEEE International Symposium on Information Theory*, 659–663. https://doi.org/10.1109/ISIT.2006.261867

Bialek, W., & van Steveninck, R. R. de R. (2005). *Features and dimensions: Motion estimation in fly vision*. Retrieved from http://arxiv.org/abs/q-bio/0505003

Dayan, P., & Abbott, L. F. (2001). *Theoretical neuroscience : computational and mathematical modeling of neural systems*. Massachusetts Institute of Technology Press.

De Boer, R., & Kuyper, P. (1968). Triggered correlation. *IEEE Transactions on Bio-Medical Engineering*, *15*(3), 169–179. Retrieved from http://www.ncbi.nlm.nih.gov/pubmed/5667803

Eggermont, J. J., Epping, W. J. M., & Aertsen, A. M. H. J. (1983). Stimulus dependent neural correlations in the auditory midbrain of the grassfrog (Rana temporaria L.). *Biological Cybernetics*, *47*(2), 103–117. https://doi.org/10.1007/BF00337084

Ester, M., Kriegel, H.-P., Sander, J., & Xu, X. (1996). *A Density-Based Algorithm for Discovering Clusters in Large Spatial Databases with Noise*. Retrieved from www.aaai.org

Fitzgerald, J. D., Rowekamp, R. J., Sincich, L. C., & Sharpee, T. O. (2011). Second Order Dimensionality Reduction Using Minimum and Maximum Mutual Information Models. *PLoS Computational Biology*, *7*(10), e1002249. https://doi.org/10.1371/JOURNAL.PCBI.1002249

Fitzgerald, J. D., Sincich, L. C., & Sharpee, T. O. (2011). Minimal Models of Multidimensional Computations. *PLoS Computational Biology*, *7*(3), e1001111. https://doi.org/10.1371/journal.pcbi

Harris, K. D., & Woolley, S. (2015). Cortical computation in mammals and birds. *Proceedings of the National Academy of Sciences of the United States of America*, *112*(11), 3184–3185. https://doi.org/10.1073/pnas.1502209112

James, W., Burkhardt, F., Bowers, F., & Skrupskelis, I. K. (1981). *The principles of psychology*. Harvard University Press.

Johnson, A., & Proctor, R. W. (2004). *Attention : theory and practice*. Sage Publications.

Kaardal, J. T., Theunissen, F. E., & Sharpee, T. O. (2017). A Low-Rank Method for Characterizing High-Level Neural Computations. *Frontiers in Computational Neuroscience*, *11*, 68. https://doi.org/10.3389/fncom.2017.00068

Karten, H. J. (2013). Neocortical Evolution: Neuronal Circuits Arise Independently of Lamination. *Current Biology*, *23*(1), R12–R15. https://doi.org/10.1016/j.cub.2012.11.013

Kell, A. J. E., Yamins, D. L. K., Shook, E. N., Norman-Haignere, S. V, & Mcdermott, J. H. (n.d.). *A Task-Optimized Neural Network Replicates Human Auditory Behavior, Predicts Brain Responses, and Reveals a Cortical Processing Hierarchy In Brief*. https://doi.org/10.1016/j.neuron.2018.03.044

Koyama, S. (2012). On the Relation Between Encoding and Decoding of Neuronal Spikes. *Neural Computation*, *24*(6), 1408–1425. https://doi.org/10.1162/NECO_a_00279

Kozlov, A. S., & Gentner, T. Q. (2016). Central auditory neurons have composite receptive fields. *Proceedings of the National Academy of Sciences*, *113*(5), 1441–1446. https://doi.org/10.1073

Maaten, L. van der, & Hinton, G. (2008). Visualizing Data using t-SNE. *Journal of Machine Learning Research*, *9*(Nov), 2579–2605. Retrieved from http://www.jmlr.org/papers/v9/vandermaaten08a.html

Machens, C. K., Wehr, M. S., & Zador, A. M. (2004). Linearity of Cortical Receptive Fields Measured with Natural Sounds. *Journal of Neuroscience*, *24*(5), 1089–1100. https://doi.org/10.1523/JNEUROSCI.4445-03.2004

Masamoto, K., & Kanno, I. (2012). Anesthesia and the Quantitative Evaluation of Neurovascular Coupling. *Journal of Cerebral Blood Flow & Metabolism*, *32*(7), 1233–1247. https://doi.org/10.1038/jcbfm.2012.50

Pascual-Leone, A., Amedi, A., Fregni, F., & Merabet, L. B. (2005). THE PLASTIC HUMAN BRAIN CORTEX. *Annual Review of Neuroscience*, *28*(1), 377–401. https://doi.org/10.1146/annurev.neuro.27.070203.144216

Pasley, B. N., David, S. V., Mesgarani, N., Flinker, A., Shamma, S. A., Crone, N. E., … Chang, E. F. (2012). Reconstructing Speech from Human Auditory Cortex. *PLoS Biology*, *10*(1), e1001251. https://doi.org/10.1371/journal.pbio.1001251

Ranson, A. (2017). Stability and Plasticity of Contextual Modulation in the Mouse Visual Cortex. *Cell Reports*, *18*(4), 840–848. https://doi.org/10.1016/j.celrep.2016.12.080

Rieke, F., Bodnar, D. A., & Bialek, W. (1995). Naturalistic stimuli increase the rate and efficiency of information transmission by primary auditory afferents. *Proceedings of the Royal Society of London. Series B: Biological Sciences*, *262*(1365), 259–265. https://doi.org/10.1098/rspb.1995.0204

Rieke, F. (1997). *Spikes : exploring the neural code*. MIT Press.

Rob R. de Ruyter van Steveninck, W. B. (1988). Real-time performance of a movement-sensitive neuron in the blowfly visual system: coding and information transfer in short spike sequences. *Proceedings of the Royal Society of London. Series B. Biological Sciences*, *234*(1277), 379–414. https://doi.org/10.1098/rspb.1988.0055

Rossant, C., Kadir, S. N., Goodman, D. F. M., Schulman, J., Hunter, M. L. D., Saleem, A. B., … Harris, K. D. (2016). Spike sorting for large, dense electrode arrays. *Nature Neuroscience*, *19*(4), 634–641. https://doi.org/10.1038/nn.4268

Schäfer, P. J., Corona-Strauss, F. I., Hannemann, R., Hillyard, S. A., & Strauss, D. J. (2018). Testing the Limits of the Stimulus Reconstruction Approach: Auditory Attention Decoding in a Four-Speaker Free Field Environment. *Trends in Hearing*, *22*, 233121651881660. https://doi.org/10.1177/2331216518816600

Schoups, A., Vogels, R., Qian, N., & Orban, G. (2001). Practising orientation identification improves orientation coding in V1 neurons. *Nature*, *412*(6846), 549–553. https://doi.org/10.1038/35087601

Schwartz, O., Chichilnisky, E. J., & Simoncelli, E. P. (2002). *Characterizing Neural Gain Control using Spike-triggered Covariance* (pp. 269–276). pp. 269–276. Retrieved from https://papers.nips.cc/paper/1975-characterizing-neural-gain-control-using-spike-triggered-covariance

Schwartz, O., Pillow, J. W., Rust, N. C., & Simoncelli, E. P. (2006). Spike-triggered neural characterization. *Journal of Vision*, *6*(4), 13. https://doi.org/10.1167/6.4.13

Sharpee, T., Rust, N. C., & Bialek, W. (2004). Analyzing Neural Responses to Natural Signals: Maximally Informative Dimensions. *Neural Computation*, *16*(2), 223–250. https://doi.org/10.1162/089976604322742010

Sherrington, C. S. (1906). Observations on the scratch-reflex in the spinal dog. *The Journal of Physiology*, *34*(1–2), 1–50. Retrieved from http://www.ncbi.nlm.nih.gov/pubmed/16992835

Stanley, G. B., Li, F. F., & Dan, Y. (1999). Reconstruction of natural scenes from ensemble responses in the lateral geniculate nucleus. *The Journal of Neuroscience : The Official Journal of the Society for Neuroscience*, *19*(18), 8036–8042. Retrieved from http://www.ncbi.nlm.nih.gov/pubmed/10479703

Theunissen, F. E., Sen, K., & Doupe, A. J. (2000). Spectral-temporal receptive fields of nonlinear auditory neurons obtained using natural sounds. *The Journal of Neuroscience : The Official Journal of the Society for Neuroscience*, *20*(6), 2315–2331. Retrieved from http://www.ncbi.nlm.nih.gov/pubmed/10704507

Van Steveninck, R. R. de R. (1988). Real-time performance of a movement-sensitive neuron in the blowfly visual system: coding and information transfer in short spike sequences. *Proceedings of the Royal Society of London. Series B. Biological Sciences*, *234*(1277), 379–414. https://doi.org/10.1098/rspb.1988.0055

Wu, S., Amari, S., & Nakahara, H. (2002). Population Coding and Decoding in a Neural Field: A Computational Study. *Neural Computation*, *14*(5), 999–1026. https://doi.org/10.1162/089976602753633367

Yildiz, I. B., Mesgarani, N., & Deneve, S. (2016). Predictive Ensemble Decoding of Acoustical Features Explains Context-Dependent Receptive Fields. *The Journal of Neuroscience*, *36*(49), 12338–12350. https://doi.org/10.1523/JNEUROSCI.4648-15.2016

Zion Golumbic, E. M., Ding, N., Bickel, S., Lakatos, P., Schevon, C. A., McKhann, G. M., … Schroeder, C. E. (2013). Mechanisms Underlying Selective Neuronal Tracking of Attended Speech at a "Cocktail Party." *Neuron*, *77*(5), 980–991. https://doi.org/10.1016/j.neuron.2012.12.037

CHAPTER 3

Stimulus evoked single units recorded from starlings brain surface

3.1 **Abstract**

The distinctive physical properties of nanostructures such as electrochemical sensing made them attractive materials to be used in different fields of science including neuroscience ((Wise, 2007); (Chang-Hsiao, 2010); (Amaral, 2013)). In this study platinum nanorods (one-dimensional) in the form of surface electrodes have been utilized for electrical recording from the surface of the brain. One-dimensional (1D) nanorods are particularly attractive because they can cover a large surface area of the cortex, enhanced electric fields at their tips (Banerjee, 2004), and the emergence of high-index crystalline facets at their circumference (Shen, 2015) which cumulatively facilitate electrochemical interactions. The surface platinum nanorad (PtNR) sites are made by selective dealloying (Yoo, 2007), which are aligned on top of metal leads that are bound on a fixable film. Before we conduct neural recording, we characterize the PtNR arrays. They exhibit very low electrochemical impedances and high charge injection capacities at various length scales. In general, combination of distinctive features such as low impedance, stable and scalable recording sites, flexible substrate, and biocompatible materials make PtNR arrays suitable candidates for neural recording, especially from the cortical surface. Recording with PtNR microelectrode arrays from the surface of the auditory region of song birds, demonstrated brain activity at a cellular resolution. Significantly, strong modulations of single cell activities as well as local field potentials by auditory stimuli are detected from the cortical surface of the birds. Subsequently, we were able to extract composite receptive fields from the recorded single cells on the surface. This development paves the way for high fidelity and less invasive brain-machine interfaces, which could support devices that operate on the principle of highly efficient electrochemical catalytic processes. In addition, thin PtNR microelectrode arrays can be utilized to study sensory receptive field mechanisms and their relationship to the stimuli on the surface of the brain.

3.2 Introduction

There are numerous demonstrations that exploit the unique properties of 1D nanowires in interfacing with biological tissue at multiple scales including cellular ((Tian, 2010) ; (Liu, 2017)), in-vitro cultured tissue (Dai, 2016) as well as in-vivo from intact retina (Hong, 2018) and brain tissue (Fu, 2017). However, the unique electrochemical properties of 1D structures have not been used in large scale electrodes that can interface with the living brain, partly because of the growth of 1D nanowires is carried out at high temperatures ((Wagner, 1964); (Sun, 2018)) that are incompatible with flexible substrates that are required for brain interfaces. Fabrication methods are readily available to form 1D nanostructures (Greene, 2006) but their applicability to Platinum, the most known biocompatible material that is widely used in clinical practice, is yet to be demonstrated. Most commonly, 1D Pt nanostructures can be grown by electrochemical deposition ((Li, 2013), (Liu, 2009), (Li, 2009), (Shui, 2011), (Jin, 2009), and (Tominaka, 2010)) but suffer from stability issues. They are also problematic due to toxic ligand additives, metal elements and/or isotopes.

In this study we discuss fabrication of Pt nanorods (PtNRs) on thin and flexible parylene C substrates. The selective chemical dissolution of metal alloys technique has been utilized to create nanoporous structures (Erlebacher, 2001). High resolution transmission electron microscopy (HRTEM) imaging that has been used in this study has demonstrated that the PtNR is polycrystalline and porous. Moreover, uniform distribution of the PtNRs across a single microelectrode has been visualized by an optical and scanning electron microscope (SEM).

Following, electrochemical characterizations such as, electrochemical impedance spectroscopy, cyclic voltammetry (CV), and voltage transients (VTs) are performed on these thin films with 32 microelectrodes. Biocompatibility and the mechanical stability of PtNRs are tested

in-vivo by implanting the device in a mouse cortex for 42 days. Histological analysis demonstrated near normal neuronal distribution with minimal glial and astrocyte response in the implanted site compared to the contralateral site. The explanted device was examined by SEM and showed intact PtNRs underneath the adsorbed tissue on the microelectrode.

To exploit brain electrical recording ability of PtNR microelectrodes , PtNRs array with 32 electrode sites have been implanted on the surface of the HVC (high vocal center) of European starling songs birds as well as zebra finches which possess similar functions in their auditory region to that of humans at cellular levels ((Karten, 2013) & (Harris K. , 2015)).

To examine the quality of recording from this new surface electrode array, a commercial depth electrode with 16 sites has also been inserted to the HVC area via an open window on the surface array. After implanting both the PtNR surface array and depth electrode, neural data was recorded from both electrodes simultaneously. Recorded data reveled the PtNR surface electrodes are capable of registering action potential waveforms from single cells similar to the control depth electrode. The quality of the recorded single cells furthermore were tested by extracting low noise composite receptive fields (CRFs) from them. Low noise CRFs usually are generated from cells that are stimulus-locked and contain minimum noise. In addition, the local field potential signals recorded by all the 48 sites (32 sites of surface array and 16 sites of depth electrode) demonstrate that there are more correlation between channels on PtNR surface electrode in comparison to channels on depth electrodes.

This study demonstrates not only that PtNRs are biocompatible and robust but can potentially be used as novel microelectrode coatings on chronic implants. They are also capable of recording high quality neural data such as LFP, spikes, single cells, multi-units, and composite receptive fields from the cortical surface of the brain. Overall, thin PtNR microelectrode arrays

highlight the potential for minimally invasive neuroprosthetic applications as well as introducing a tool to map and study neural activities and receptive fields on the cortical surface of the brain.

3.3 **Method**

3.3.1 ***Device fabrication and characterization***

The fabrication of the PEDOT:PSS and Pt devices used in the electrochemical benchtop tests is similar to previously established protocols ((Ganji, 2018) & (Uguz, 2016)). The fabrication process of PtNR-based electrodes extends these protocols and is reported elsewhere (Ganji, 2019). An Axioscope Optical microscope and FEI SFEG ultra high-resolution SEM at 10 kV accelerating voltage were used to characterize the devices. For TEM characterization, the devices were coated with 1μm SiN_x protection layer and a 30nm Pt layer and then sliced by a focused ion beam (FIB) to view the cross-section of the microelectrodes. EIS was performed using a GAMRY interface 1000E in 0.01 M phosphate buffer saline (×1 PBS) solution, using a three-electrode configuration, i.e., Ag/AgCl electrode as a reference electrode, a large platinum electrode as a counter electrode, and the target micro/macro-dot array as the working electrode (Figure 3-1).

3.3.2 ***Electrophysiology and data acquisition***

These experiments were performed on European starling song birds as well as zebra finches under anesthesia. The auditory HVC brain region in song birds which is known to be responsible for song production and vocal learning (Brainard & Doupe, 2002), has been targeted for craniotomies. The PtNR surface probe is then placed on the HVC after which a 16 channel depth probe (NeuroNexus) is slowly lowered into the HVC via an open window on the array. Following,

pre-recorded bird songs such as native starling and zebra finch songs were played back for the subjects in thirty random trials. The bird songs were recorded at 44.1 KHz.

Intan RHD2000 (Intan Technologies, Los Angeles, CA) recording system along Open Ephys GUI (Black, 2017) or RHD2000 software have been utilized to record electrophysiological data from both surface and depth probes. The Intan RHD2000 USB Controller, Flex Adapter board, and RHD2116 head stage were serially connected to the probes. Recorded data was sampled at 30 kHz with a cutoff frequency 0.01-7.5 kHz. Later this data was divided into two sets by low pass filtering under 300Hz and high pass filtering above 300Hz. Spike sorting and clustering was performed through KiloSort program (Pachitariu, 2016). Clusters were then sorted to three groups of single unit (SUA), multi-unit (MUA), and noise based on their refractory period (Dayan & Abbott, 2000). Clusters with little to no spikes between 0 to 2 ms from the previous spike were considered single unit. Clusters containing many spikes with refractory periods less than 2ms were considered multi-unit.

3.3.3 *Analysis and Statistical Methods*

The spike waveforms in Figure 3-3c and Figure 3-5a are extracted from single unit clusters. The red waveforms are averages of 20 uniformly sampled spike snippets. The black scales on the lower right of each waveform indicates a 50 μV amplitude. The inter-spike intervals (ISI) are the time between succeeding spikes of a neuron. The ISI histogram of spike waveforms shown in these figures indicate the distribution of the log of ISI, which can be a visual tool to track violation of refractory period and differentiate single cells from multi-unit type. Besides extracting waveforms from clusters, we can examine their quality and whether they are related to real neural cells or noise. One way to conduct this test is to monitor cell activity in

response to stimulus with repeated trials. If a cell response shows any stimulus locking property, this can be an indication of an actual cell activity rather than an artifact.

Figure 3-3d is an example of a recorded cell from the surface of the brain with a stimulus locking response over 30 trials. The first row shows the spectrogram of a 28 second native bird song stimulus. To create this spectrogram, bird song is converted to spectrograms by use of a Matlab spectrogram function with parameters nfft=128, and a Hanning window of nfft with 50% overlap. It contains 65 frequency bands in the 0-10KHz range. The second row shows an example of one channel (Ch1) raw data in blue. The raw data contains both low and high frequency information. The green wave shown underneath is the high pass filtered raw data (Freq.>300Hz) and contains spikes. At the bottom of the figure, 30 trials are averaged and a raster plot of spike trains in response to 30 song trials are shown in red.

Figure 3-2e shows a detailed view of 5s from

Figure 3-3d. In this figure, on the spectrogram plot, a logarithm of power spectrum density (PSD) is averaged over 65 spectrogram frequency bands and is shown in black. Underneath in black, the average of 65 frequency bands of PSD is calculated for a 5s stimulus.

3.4 **Result**

3.4.1 ***Overview of PtNR Properties***

Figure 3-1 show a picture and a microscope image of the PtNR microelectrodes on flexible parylene C. PtNR is polycrystalline and porous, both of which are beneficial for electrochemical activity. The optical and scanning electron microscope imaging indicate uniform distribution across PtNRs microelectrodes. The thin film fabrication process is high-yield and uniform, embodied in overlapping electrochemical impedance spectroscopy (EIS), cyclic voltammetry

(CV), and voltage transients (VTs). To demonstrate the biocompatibility and the mechanical stability of PtNRs in vivo, the device was implanted on a mouse brain cortex and performed immune-histological staining, the result have shown minimal glial and astrocyte response.

In total, these results demonstrate the biocompatibility and robustness of the PtNRs as novel microelectrode coatings, with potential for chronic implants.

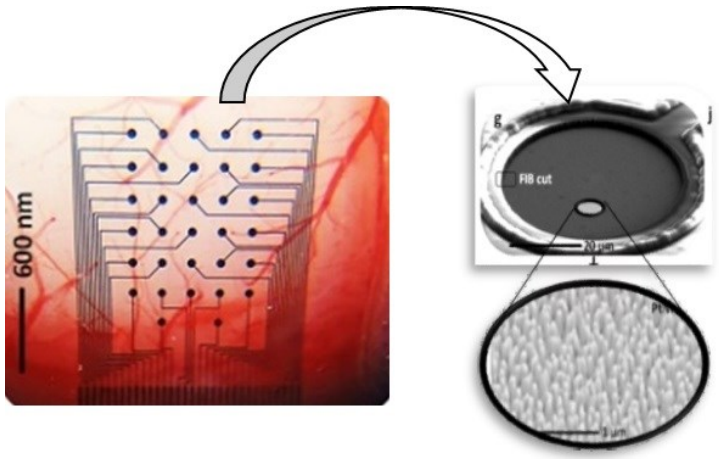

Figure 3-1: PtNR microelectrodes on a flexible substrate.
Right: A picture of implanted PtNR device on starling bird HVC region. The array contains thin film parylene C. It is 500nm thick with embedded microelectrodes (Dimeter=50 µm). Left: A magnified image of porous polycrystalline structure of Pt nanorods. Each nanorod on average has 100nm dimeter and 500nm height.

3.4.2 *Electrical recording*

The superior electrochemical properties of PtNR microelectrodes were exploited in recordings from European starling birds and zebra finches which possess similar functional organization in their auditory cortex to that of humans (Harris K. , 2015).

To run the experiments for this study initially a 32 channel PtNRs surface array along with a 16 channel depth electrode have been implanted on the HVC brain auditory region of starling

birds and zebra finches under anesthesia. Following, auditory stimuli in the form of bird song (e.g. birds' native song) has been played for the birds (Figure 3-2). Figure3-2a-b demonstrate schematics of the songbird brain circuit and location of PtNR array implanted on top of the HVC. Figure 3-3a-b display 2s of spectrogram of the zebra finch song on top and on the bottom eight high-passed filtered data sets. Four of the sets are recorded from surface electrodes in red and the other four are recorded from depth electrodes in blue.

Subsequently, multi-unit and single cells are extracted from this high frequency data. Figure 3-2c & Figure 3-5a-b demonstrate a few of the single cell waveforms from the surface array in red and depth electrode in blue, recorded from a starling bird and a zebra finch respectively. To differentiate between single cells and multi-units, inter-spike intervals (ISI) have been calculated for all the recorded cells (Figure 3-2c second row and Figure 3-5a-b, right side). Cells with ISI more than 1-2ms have been categorized as single cells.

Stimulus driven neural response analysis is another method that assist us to segregate real neuron cells from noise (Figure 3-2d-e). These figures display an example of a cell with stimulus driven neural response. On top 28 seconds of starling bird song spectrogram is shown. Underneath, respectively, recorded raw signal is shown in blue while the same signal high pass filtered (>300 Hz) is displayed in green, the trial average of 30 trial spike trains is illustrated by the red curve, and finally the spikes raster plot of 30 trials is displayed in black. This figure, significantly demonstrates stimulus-locked modulation of a single cell to auditory stimuli across 30 trial responses. These cells have been recorded by a surface implanted PtNR array.

The magnified view of 5s of Figure 3-2d has been demonstrated in Figure 3-2e. The log of power spectrum density (PSD) averaged over 65 frequency bands of bird song spectrogram is shown in black on the spectrogram. In the second row, the average of 65 frequency bands of the

spectrograms' PSD is calculated. The third row displays the average of 30 trial responses in red. The fourth row is a raster plot of 30 trial responses. Comparing the second, third, and forth row curves shows this cell is not only stimulus-locked, but also its average of trials has delayed correlation with stimuli power modulations.

Stimulus-locked character of this cell has encouraged us to examine the possibility of extracting composite receptive fields (CRFs) from it (see chapter 2-3 for method). Figure 3-6 shows the 10 most significant facilitatory receptive fields and 10 most significant excitatory receptive fields extracted from this cell. As it is observed, the receptive field images are high quality with minimum noise. See section 2-4-5 for more information about CRFs quality.

Another valuable piece of information one can obtain from our recordings is local field potentials (LFP). The LPF signals from surface array channels and depth array channels are extracted by filtering recorded data less than 300 Hz. Correlation between LFP signals of 30 channels of a surface PtNR array has been tested first (Figure 3-4). The result demonstrates, in general, there is high correlation between sites on the surface (r >86%). Subsequently, the correlation between LFP signals of 30 surface sites were compared with LFP signals from 10 depth sites (Figure 3-5c). The result showed there are high correlation in-between surface LFPs (r=0.8-1) as well as high correlation in-between depth LFPs (r=0.8-1) but lower correlation exist among surface and depth LFPs (r=0.55-0.75). The correlation drops by traveling from cortical surface into deep auditory cortex. The correlation coefficients (r) from the HVC surface of the brain to 2500 µm deep changes from almost 100% to 55%.

Figure 3-2: Recording of stimulus modulated single unit activity with PtNRs in Starling songbird experiments.
a) Auditory stimuli in the form of bird song (e.g. bird own song) is played for European Starling bird under anesthesia and neural signals are recorded from HVC auditory area. **b)** Schematic of the songbird brain circuit and location of PtNR array implanted on top of the HVC. **c)** Example of single unit surface spike waveforms (Top) and their corresponding Inter-spike interval (ISI) histograms of waveforms (bottom). The red waveforms are averages of 20 uniformly sampled spike snippets. The black scales on lower right of each waveforms indicates 50 μV amplitude. **d)** Cell with stimulus driven neural response. The first row demonstrates spectrogram of 28s stimulus (bird's own song). The color from blue to yellow indicate intensity of stimulus power from low to high. The second row displays a recorded raw signal (blue). The third row demonstrates same signal high pass filtered (>300 Hz) (green). The fourth row shows the trial average of 30 trial spike trains. Bottom row is a spike raster plot of 30 trials. **e)** Magnified view, 5s of stimuli: First row shows spectrogram of 5s bird own song. The log of power spectrum density (PSD) averaged over 65 frequency bands is overlaid in black. Second row is the average of 65 frequency bands of PSD. Third row displays the trial average in red. Last row shows raster plot of 5s spike train in response to 30 trials showing modulated spiking across trials.

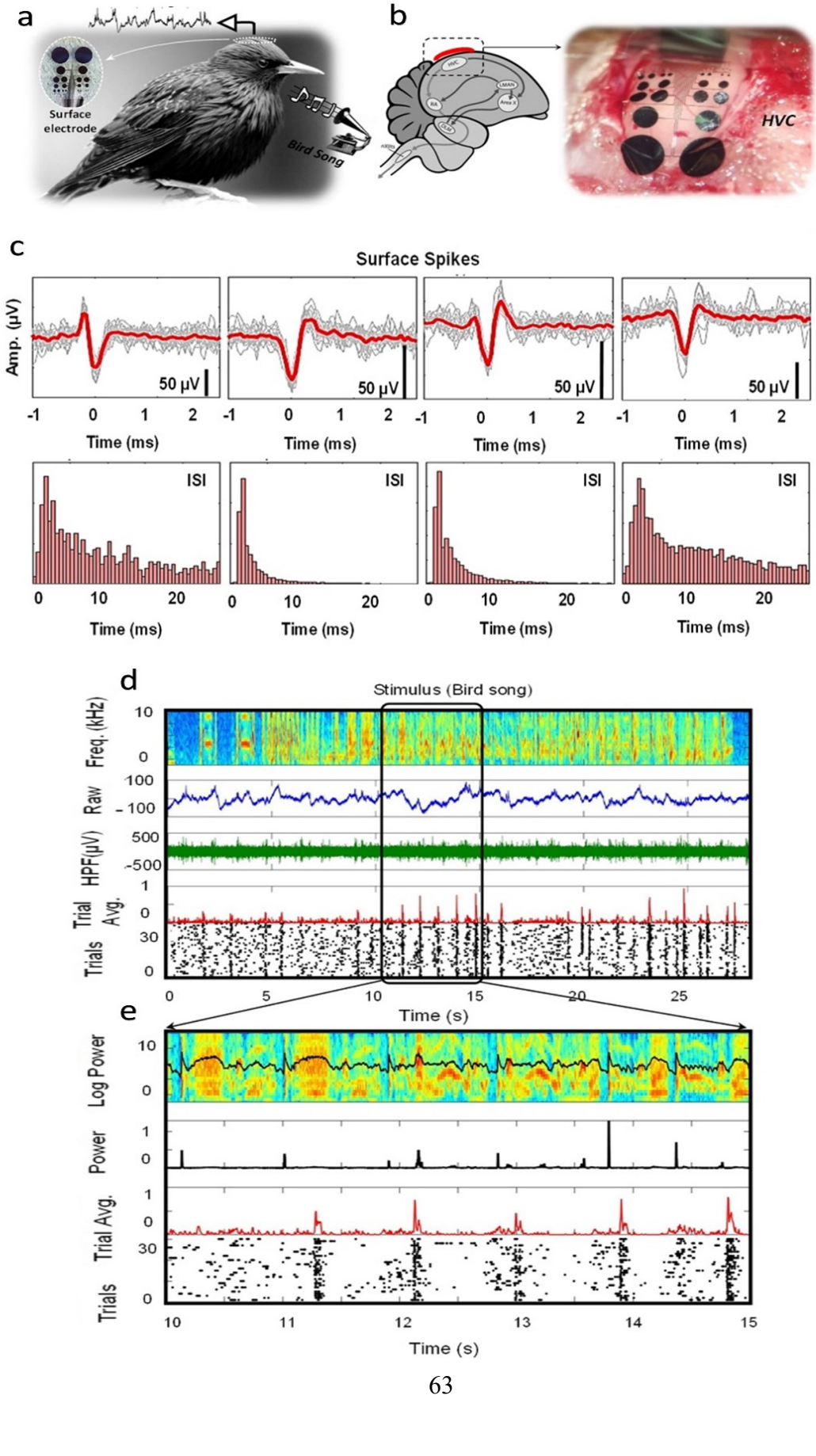
a
Surface electrode
Bird Song
b
HVC
c
Surface Spikes
Amp. (μV)
50 μV
Time (ms)
ISI
d
Stimulus (Bird song)
Freq. (kHz)
Raw
HPF(μV)
Trial Avg.
Trials
Time (s)
e
Log Power
Power
Trial Avg.
Trials
Time (s)

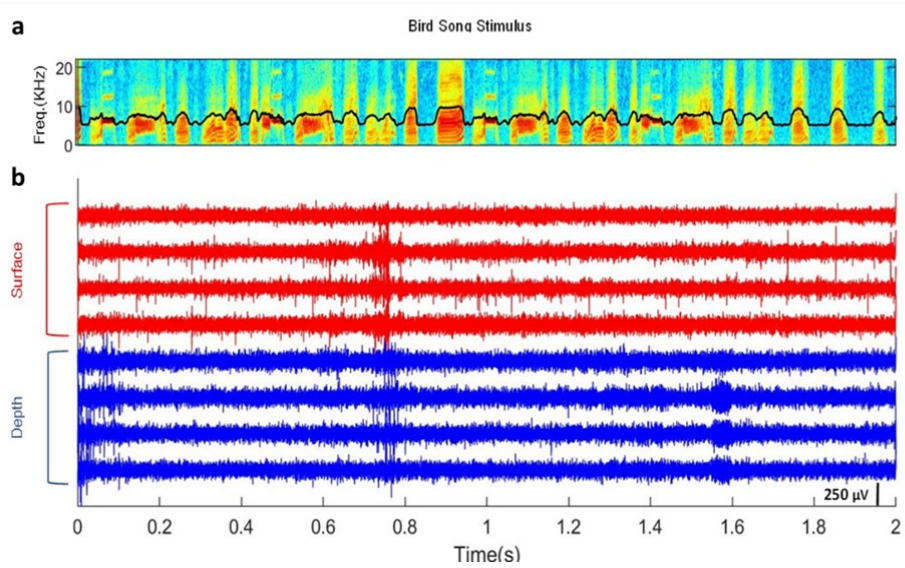

Figure 3-3: Example of high passed data for surface and depth electrode.
a) Spectrogram of the stimulus of a zebra finch song. The black waveform is the log of power spectrum density (PSD) averaged over 65 frequency bands of spectrogram. b) Eight high-pass filtered time series: Four recorded from surface electrodes in red and the other four are recorded from depth electrodes in blue. The black scale bar in bottom right indicates amplitude of 250µV.

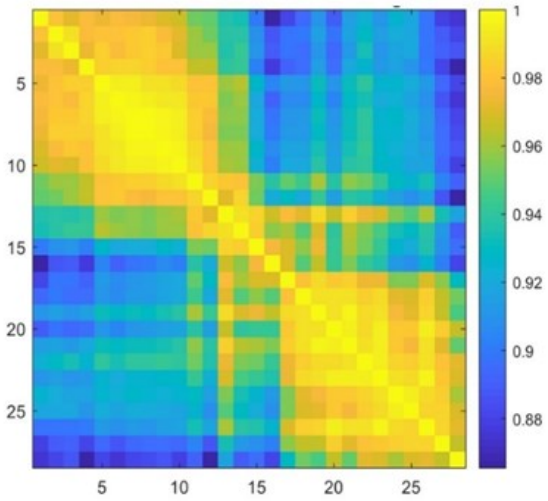

Figure 3-4: Similarity map across LFP data of 30 surface electrodes
30 channels of data first low pass filtered at 300 freq. to extract local field potential (LFP) waveforms then the correlation coefficient across the 30 channels LFP are calculated based on cross-correlation method. The color bar in right side indicates the most similarity between channels (r=1) in bright yellow and less similarity in dark blue (r=0.8). This map shows similarity between LFP data of surface channels are high and ranging from r=0.86 to 1.

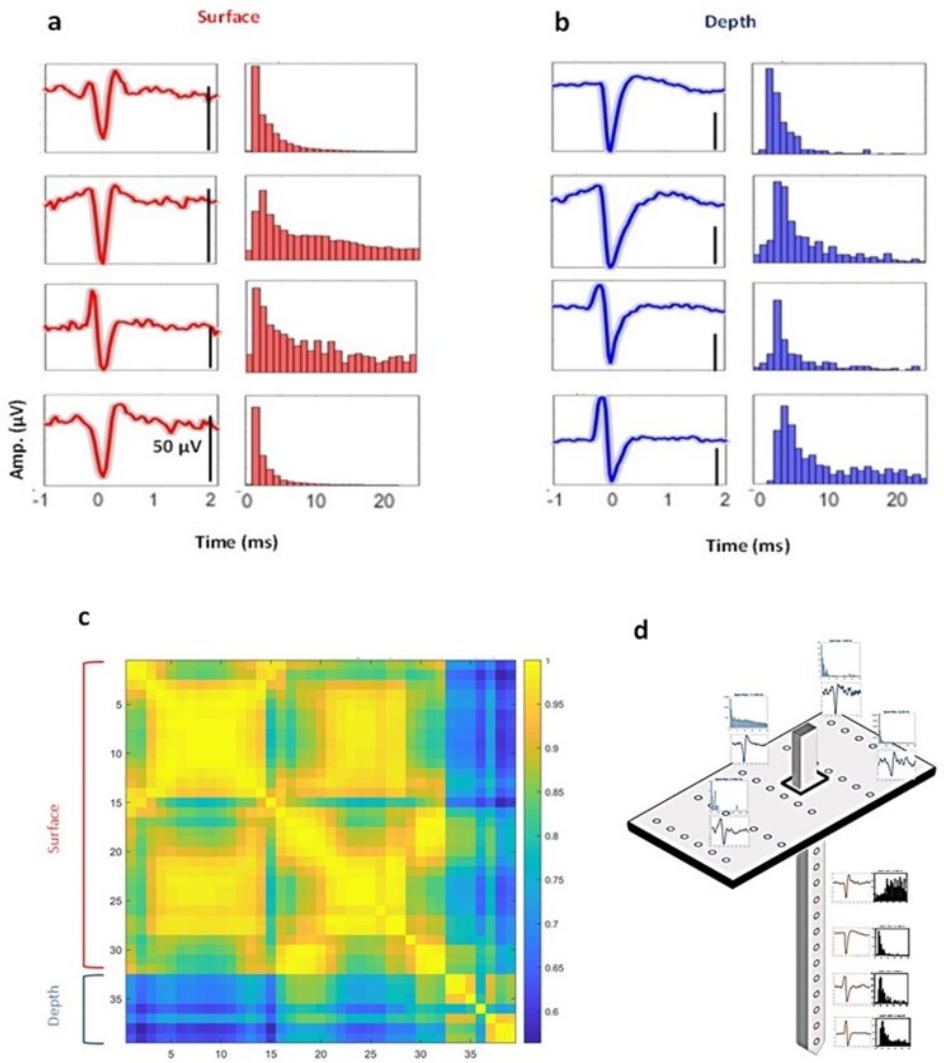

Figure 3-5: Examples of recorded single cell spike waveforms from surface and depth electrodes.

a) Single cells recorded spike waveforms from surface electrode. The red waveforms are averages of 20 sampled spike snippets and the scale black bar indicates 50μV in amplitude. Left column are waveforms corresponding inter-spike interval (ISI) histograms in red. b) Single cells recorded spike waveforms from depth electrode. The blue waveforms are averages of 20 sampled spike snippets. Left column demonstrates the waveforms corresponding inter-spike interval (ISI) histograms. c) Similarity map across 40 channels of LFP data from 32 surface electrodes and 8 depth electrodes. The 40 channels data first low pass filtered at 300 Hz to extract local field potential (LFP) waveforms then the correlation coefficient across the 40 channels LFP are calculated based on cross-correlation method. The color bar in right side indicates the most similarity between channels in bright yellow and less similarity in dark blue. This correlation matrix demonstrates high correlation in-between surface LFPs (r=0.8-1) as well as high correlation in-between depth LFPs (r=0.8-1) but lower correlation among surface and depth LFPs (r=0.55-0.75). d) An illustrations demonstrating example of spike waveforms recorded from the surface and depth electrodes.

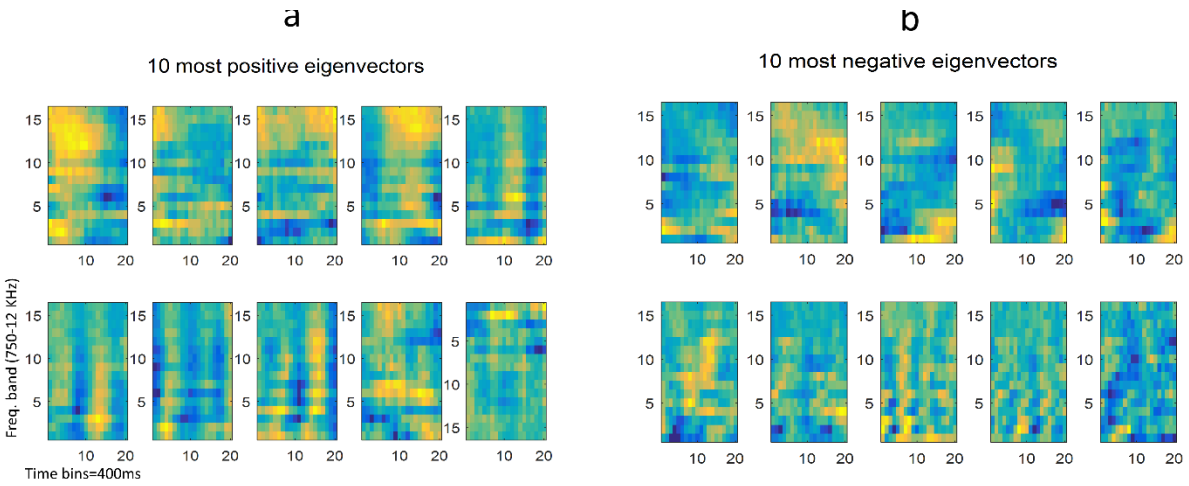

Figure 3-6: Examples of extracted CRFs from a single cell.
a) 10 most significant facilitatory receptive fields of a single cell. b) 10 most significant excitatory receptive fields. This show cells recorded with PtNR are of high quality which enable us to extract low noise receptive fields from them.

3.5 Conclusion

Here in this study we have introduced a highly flexible ECoG array with novel electrochemical sensing sites. The PtNR malleable substrate is made of a thin parylene C and the embedded microelectrodes are constructed by Pt nanorods. PtNRs array is a promising neural interface that can surpass other ECOG micro and nanoelectrodes by incorporation of nanoporous structures (Erlebacher, 2001) to the electrode sites. There are studies that have been done to create nanostructures in general and Pt nanostructures in particular however, their results were not applicable for ECOG prosthetics. The existing nanostructures are mostly require high temperatures which made them incompatible with flexible substrates, they have weak physical strength, and contain toxic ligand additives ((Wagner, 1964) & (Sun, 2018)).

PtNR sites made of nonporous structures, as opposed to existing nanostructures, are developed by selective chemical dissolution of metal alloys technique (Erlebacher, 2001). The PtNR sites are porous, uniformly distributed, biocompatible. In addition, they have very low impedances and high charge injection capacities.

To inspect thin PtNR microelectrode array ability for neural recording from cortical surface, the array was implanted on HVC auditory area of song birds along with a commercial depth electrode shank as a control. Statistical analysis on the neural data recorded by PtNR surface array demonstrate that the array is able to record action potential from single cells similar to the control depth electrode. The recorded cells were stimulus-locked with low noise which promote extrication of composite receptive fields for these cells. Furthermore, analyzing local field potential signals recorded from both surface array and depth electrode have shown there are high correlation in-between surface LFPs as well as high correlation in-between depth LFPs but lower correlation exist among surface and depth LFPs.

This study demonstrates that PtNRs in general are biocompatible and robust and therefore can be used as a unique microelectrode coating on chronic implants. Thin PtNRs microelectrode arrays implanted on the cortical surface have shown that they are capable of recording high quality neural data from the surface of brain such as LFP, single cells, multi-units, and composite receptive fields. In general, PtNRs arrays performance suggest their potential for minimally invasive neuro-prosthetic applications. Likewise, they can be introduced as novel intermediate tools to assist study of neural activities, receptive fields, and their relationship to presented stimuli on the surface of brains.

3.6 **Acknowledgements**

Chapter 3, in full, is in preparation for publication as: Mehran Ganji, Angelique C. Paulk, Jimmy C. Yang, Nasim W. Vahidi, Sang Heon Lee, Ren Liu, Lorraine Hossain, Ezequiel M. Arneodo, Martin Thunemann, Michiko Shigyo, Atsunori Tanaka, Sang Baek Ryu, Seung Woo Lee, Martin Marsala, Anna Devor, Daniel Cleary, Vikash Gilja, Timothy Q. Gentner, Shelly I.

Fried, Eric Halgren, Sydney S. Cash, and Shadi A. Dayeh. “Selective Formation of Porous Pt Nanorods for Highly Electrochemically Efficient Neural Electrode Interfaces”. The dissertation author was the co-primary investigator of this chapter.

3.7 References

Amaral, J., Pinto, V., Costa, T., Gaspar, J. M., Ferreira, R., Paz, E. M., Freitas, P. P. (2013). Integration of TMR Sensors in Silicon Microneedles for Magnetic Measurements of Neurons. *Undefined*. Retrieved from https://www.semanticscholar.org/paper/Integration-of-TMR-Sensors-in-Silicon-Microneedles-Amaral-Pinto/2b24a177d48259e0a4ae7bc2760c31fd2d3e0540

Banerjee, D., Jo, S. H., & Ren, Z. F. (2004). Enhanced Field Emission of ZnO Nanowires. *Advanced Materials*, *16*(22), 2028–2032. https://doi.org/10.1002/adma.200400629

Black, C., Voigts, J., Agrawal, U., Ladow, M., Santoyo, J., Moore, C., & Jones, S. (2017). Open Ephys electroencephalography (Open Ephys + EEG): a modular, low-cost, open-source solution to human neural recording. *Journal of Neural Engineering*, *14*(3), 035002. https://doi.org/10.1088/1741-2552/aa651f

Brainard, M. S., & Doupe, A. J. (2002). What songbirds teach us about learning. *Nature*, *417*(6886), 351–358. https://doi.org/10.1038/417351a

Chen, C.-H., Chuang, S.-C., Lee, Y.-T., Chang, Y.-C., Yeh, S.-R., & Yao, D.-J. (2010). Three-dimensional flexible microprobe for recording the neural signal. *Journal of Micro/Nanolithography, MEMS, and MOEMS*, *9*(3), 031007. https://doi.org/10.1117/1.3455409

Dai, X., Zhou, W., Gao, T., Liu, J., & Lieber, C. M. (2016). Three-dimensional mapping and regulation of action potential propagation in nanoelectronics-innervated tissues. *Nature Nanotechnology*, *11*(9), 776–782. https://doi.org/10.1038/nnano.2016.96

Dayan, P., & Abbott, L. F. (2001). *Theoretical neuroscience : computational and mathematical modeling of neural systems*. Massachusetts Institute of Technology Press.

Fu, T.-M., Hong, G., Viveros, R. D., Zhou, T., & Lieber, C. M. (2017). Highly scalable multichannel mesh electronics for stable chronic brain electrophysiology. *Proceedings of the National Academy of Sciences of the United States of America*, *114*(47), E10046–E10055. https://doi.org/10.1073/pnas.1717695114

Greene, L. E. (2006). Solution-grown zinc oxide nanowires. *Inorganic chemistry 45*, 7535-7543 .

Ganji, M., Kaestner, E., Hermiz, J., Rogers, N., Tanaka, A., Cleary, D., … Dayeh, S. A. (2018). Development and Translation of PEDOT:PSS Microelectrodes for Intraoperative Monitoring. *Advanced Functional Materials*, *28*(12), 1700232.

Harris, K. D., & Woolley, S. (2015). Cortical computation in mammals and birds. *Proceedings of the National Academy of Sciences of the United States of America*, *112*(11), 3184–3185. https://doi.org/10.1073/pnas.1502209112

Hong, G., Fu, T.-M., Qiao, M., Viveros, R. D., Yang, X., Zhou, T., … Lieber, C. M. (2018). A method for single-neuron chronic recording from the retina in awake mice. *Science*, *360*(6396), 1447–1451. https://doi.org/10.1126/science.aas9160

Jin, H.-J., Wang, X.-L., Parida, S., Wang, K., Seo, M., & Weissmüller, J. (2010). Nanoporous Au−Pt Alloys As Large Strain Electrochemical Actuators. *Nano Letters*, *10*(1), 187–194. https://doi.org/10.1021/nl903262b

Karten, H. J. (2013). Neocortical Evolution: Neuronal Circuits Arise Independently of Lamination. *Current Biology*, *23*(1), R12–R15. https://doi.org/10.1016/j.cub.2012.11.013

Li, C., Sato, T., & Yamauchi, Y. (2013). Electrochemical Synthesis of One-Dimensional Mesoporous Pt Nanorods Using the Assembly of Surfactant Micelles in Confined Space. *Angewandte Chemie International Edition*, *52*(31), 8050–8053. https://doi.org/10.1002/anie.201303035

Li, H., Misra, A., Baldwin, J. K., & Picraux, S. T. (2009). Synthesis and characterization of nanoporous Pt–Ni alloys. *Applied Physics Letters*, *95*(20), 201902. https://doi.org/10.1063/1.3265744

Liu, L., Pippel, E., Scholz, R., & Gösele, U. (2009). Nanoporous Pt−Co Alloy Nanowires: Fabrication, Characterization, and Electrocatalytic Properties. *Nano Letters*, *9*(12), 4352–4358. https://doi.org/10.1021/nl902619q

Liu, R., Chen, R., Elthakeb, A. T., Lee, S. H., Hinckley, S., Khraiche, M. L., … Dayeh, S. A. (2017). High Density Individually Addressable Nanowire Arrays Record Intracellular Activity from Primary Rodent and Human Stem Cell Derived Neurons. *Nano Letters*, *17*(5), 2757–2764. https://doi.org/10.1021/acs.nanolett.6b04752

Lori E. Greene, Benjamin D. Yuhas, Matt Law, David Zitoun, and, & Yang*, P. (2006). *Solution-Grown Zinc Oxide Nanowires*. https://doi.org/10.1021/IC0601900

Pachitariu, M., Steinmetz, N. A., Kadir, S. N., Carandini, M., & Harris, K. D. (2016). *Fast and accurate spike sorting of high-channel count probes with KiloSort* (pp. 4448–4456). pp. 4448–4456. Retrieved from https://papers.nips.cc/paper/6326-fast-and-accurate-spike-sorting-of-high-channel-count-probes-with-kilosort

Shen, M., Han, A., Wang, X., Ro, Y. G., Kargar, A., Lin, Y., Xiang, B. (2015). Atomic Scale

Analysis of the Enhanced Electro- and Photo-Catalytic Activity in High-Index Faceted Porous NiO Nanowires. *Scientific Reports*, *5*(1), 8557. https://doi.org/10.1038/srep08557

Shui, J.-L., Zhang, J.-W., & Li, J. C. M. (2011). Making Pt-shell Pt30Ni70 nanowires by mild dealloying and heat treatments with little Ni loss. *Journal of Materials Chemistry*, *21*(17), 6225. https://doi.org/10.1039/c1jm10216h

Sun, G., Xu, J., & Harrowell, P. (2018). The mechanism of the ultrafast crystal growth of pure metals from their melts. *Nature Materials*, *17*(10), 881–886. https://doi.org/10.1038/s41563-018-0174-6

Sun, G., Xu, J., & Harrowell, P. (2018). The mechanism of the ultrafast crystal growth of pure metals from their melts. *Nature Materials*, *17*(10), 881–886. https://doi.org/10.1038/s41563-018-0174-6

Tominaka, S., Hayashi, T., Nakamura, Y., & Osaka, T. (2010). Mesoporous PdCo sponge-like nanostructure synthesized by electrodeposition and dealloying for oxygen reduction reaction. *Journal of Materials Chemistry*, *20*(34), 7175. https://doi.org/10.1039/c0jm00973c

Uguz, I., Ganji, M., Hama, A., Tanaka, A., Inal, S., Youssef, A., Malliaras, G. G. (2016). Autoclave Sterilization of PEDOT:PSS Electrophysiology Devices. *Advanced Healthcare Materials*, *5*(24), 3094–3098. https://doi.org/10.1002/adhm.201600870

Wagner, R. S., & Ellis, W. C. (1964). VAPOR-LIQUID-SOLID MECHANISM OF SINGLE CRYSTAL GROWTH. *Applied Physics Letters*, *4*(5), 89–90. https://doi.org/10.1063/1.1753975

Wise, K. D. (2007). Integrated sensors, MEMS, and microsystems: Reflections on a fantastic voyage. *Sensors and Actuators A: Physical*, *136*(1), 39–50. https://doi.org/10.1016/J.SNA.2007.02.013

Yoo, S.-H., & Park, S. (2007). Platinum-Coated, Nanoporous Gold Nanorod Arrays: Synthesis and Characterization. *Advanced Materials*, *19*(12), 1612–1615. https://doi.org/10.1002/adma.200602551

CHAPTER 4

In Vivo dopamine detection and single unit recordings using intra-cortical glassy carbon microelectrode arrays

Published in final edited form as:
MRS Adv. 2018 ; 3(29): 1629–1634. doi:10.1557/adv.2018.98.

In Vivo Dopamine Detection and Single Unit Recordings Using Intracortical Glassy Carbon Microelectrode Arrays

Elisa Castagnola[1,2], **Nasim Winchester Vahidi**[3,4], **Surabhi Nimbalkar**[1,2], **Srihita Rudraraju**[5], **Marvin Thielk**[4], **Elena Zucchini**[6], **Claudia Cea**[1,2], **Stefano Carli**[6], **Timothy Q. Gentner**[4], **Davide Ricci**[5], **Luciano Fadiga**[6,7], and **Sam Kassegne**[1,2]

[1]MEMS Research Lab., Department of Mechanical Engineering, College of Engineering, San Diego State University, 5500 Campanile Drive, San Diego, CA 92182-1323, USA

[2]Center for Sensorimotor Neural Engineering (CSNE), Box 37, 1414 NE 42nd St., Suite 204, Seattle, WA 98105-6271, USA

[3]Dept. of Electrical Engineering, University of California San Diego, La Jolla, CA 92093, USA

[4]Neurosciences Graduate Program, University of California San Diego, 9500 Gilman Dr, La Jolla, CA, USA

[5]Department of Bioengineering, University of California San Diego, La Jolla, CA, USA

[6]Center for Translational Neurophysiology of Speech and Communication, Istituto Italiano di Tecnologia, Via Fossato di Mortara 17/19, 44121, Ferrara, Italy

[7]Human Physiology, University of Ferrara, Via Fossato di Mortara 17/19, 44121, Ferrara, Italy

Abstract

In this study, we present a 4-channel intracortical glassy carbon (GC) microelectrode array on a flexible substrate for the simultaneous in vivo neural activity recording and dopamine (DA) concentration measurement at four different brain locations (220μm vertical spacing). The ability of GC microelectrodes to detect DA was firstly assessed in vitro in phosphate-buffered saline solution and then validated in vivo measuring spontaneous DA concentration in the Striatum of European Starling songbird through fast scan cyclic voltammetry (FSCV). The capability of GC microelectrode arrays and commercial penetrating metal microelectrode arrays to record neural activity from the Caudomedial Neostriatum of European starling songbird was compared. Preliminary results demonstrated the ability of GC microelectrodes in detecting neurotransmitters release and recording neural activity in vivo. GC microelectrodes array may, therefore, offer a new opportunity to understand the intimate relations linking electrophysiological parameters with neurotransmitters release.

INTRODUCTION

Dopamine (DA) is a key neurotransmitter that plays a pivotal role in a large variety of neurophysiological functions. Disruption of the secretion and uptake of this neurotransmitter is the cause of several psychiatric and neurological disorders [1], among which are Schizophrenia [2], Parkinson diseases [3] and drug addiction [4]. To obtain a better understanding of how synaptic malfunctions lead to psychiatric and neurological diseases

and to take the current available clinical treatments to the next level, a fundamental understanding of the interplay between electrical and electrochemical signaling in the basic neurotransmission mechanisms is necessary. For this, the development of a device capable of precisely and selectively detecting neurotransmitters *in vivo* and simultaneously record electrical neural activity is needed. An ideal recording-detection platform has to fulfil many conflicting requirements in order to be able to (i) record informative and robust signals over several years and (ii) selectively and sensitively detect, in a reproducible way, small concentrations of neurotransmitters *in vivo*, at low levels that are typical of living systems. Despite the recent attempt to introduce new electrode materials [5,9] and develop novel microfabrication techniques to allow multi-site detection [10–11], the available techniques for *in vivo* DA detection often lack in stability and spatial selectivity and do not allow the simultaneous detection of electrical and chemical signals.

In this study, we address this problem by introducing a 4-channel glassy carbon (GC) microelectrode arrays on a flexible substrate to measure dopamine concentration *in vivo* and to simultaneously record neural activity at four different locations (220μm vertical spacing). We present preliminary *in vivo* validation of (i) the capability of GC microelectrodes to detect spontaneous DA concentration in the Striatum of a European starling songbird through fast scan cyclic voltammetry (FSCV), (ii) the capability to simultaneously record single-unit neural activity at four different depth locations from the Caudomedial Neostriatum (NCM) auditory area of a European starling songbird, compared with commercial penetrating metal microelectrode array.

EXPERIMENTAL DETAILS

Glassy Carbon Microarrav Fabrication

The fabrication of the thin-film devices used for this study is described in detail elsewhere [12,13], Here, we extend the microfabrication technology by adding a new reinforcing layer to allow brain penetration. An additional thicker layer of polyimide (Durimide 7520) (FujiFilm) was then patterned on top of the insulation layer to reinforce the penetrating portion of the device. Subsequently, the device was released from the wafer through the selective etching of the silicon dioxide with buffered hydrofluoric acid. The microelectrode array is made of 4 recording-detection sites with an area of 1500 μm^2 and a vertical inter-electrode distance of 220 μm.

Surgery, Neural Recording and Data Acquisition

Starling bird was anesthetized under isofluorane, and urethane and a craniotomy was made around Y-sinus with enough space for electrode implantation. Then the probe was attached to the head-stage and lowered down to 2000 μm by stereotaxic coordinates targeting Caudomedial Neostriatum NCM (Right hemisphere, posterior: 750 μm, lateral: 1600 μm from the bifurcation of the sagittal sinus). Finally, the reference/ground electrode was inserted under the skull opening.

After dropping the microelectrode implants to the desire area, a series of natural Starling bird songs were played in a random order to the anesthetized bird. The recordings were

performed by utilizing A-M recording systems (Sequim, WA) for 30 min. The neural recording was obtained from NCM auditory area of brain of a European Starling songbird. Brain response recording was started with sampling rate of 20 kHz from four electrode sites on both microelectrodes. The signals were filtered (300Hz – 5kHz) with gain of 5K. The recorded signals then were sent to a A/D converter (CED Power 1401) with 10X gain to be digitized. Recordings were performed both using our device and a commercial depth electrode as a reference (Neuronexus, A16-5mm-50-177, 15 μm diameter Ir-based microelectrodes).

In-vitro and *In-vivo* Electrochemical Detection

Fast-Scan Cyclic Voltammetry (FSCV) was carried out for dopamine detection using WaveNeuro FSCV Potentiostat System (Pine Research, NC). For *in vitro* DA calibration in phosphate-buffered saline solution (PBS; 0.1 M, pH 7.4) (Sigma Aldrich, USA), a waveform proceeding with a triangle scan at 400 V/s from −0.5 V to +1.3 V and back to −0.5V with respect to the reference Ag/AgCl electrode was used. The duration of each scan was 9 ms (900 data points) with a frequency of 10 Hz. The same voltage waveform was applied to microelectrodes at 60 Hz for 1 hour prior to the start of each experiment, to precondition the microelectrodes. Known concentrations of dopamine (10 nM – 400 nM) were then injected for 5 s and changes in current recorded for 40 seconds. The background current caused by the charging of the double layer was digitally subtracted, revealing the oxidation peak of DA. The *in vivo* detection of basal level of DA was obtained from the medial striatum (MSt) of European starling songbird without applying electrical stimulation.

RESULTS

Neural Recordings

We use songbirds as recoding model because their auditory area is similar to Superior Gyro area of the human brain which deals with speech and acoustic, making it a good candidate for neural recording [14]. Preliminary recording from GC microelectrode arrays has shown that the GC microelectrode array is capable of simultaneously record high quality single-unit neural activity at four different depth locations (220μm vertical spacing). The neural activity recorded using GC microelectrode array and commercial penetrating metal microelectrode array (Neuronexus, A16-5mm-50-177) were compared. Examples of bird song wave and recording activity for a GC microelectrode (top) versus a commercial microelectrode (bottom) are reported in Figure 1a and b. In both the cases, the stimulated neural activity is synchronized with the bird song wave. GC microelectrodes have shown to record greater spikes and lower base line activity compared with the commercial microelectrode. This means GC microelectrodes can pick up neural activity with a higher signal to noise ratio than the utilized commercial microelectrode.

FSCV Dopamine Detection

The GC penetrating microelectrodes are able to detect very clear DA peaks in a range of concentration from 10 nM, the lower detection limit, to 400 nM in PBS. Figure 2 shows an example of DA signal detected using a standard pyramidal FSCV waveform in which the applied voltage was ramped from −0.5 V to+1.3 V and then back to −0.5 V at 400 V/s scan

rate and 10Hz frequency. In particular, the color plot (Fig. 2a) shows the changes in current following 10nM DA injection in PBS in vitro. The changes in currents correspond to the reduction (−0.17V) and oxidation (0.63 V) peaks of DA, as visible from the correspondent background subtracted CV plot (Fig. 2b). The *in vitro* DA calibration curve is reported in Figure 2c. The microelectrode sensitivity to DA, defined as the normalized oxidation peak amplitude at the different DA concentrations, follows a logarithmic trend in the 10–50 nM concentration range and a linear trend (Pearson's r = 0.997) in the 50–400 nM concentration range. The functionality of the array was *in vivo* validated by measuring the spontaneous DA concentration in the MSt of an anesthetized European starling songbird, through FSCV. Figure 3 shows an example of the spontaneous DA signal detected; the oxidation peak amplitude corresponds to a 10nM concentration of the *in vitro* calibration results. The color plot (Fig. 3a) shows the changes in current due to a spontaneous DA release. The changes in currents correspond to the reduction (−0.17 V) and oxidation (+0.63 V) peaks of DA, as visible from the correspondent background subtracted CV plot (Fig. 3b).

CONCLUSIONS

In this study, we presented a 4-channel glassy carbon (GC) penetrating microelectrode array on a flexible substrate, able to (i) record high quality single-unit neural activity at four different depth locations (220μm vertical spacing) from NCM auditory area of brain of a European Starling songbird; (ii) *in vitro* measure 10 nM lower limit detection of DA through FSCV; (iii) *in vivo* detect DA spontaneous concentration in the MSt of an anesthetized starling songbird through the use of FSCV. To the best of our knowledge, this work represents the first report in the literature on the use of GC microelectrode array for *in vivo* DA detection in a songbird. These preliminary results show promising opportunity that GC microelectrode arrays may offer for real-time and simultaneous *in vivo* neural recording and neurotransmitter detection. Depending on the physiological and clinical goals, some of the microelectrodes of the probe could be used for electrical recordings while others could simultaneously be used for DA detection, helping in the understanding of the intimate relations linking electrophysiological parameters with neurotransmitters release.

Acknowledgments

This material is based on research work supported by the Center for Sensorimotor Neural Engineering (CSNE), a National Science Foundation Engineering Research Center (EEC-1028725). We would like to thanks Bradley Theilman at UCSD Centner lab.

References

1. van Spronsen M, Hoogenraad CC. Curr Neurol Neurosci Rep. 2010; 10(3):207. [PubMed: 20425036]
2. Brisch R, Saniotis A, Wolf R, Bielau H, Bernstein HG, Steiner J, Bogerts B, Braun K, Jankowski Z, Kumaratilake J, Henneberg M, Gos T. Front Psychiatry. 2014; 5:47. [PubMed: 24904434]
3. Lotharius J, Brundin P. Nature Reviews Neuroscience. 2002; 3(12):932. [PubMed: 12461550]
4. Volkow ND, Fowler JS, Wang GJ. Behav Pharmacol. 2002; 13(5–6):355. [PubMed: 12394411]
5. Castagnola E, Carli S, Vomero M, Scarpellini A, Prato M, Goshi N, Fadiga L, Kassegne S, Ricci D. Biointerphases. 2017; 12(3):031002. [PubMed: 28704999]
6. Mundroff ML, Wightman MR. Curr Protoc Neurosci Chapter. 2002; 6 Unit 6.14.
7. Cahill PS, Walker QD, Finnegan JM, Mickelson GE, Travis ER, Wightman MR. Anal Chem. 1996; 68:3180. [PubMed: 8797378]
8. Taylor IM, Robbins EM, Catt KA, Cody PA, Happe CL, Cui XT. Biosens Bioelectron. 2017; 89(Pt 1):400. [PubMed: 27268013]
9. Xiao N, Venton BJ. Anal Chem. 2012; 84(18):7816. [PubMed: 22823497]
10. Yi W, Yang Y, Hashemi P, Ming-Cheng Cheng M. Biomed Microdevices. 2016; 18:112. [PubMed: 27900618]
11. Zachek MK, Takmakov P, Moody B, Wightman RM, McCarty GS. Anal Chem. 2009; 81(15): 6258. [PubMed: 19552423]
12. Vomero M, Castagnola E, Ciarpella F, Maggiolini E, Goshi N, Zucchini E, Carli S, Fadiga L, Kassegne S, Ricci D. Scientific Reports. 2016; 7:40332.
13. Vomero M, van Niekerk P, Nguyen V, Gong N, Hirabayashi M, Cinopri A, Logan K, Moghadasi A, Varma P, Kassegne S. J Micromechanic Microengineer. 2016; 26:2.
14. Simonyan K, Horwitz B, Jarvis ED. Brain Lang. 2012; 122(3):142. [PubMed: 22284300]

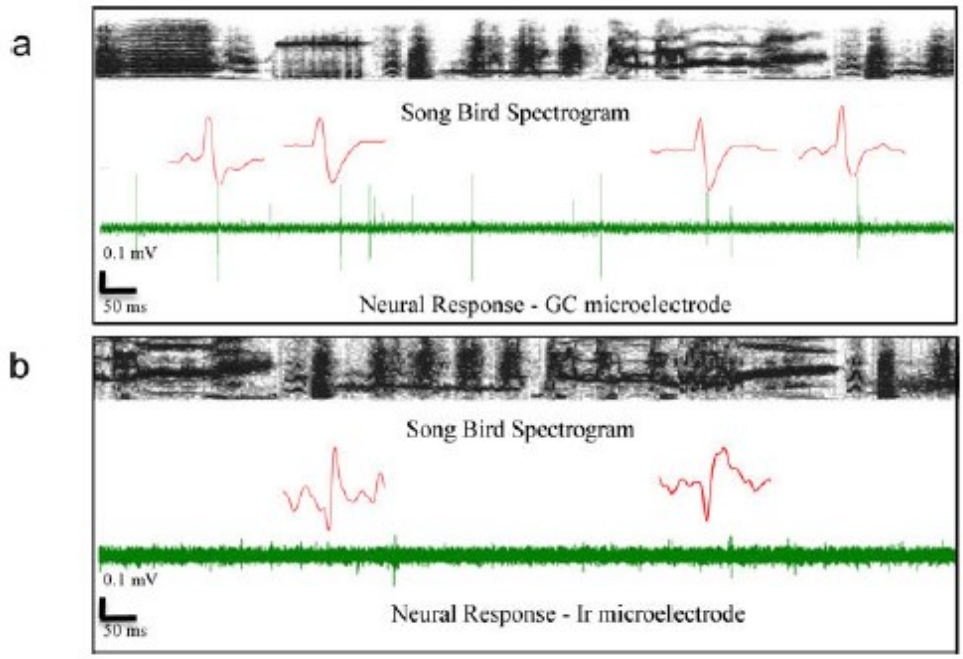

Figure 1.
Neural recording: comparative example of bird song wave and recording activity with a GC microelectrode (a) versus a commercial Ir microelectrode (b) Magnifications of single unit activities for both (a) and (b) are reported in insets.

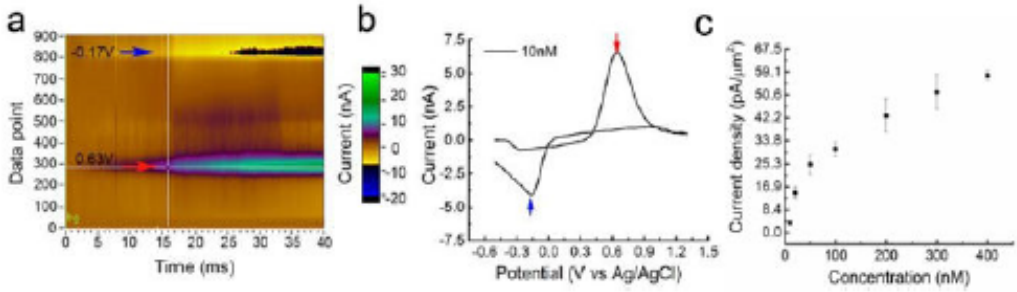

Figure 2.
example of 10 nM concentration dopamine signals detected using a standard pyramidal FSCV waveform in which the applied voltage was ramped from the holding potential of −0.5 V to the switching potential of+1.3 V and then back to −0.5 V at 400 V/s scan rate: color plot (a) and subtracted FSCV plot (b). (c) *In vitro* calibration curve in PBS solution.

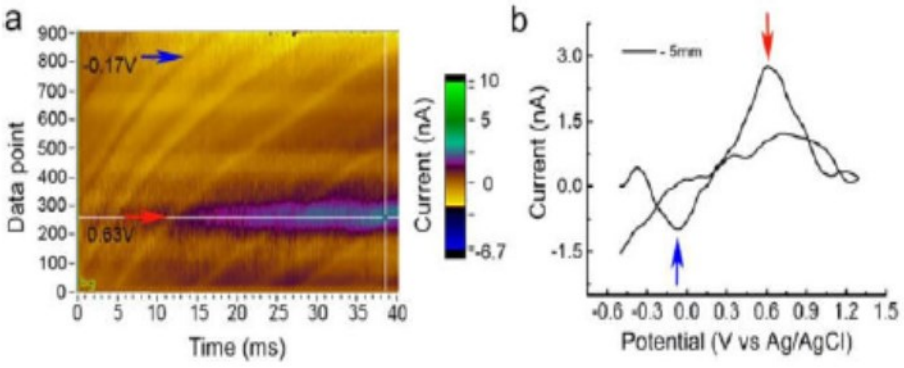

Figure 3.
example of spontaneous DA signal detected from the MSt of an anesthetized Starling songbird though the use of a standard pyramidal FSCV waveform in which the applied voltage was ramped from the holding potential of −0.5 V to the switching potential of +1.3 V and then back to −0.5 V at 400 V/s scan rate: color plot (a) and subtracted FSCV plot (b).

4.7 Acknowledgements

Chapter 4, in full, is a reprint of materials as it appears in Elisa Castagnola, Nasim W.Vahidi, Surabhi Nimbalkar, Srihita Rudraraju, Marvin Thielk, Elena Zucchini, Claudia Cea, Stefano Carli, Timothy Q. Gentner, Davide Ricci, Luciano Fadiga, and Sam Kassegne (2018). "In Vivo Dopamine Detection and Single Unit Recordings Using Intracortical Glassy Carbon Microelectrode Array" *in MRS Adv.3,* p. 1629–1634, doi:10.1557/adv.2018.98. The dissertation author was the primary co- author of this paper.

CHAPTER 5

Epi-Intra device with glossy carbon electrodes: A tool for neural coding

5.1 Abstract

In this study we demonstrate practical applications of an in-house fabricated novel device for simultaneous recording from brain cortical surface as well as deep tissue. This device is an origami combination of epi-cortical surface array and intra-cortical depth shank (Epi-intra) which will unfold during brain implant. The surface array is flexible and will confirm to the brain cortex while the depth shank is reinforced for an easy penetration. The electrode sites are made of glassy carbon (GC). The GC electrodes are inert, biocompatible, low impedance, with excellent electrochemistry sensing properties. Here we have demonstrated simultaneous electrical recording from electrode sites on the surface array as well as the depth shank. The recordings have been performed on the auditory region of anesthetized European starling songbirds during playback of starling bird songs as auditory stimuli. The Epi-Intra device has demonstrated ability to record local field potential (LFP) signals as well as single cells and multi-units from both surface and deep brain. Most of the recorded cells are stimulus-locked with low noise. Electrical recordings from this 3D Epi-Intra configuration can be used to investigate relationships between brain responses and stimuli from deep brain to the surface or vice versa. To investigate this relationship, we first explored correlation between LFP data. The result has shown that traditional LFP signals' correlation does not hold when neurons are far from each other e.g. neurons from surface and deep brain. To overcome this limitation here we adopted a non-linear model to extract composite receptive fields (CRFs) from individual neuron cells, after which these CRFs can be utilized to investigate brain response and stimuli relationship due to the fact that CRFs of neuron cells, unlike LFPs' correlation, are independent of cell location. This fact made CRFs extracted from cells recorded by Epi-Intra combinations very good candidates for understanding the relationship between sensory neuron responses and their stimuli from deep brain to cortical surface in 3D

volumes of tissue. In addition, these CRFs located in the 3D volume can be used as tools for neural decoding and encoding of stimulus.

5.2 Introduction

Here we are explore the excellent electrical recording data of an Epi-Intra device that conceivably make this device a potential tool for neural coding from deep brain to cortical surface. The Epi-Intra device has a 3D origami shape consisting of an epi-cortical surface array and intra-cortical depth shank and designed for neural recording from a volume of a brain tissue.

The depth shank consists four GC recording sites and has been reinforced during fabrication for easy brain penetration. On the other hand, the surface array of the Epi-Intra device contains seven GC recording sites and a reference on a flexible polymer substrate. These sites are positioned on both side of depth shank to insure neural recording from a volume of tissue (Figure 5-3).

The core extended C-MEMS microfabrication technology that is used for these GC thin-film devices supported on polymeric substrates is described in detail elsewhere ((Nimbalkar, 2018) and (Vomero, 2016)). In summary, the glassy carbon electrodes were fabricated using negative photoresist SU-8, which was patterned and pyrolyzed at 1000 °C in an inert atmosphere. Subsequently, a layer of photosensitive polyimide (HD Microsystem) was spun and patterned onto the electrodes, as a substrate for the subsequent layers. Metals (Cr and Au) were then deposited on the substrate to create the conductive traces, and finally a second layer of polyimide was spun on the traces to electrically insulate them. Here, we further extend the functionality of this microfabrication technology by incorporating an additional procedure for depositing a reinforcing polymer layer that will allow easy penetration of the depth shank into brain tissue.

The Epi-Intra device has been characterized by different methods. The optical microscope and scanning electron microscope (SEM) images on GC microelectrodes indicate uniform distribution of glassy carbon before and after implantation (Figure 5-3B) (Vomero, et al., 2017). The capacitive charging ability and electrochemical characterization of GC microelectrodes were evaluated by cyclic voltammetry (CV), voltage transient (VTs), and electrochemical impedance spectroscopy (EIS). The GC penetrating microelectrodes show clear ability to detect neurotransmitters such as dopamine (Castagnola, et al., 2018). In addition, GC microelectrodes exhibit low impedance which make them suitable candidates for neural recordings (Goshi, et al., 2018). Furthermore, biocompatibility and the mechanical stability of GC electrode sites was monitored by implanting the Epi-Intra device into cultured fibroblasts cells. The results demonstrated this device has a potential for chronic implants and recordings (Vomero, et al., 2017) .

To explore the electrical recording ability of Epi-Intra electrodes, the device was implanted on the auditory region of anesthetized European starling bird brains. The auditory region of avian brains process audio stimuli the same way as humans ((Karten, 2013) & (Harris , 2015)). During implantation the Epi-Intra origami configuration the electrode converts to two connected parts of surface array and depth shank. The Epi surface array conforms to the curvature of the cortex while the Intra depth shank penetrates deep into the brain (Figure 5-3a). Brain signals were recorded while audio stimuli, bird songs, were played back for the subjects (Figure 5-2). The recorded data from eleven channels were later filtered via low pass (<300Hz) and high pass (300-20KZ) filters to determine LFPs and neuron cell action potentials. Figure 5-4 displays high pass data collected from channels on the surface as well as deep brain. From these electrical recordings we were able to extract robust LFP signals as well as discern single cells and multi-units from both cortical

surface and deep brain. The recorded cells are high quality stimulus-locked (Blackwell, 2015) with low noise (Figure 5-5a-b). To differentiate between single cells and multi-units, inter-spike intervals have been calculated (Figure 5-5c) (Dayan & Abbott, 2000).

The 3D Epi-Intra configuration proposed in this study can be used to investigate relationship between stimulus and its brain responses from deep in the brain up to the cortical surface or vice versa. To investigate this relationship, first we explored correlation between LFP signals of eleven channels on the surface array and depth shank. The result demonstrated the LFP correlations in-between channels decrease from surface to depth for channels further than 1500 μm (Figure 5-6). This result is consistent with some other new studies ((Destexhe, 1999) & (Bedard, 2004)). In consequence, to avoid the cells' distance limitation, instead of LFPs we concentrated on cell action potentials and their receptive fields (Figure 5-7).

Recently we have demonstrated that the brain perceives cells' composite receptive fields (CRFs) independent of cell locations and their topology (Vahidi, 2018). Thus concentrating on CRFs appear to be a better option than LFPs to investigate stimulus and neural response relationship for cells that have long distances for instance deep brain cells relative to surface cells. To generate CRFs, Maximum noise entropy model (MNE) has been adopted. The MNE minimal model describes the probability of brain responses given a stimulus such as bird song. This model looks for highest mutual information between stimuli and the brain response in the form of composite receptive fields at the cellular level ((Fitzgerald , 2011a) & (Kozlov & Gentner, 2016)).

There are prevailing models which can create receptive fields from neuron cells such as spike trigger average which it widely has been used to build linear receptive fields (De Boer & Kuyper, 1968), spike-triggered covariance (Schwartz., 2002), and maximally informative dimensions (MID) (Sharpee, 2004). Although these models have provided excessive information

about receptive fields, they exhibit limitations such as inability to characterize nonlinear information of stimuli (Thunissen, 2000), limitation working with natural stimuli such as human speech or bird song ((Schwartz , 2006)& (Eggermont, 1983b)), and limitations identifying large numbers of relevant receptive field features with respect to natural stimuli. In contrast, the MNE model utilized in this study overcomes most of these drawbacks ((Kozlov & Gentner, 2016), (Fitzgerald, 2011a), (Sharpee, 2004) , and (Bialek W. D., 2006)).

The high quality stimulus-locked cells recorded by the Epi-Intra device have opened the opportunity to extract CRFs from them. Figure 5-7a shows examples of ten facilitatory and ten suppressive receptive fields generated from one single cell on the cortical surface. Figure 5-7b displays Epi-Intra combination electrodes with the example of single cell waveforms from their corresponding recording sites on the surface array and depth electrode. Next to each waveform, the first extracted receptive field from 20 CRFs have been shown.

Consequently, following propagation of the CRFs from deep brain to the surface of cortex and correlation of them to stimuli can be used as a tool to encode stimuli and decode brain response (Vahidi, 2018) in 3D volume of tissue.

5.3 **Method**

5.3.1 ***Epi-Intra electrodes fabrication and in–vitro characterization***

Recently we have presented a novel technology for transferring glassy carbon microstructures, originally fabricated on a silicon wafer through a high-temperature process, to a polymeric flexible substrate such as polyimide ((Sharma, 2018) and (Vomero, 2017)). This new transfer technique addresses a major barrier in Carbon-MEMS technology whose widespread use has been hampered by the high-temperature pyrolysis process (≥900 °C), which limits selection of

substrates. In this new presented approach, patterning and pyrolysis of polymer precursor on silicon substrate is carried out first, followed by coating with a polymer layer that forms a hydrogen bond with glassy carbon and then releasing the ensuing glassy carbon structure; hence, transferring it to a flexible substrate.

This enables the fabrication of a unique set of glassy carbon microstructures critical in applications that demand substrates that conform to the shape of the stimulated/actuated or sensed surface. Our findings based on Fourier transform infrared spectroscopy on the complete electrode set demonstrate - for the first time - that carbonyl groups on polyimide substrate form a strong hydrogen bond with hydroxyl groups on glassy carbon resulting in carboxylic acid dimers (peaks at 2660 and 2585 cm-1). This strong bond is further confirmed by a tensile test that demonstrated an almost perfect bond between these materials that behave as an ideal composite material. Further, mechanical characterization shows that ultimate strain for such a structure is as high as 15% with yield stress of ~20 MPa. We propose that this novel technology not only offers a compelling case for the widespread use of carbon-MEMS, but also helps move the field in new and exciting directions.

Next step, we integrate the GC sensing sites into 3D origami-styled platform. The detailed fabrication method of the origami-styled 3D integrated intra-cortical and epi-cortical neural probes (Epi-intra) with GC electrode sites is described in detail elsewhere ((Nimbalkar, 2018), (Vomero , 2016)). Here we briefly explain the overall method along with the extra processes which are added to improve performance of these electrode combinations. The Epi-Intra microfabrication process starts by spin-coating SU8 negative photoresist (Microchem, MA) on SiO2 substrate at 1200 rpm for 55 s. The coated substrate is then soft-baked at 65°C for 10 min, 95°C for 20 min, then UV exposed at ~400 mJ cm^{-2} (Figure 5-1a). Further, post-exposure bake was run at 65°C for

1 min and 95°C for 1 min. This was followed by development of SU8 for 3–5 min and curing at 150°C for 30 min (Figure 5-1b). Pyrolysis was done at 1000°C in an inert N_2 environment resulting in GC microelectrodes with high graphitic content (Figure 5-1c). After the pyrolysis step, 6 μm layer of photo-patternable polyimide HD 4100 (Microsystems) was spin-coated on top of GC microelectrodes at 2500 rpms for 45 s, soft baked at 90°C for 3 min and at 120 °C for 3 min, then cooled to room temperature, and patterned through UV exposure at ~400 mJ cm^{-2}. Post-exposure bake consisted of 80°C for 1 min. Development was performed using a spry-puddle process where QZ3501 (Fuji Film, Japan) was dispersed to form a puddle on a stationary wafer. Three rinse steps were applied later with SU8 developer followed by spin-drying of the wafer at 2000 rpm for 15 s with 500 rpm s^{-1} stepping ramp. Subsequently, the polyimide layer was partially cured at 300°C for 60 min in a N_2 environment. An additional thicker layer of polyimide (Durimide 7520) (FujiFilm, Japan) was then patterned on top of the insulation layer to reinforce the penetrating portion of the device (Figure 5-1d). Following this, metal traces were patterned using lift-off process with a sacrificial layer of NR9-1000PY photoresist (Futurrex, Inc). The photoresist was spin-coated at 500 rpm for 45 s and ramped down for 10 s, then prebaked for 2 min at 150 °C followed by 380 mJ cm^{-2} UV exposure. Post exposure bake was done at 100 °C for 2 min and the sample was developed in pure RD6 developer (Futurrex Inc) for 3 s. Afterward, a 20 nm Ti adhesion layer and 200 nm Pt layer were deposited through sputtering (Figure 5-1e). For electrical insulation, an additional 6 μm of polyimide HD4100 (300 rpms) was spun, patterned (400 mJ cm^{-2}), and cured (350°C for 90 min) in a N_2 environment (Figure 5-1f). Additional 30 μm thicker layer of polyimide (Durimide 7520, Fuji Film) was spin-coated (800 rpm, 45 s) and then patterned (400 mJ cm^{-2}) on top of the insulation layer to reinforce the penetrating portion of the device (Figure 5-1g). A final cure was done at 350°C for 90 min. Finally, the device was released from

the wafer through selective etching of silicon dioxide layer with buffered hydrofluoric (BHF) acid (Figure 5-1h). Finally the released device can be formed to a 3D combination of surface array and depth shank (Figure 5-3).

In vitro Epi-Intra device characterization has been reported elsewhere (Vomero, et al., 2017). Overall, optical microscope and scanning electron microscope (SEM) method have been utilized to image uniform distribution of the glassy carbon microelectrodes (GC) before and after device implantation. The capacitive charging ability and electrochemical characterization of GC microelectrodes also were evaluated by cyclic voltammetry (CV) and voltage transient (VTs), and electrochemical impedance spectroscopy (EIS) and compared with its known Pt counterparts. The GC penetrating microelectrodes exhibited lower impedance (3.6 ± 1.2 kΩ at 1 kHz) than their Pt counterparts across the whole frequency range (Goshi, et al., 2018).

Finally, biocompatibility and the mechanical stability of GC electrode sites was monitored by implanting the Epi-Intra device in cultured fibroblasts cells. The results demonstrated the percentage of surviving cells progressively increased after third day of post implant on the culture and remained constant (Vomero, 2017).

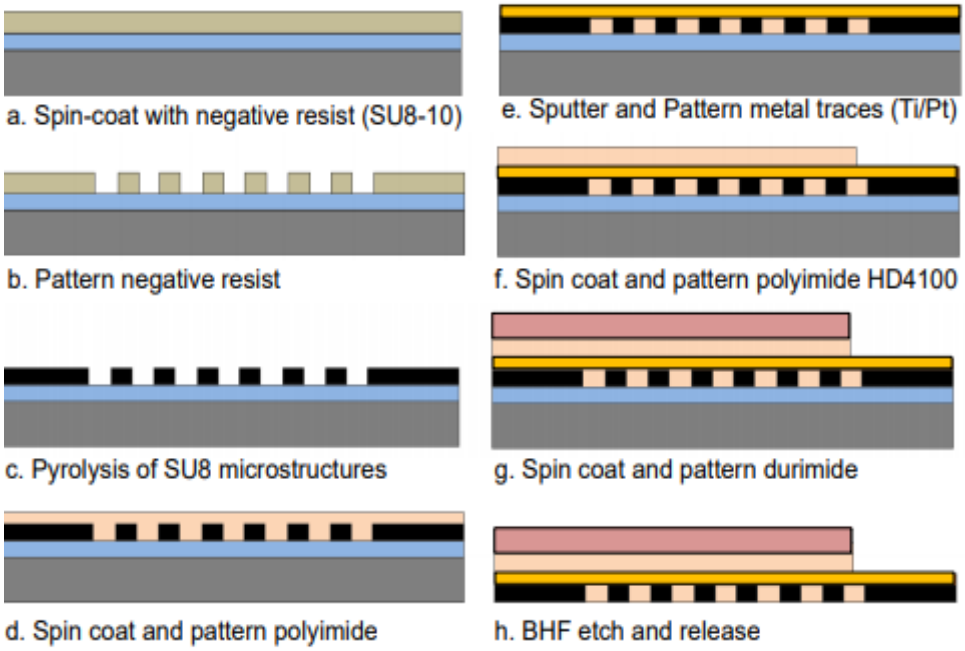

Figure 5-1: Epi-Intra electrode fabrication
(a) Spin-coating SU8 negative photoresist on SiO2 substrate. (b) Patterned photoresist by UV exposure. (c) Pyrolysis photoresist to receive GC microelectrodes. (d) *Patterned* polyimide with additional thicker layer of polyimide to reinforce the penetrating portion of the device. (e) Patterned metal traces. (f) Electrical insulation by polyimide HD4100. (g) Durimide coating to reinforce the depth shank. (h) Released the device from the wafer by buffered hydrofluoric acid (BHF).

5.3.2 *Surgical procedure and electrophysiology*

These experiments were performed on three adult European starling song birds under a protocol approved by the Institutional Animal Care and Use Committee of the University of California, San Diego. Isoflurane and urethane (7–8 ml/kg) have been used to obtain active auditory response while subjects were under anesthesia (Masamoto & Kanno, 2012). Following, subjects were placed in a stereotaxic apparatus inside a sound attenuation chamber. A small craniotomy was made on Caudomedial Nidopallium (NCM) auditory area and the dura was removed. Subsequently, Epi-Intra electrode combinations were advanced into the brain at the coordinate of 500-1000 µm caudal and 500-1000 µm lateral on right side of Y-sinuous. Intra depth

electrode was lowered 2500µm deep until Epi surface array touched and conformed onto the cortex. Following, five starling bird songs were played 20 times randomly for the subjects. The songs were played randomly to prevent stimulus selectivity by subjects (Yaneri & Manuel, 2013). These bird song stimuli were recorded from starling males at 44.1 thousand samples/s and played back for the subjects at 60dB. Figure 5-2 displays this recording paradigm. While bird song stimuli was playing for the anesthetized birds in a sound chamber, the neural data was recorded from eleven channels of Epi-Intra electrodes: Seven channels recorded signals from brain surface and four channels recorded signals from depth brain. The data was amplified by an amplifier system (A-M model 3600) with a gain of 5K, sampling rate of 20 KHz, and then low and high pass filtered respectively at 10HZ and 10KHZ. The recorded data was then converted to Matlab files.

Two control recordings were completed with a 32 channel commercial depth electrode (NeuroNexus A1x32-Edge-10mm-20-177). This depth electrode sites have 20µm spacing with a 177 μm^2 surface area and are made of iridium.

The recorded data then was divided onto two data sets. By filtering data less than 300 Hz, we have received local field optional (LFP) signals and by filtering data above 300 Hz, we have received high frequency data that is used for cell sorting. To extract cells from high frequency data, MountainSort program has been utilized. This program is a clustering algorithm which works with high-dimensional data to sort neuronal cells (Chung, 2017). Following, the clusters containing noise have been disregarded and the sorted neural cells were grouped to single cells and multi-units. The signal processing analysis in this study have been performed in MATLAB software (Mathworks, USA) and python.

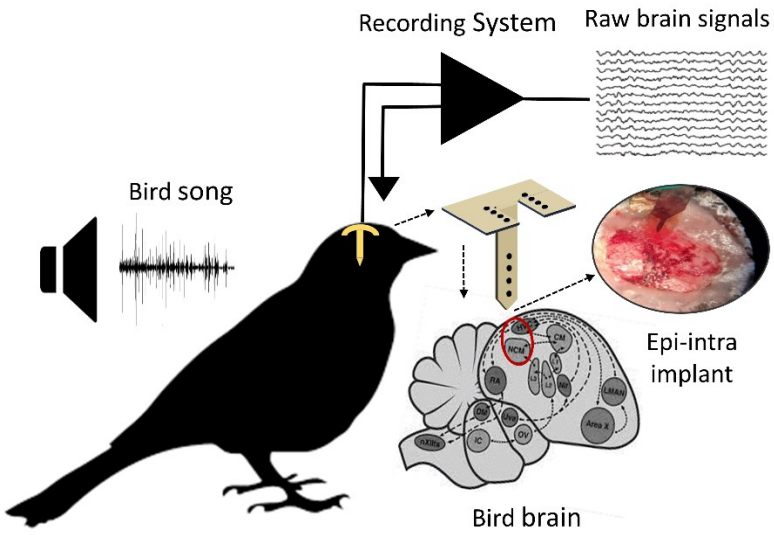

Figure 5-2: Neural recording paradigm by Epi-Intra device.
The bird songs are playing for the starling birds while recording system records from surface (Intra) and depth (Epi) electrodes simultaneously. Recorded channels then are amplified 5K and filtered at 10Hz-10KHz. Location of Epi-Intra implant on brain has been demonstrated here.

5.4 Result

5.4.1 *Epi-Intra electrodes and in-vivo characterizations*

Figure 5-3 displays Epi-Intra electrodes fabricated for this study which has the ability to unfold to combination of a surface ECoG array and a depth laminar shank with total eleven GC recording sites and a reference. Seven GC sites are separated into two parts by the depth shank (Figure 5-3a). The two surface arrays in both sides of depth shank will increase the chance of recording from a broader area of the cortex. Also their combination with the depth shank will cover a 3D volume of brain tissue which is necessary for this study. The intra depth shank contains four GC sensing sites on a reinforced polyimide shank. The depth shank is 3 mm long and 0.5 mm wide. The sites in both arrays have 30 µm diameters with a center to center pitch of 100 µm.

After implanting the Epi-Intra electrodes, in-vivo characterization has been performed.

Optical and scanning electron microscope (SEM) images of the device proved the intact uniform distribution of the glassy carbon microelectrodes during chronic recording (Figure 5-3b).

The GC penetrating microelectrodes did not exhibit a significant change in impedance before or after implantation. In-vivo cyclic voltammetry (CV) and voltage transient (VTs) measured from depth electrode sites have been conducted during neural recording from starling birds. The results demonstrated neurotransmitter sensing such as dopamine with reduction and oxidation of (−0.17 V) and (+0.63 V) peaks respectably.

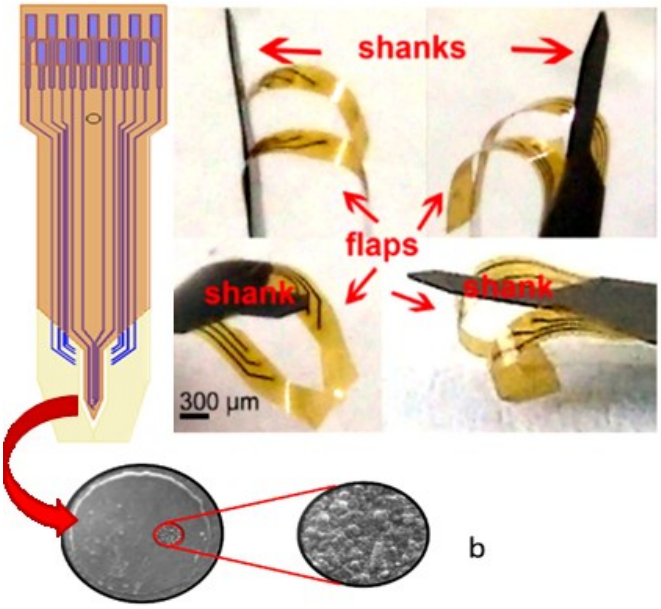

Figure 5-3: Epi-Intra device.
(a) Left: Flat configuration of Epi-Intra device before implanting. Epi surface array contain seven GC sites and one reference site. There are four sites on both right and left side of depth shank. Intra depth shank consists four sites. Right: Unfold configuration of Epi-Intra device ready for implantation. (b) Zoom into a glassy carbon sensing site.

5.4.2 *Statistical analysis of electrical recordings*

Not only the novel properties of GC electrodes have been shown viable for chemical and neurotransmitter detection but furthermore GC electrodes on Epi-Intra device have shown

exceptional electrical recording potential during recording from the auditory area of starling bird brains.

Figure 5-4 displays an example of high pass signals of eleven channels recorded simultaneously from the surface of the brain by the Epi array in red and from deep brain by the Intra shank in blue. On top, a spectrogram of a 15 second bird song is displayed which demonstrates modulation of bird song power over time across twenty frequencies. The color bar next the song spectrogram is indication of the song power intensity.

By analyzing this high pass data we have detected multiple clusters of single cells as well as multi-units. Figure 5-5b demonstrates example waveforms of a few single cells that are recorded by GC electrode sites from surface and deep brain. To differentiate between single cells and multi-units, cells inter spike intervals (ISI) have been calculated. Cells with ISI more than 1-2ms have been categorized as single cells (Dayan & Abbott, 2000). Figure 5-5c displays example of ISI related to two single cell waveforms recorded from deep brain and surface.

Figure 5-5a right and left are two raster plots which belong to the above two single cells. The top rows show a 70s and 75s sonogram, amplitude modulation, of two bird song stimuli. Second rows are a spectrogram of these bird songs with nfft=128 and Hanning window of 128 with 50% overlap. Third rows display 20 trials of spike trains and the fourth rows are the averages of these 20 trials. These plots provide evidence that the cells are significantly stimulus- locked which is an indication they are auditory neurons with minimum noise recorded from both deep brain and cortical surface.

To examine the Epi-Intra3D configuration as a possible tool for neural coding we first attempted to investigate LFP signals' cross-correlation recorded by surface channels and depth channels. Figure 5-6 is demonstrates the correlation matrix between seven surface channels and

four depth channels. Seven Epi and four Intra channels are indicated by red and blue brackets respectively. This correlation matrix demonstrates that although there are high correlation in-between surface Epi channels and in-between Intra depth channels, the correlation is relatively low among surface and depth channels. In fact cross-correlation across channels decrease when distance between channels are more than 1500μm.This finding agrees with other investigations such as ((Destexhe, 1999) & (Bedard, 2004)).

To validate the Epi-Intra device as a tool for neural coding and to overcome the limitations related to cells relative distances and their locations, we purpose investigation of composite receptive fields of neuron cells (CRFs) with this device. In a recent study we have shown that the brain perceives CRF of neurons with uniform distribution, independent of the neurons' location and their topology (Vahidi, 2018).

To extract high quality composite receptive fields from neuron cell responses, the cell responses should be stimulus-locked with low noise ((Kozlov & Gentner, 2016) and (Vahidi, 2018)). Since the recoded cells by Epi-Intra device exhibit such properties, we should be able to extract CRFs from them.

To generate CRFs from the recorded cells, Maximum noise entropy model (MNE) has been adopted ((Fitzgerald, 2011a) & (Kozlov & Gentner, 2016)). This model generates receptive fields from mutual information between neuron cells response and their stimuli. Stimuli spectrogram power density and the neuron cells response average over 20 trials are two inputs of the MNE model. To build stimuli spectrograms power density, first bird songs were down-sampled to 24 KHz, the DC part of signal is removed, and the adjacent 64 frequencies are averaged pairwise twice to receive 16 frequency bands with band ranges of 750Hz-12KHz (Nyquist frequency). Time bins have been down-sampled similar to frequency to extract 20 bins. Following, the power

spectral density (PSD) of the spectrogram is extracted (Figure 5-5a second row). To construct the neuron cell response, an average of 20 trial responses for each cell have been calculated (Figure 5-5a fourth row). These two data sets were then divided to sets of test and train and have been pushed to the MNE logistic model (Equation 5).

Equation 5

$$\mathrm{P(Response|Stimuli)} = \left(1 + \mathrm{e}^{f(s)}\right)^{-1}$$

The polynomial equation $f(s) = (a + h.s + s^T Js)$ has been minimized and parameters a, h, and J have been estimated. Where a, h, and J correspond respectably to the constant, linear part, and quadratic part of receptive field features. The quadratic J contains eigenvalues and eigenvectors. CRFs shown in Figure 5-7a are extracted from a single surface cell and they are built from twenty eigenvectors of J-matrix that are significant. Significant eigenvectors have the highest (positive) or lowest (negative) probability of occurring on the logistic MNE function.
Furthermore, negative and positive eigenvectors correspond to facilitatory and suppressive CRFs successively (Figure 5-7 top and bottom). This analysis was performed on all the stimulus-locked cells for this study and have generated twenty CRFs per cell.

Figure 5-7b displays an Epi-Intra electrode combination with the example of cell waveforms on their recorded sites on the surface array and depth electrode. Next to each waveform, the first extracted receptive field from 20 CRFs is shown.

From this map we can follow propagation of the facilitatory and suppressive CRFs of many cells from deep brain up to the surface of cortex independent from neuron locations in 3D volume of brain tissue. Finally, the control commercial electrodes (NeuroNexus A1x32) and the Epi-Intra device have been compared. The results showed action potential waveforms and their extracted receptive fields recorded from NCM auditory area by both of these recording

devices are comparable.

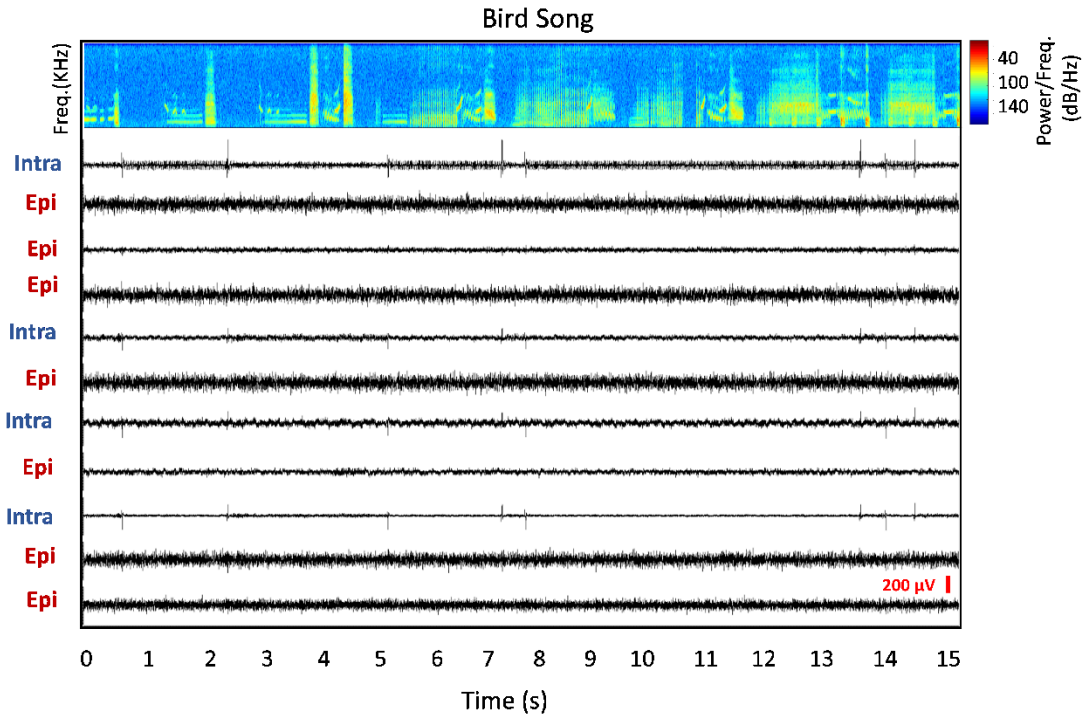

Figure 5-4: Example of high passed data recorded by Epi-Intra electrodes.
Top: Spectrogram of 15 second bird song. The color bar on right indicates power intensity of the song. Bottom: Surface recorded channels are shown in red (Epi) and depth recorded channels are displayed in blue (Intra).

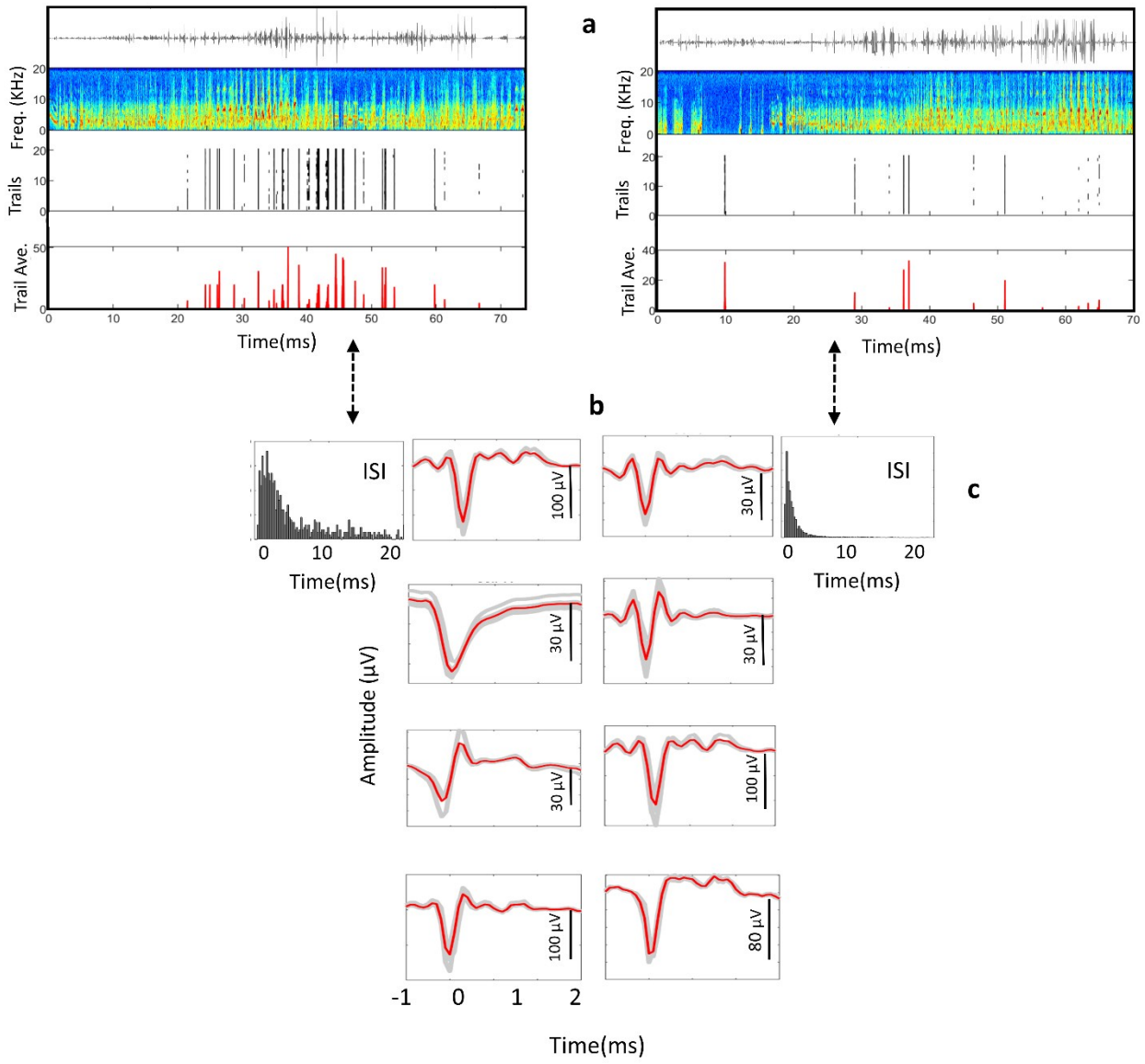

Figure 5-5: Single cells recorded from cortical surface and deep brain by Epi-Intra device. (a) Right: Example of a stimulus-locked single cell recorded from cortical surface. Top row: 75s sonogram of bird song. Second row: Spectrogram of this bird song with nfft=128 and Hanning window of 50% overlap. Third row: Raster plot of 20 trial of spike trains. Forth row: Averages of the 20 trials. Left: Example of a stimulus-locked single cell recorded from deep brain in response to a different 75s bird song. (b) Example of waveforms of a few single cells recorded from surface and deep brain. Each waveform contains twenty spike snippets (light gray). The spike snippets averages have been shown in a red waveforms. Scale of amplitude of waveforms are shown in vertical black bars. (c) Example of ISI of the two single cells. Cells with ISI more than 1-2ms have been categorized as single cells.

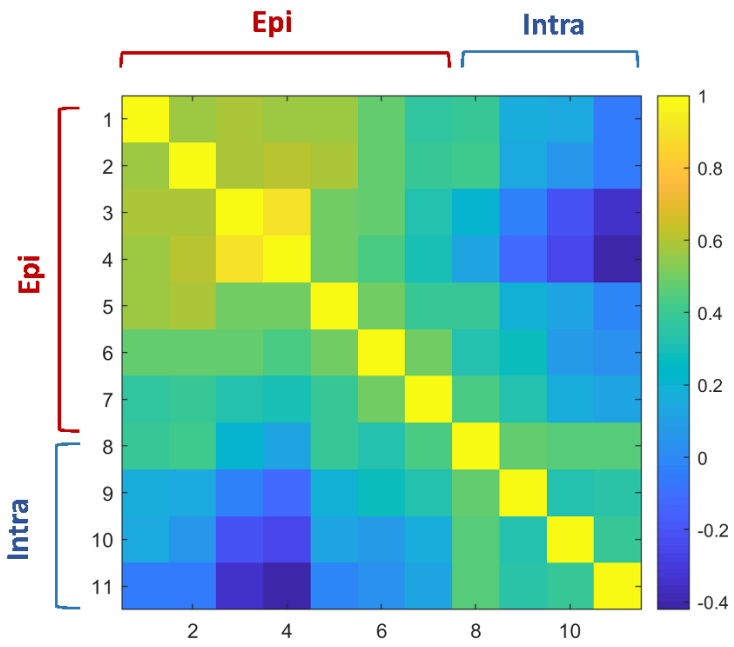

Figure 5-6: Correlations between Epi-Intra LFP signals.
Cross-correlation between low-pass filtered signals (>300Hz) recorded by surface channels and depth channels: Seven Epi and four Intra channels have been pointed by red and blue brackets respectively. The color bar indicates the cross-correlation intensity between channels. This correlation matrix shows high correlation in-between surface LFPs as well as high correlation in-between depth LFPs but low correlation among surface and depth LFPs.

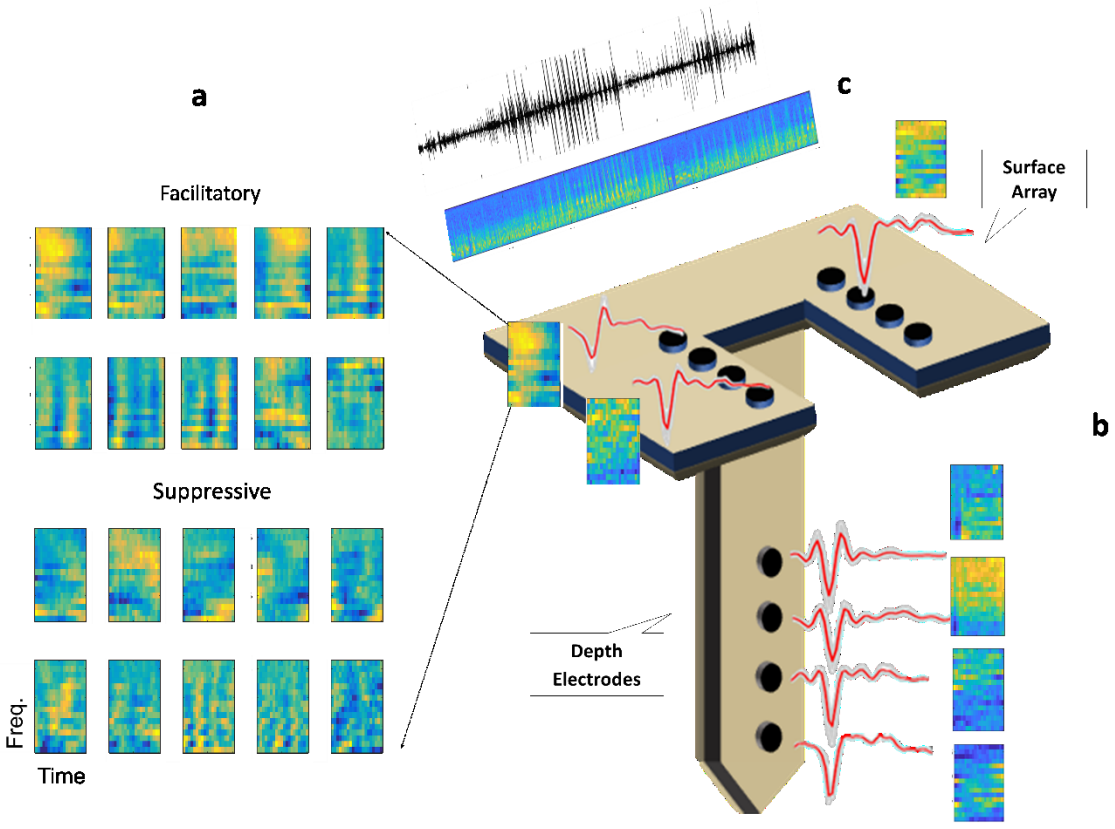

Figure 5-7: Cells and their composite receptive fields mapping on Epi-Intra device.
(a) Example of 20 CRFs extracted from a single surface cell. Top: 10 significant facilitatory CRFs. Bottom: 10 significant suppressive CRFs. (b) Epi-Intra electrode combination with example of cell waveforms assigned on their recorded sites on the surface array and depth shank. Next to each waveform, the first extracted receptive field from 20 CRFs are shown. (c) Sonogram and spectrogram of a bird song stimulus. This CRF map projected on Epi-Intra device can be used as a tool to encode stimuli in 3D volume of tissue.

5.5 Conclusion

Among the cells in our body, neuron cells have the ability to propagate signals rapidly between themselves over large distances. One technique to understand this neuron signal propagation mechanism and their relationship with the stimuli is neural coding ((Brown, 2004), (Johnson, 2000), and (Vahidi, 2018)). In this study we introduce an origami style brain prosthesis device that can unfold to a combination of a surface ECoG array and depth shank during brain

implantation. This 3D style brain recording platform has the ability to cover recordings from a volume of tissue: from deep brain to the cortical surface. The origami nature of the device made it a suitable candidate for studying neural signal propagation and neural coding in 3D volume of brain tissue.

We have named this origami style device “Epi-intra”. The Epi part made of a flexible polyimide polymer that can conform to the cortex curvature while the Intra depth shank has been reinforced for easy brain penetration. The electrochemical sensing sites of Epi-Intra are made of glassy carbon (GC). GC has shown high potential for use in neural applications ((Wang, 2010), (Lin, 2008), (Kassegne, 2012), (Martinez-Duarte, 2011), (Martinez-Duarte, 2010), (Hirabayashi, 2014), and (Vahidi , 2014)). In recent studies we have shown not only the GC sensing sites are chemically inert and biocompatible with low impedance ((Goshi, 2018), (Vomero, 2017)), but also they are able to clearly record neurotransmitters such as dopamine (Castagnola, 2018).

The unique properties of GC electrodes are not only limited to chemical and neurotransmitter sensing, as the GC electrodes on the Epi-Intra device have shown novel electrical recordings in this study while recording from auditory area of starling bird brains. From these recordings we were able to determine LFP signals as well as high quality stimulus-locked auditory single cells from both deep brain and cortical surface.

To investigate the signal propagation mechanism and their relationship with the stimuli, first the correlation between the LFP signals were monitored. The result has shown, although there are high correlation in-between surface Epi channels as well as in-between Intra depth channels, the overall correlation is relatively low among surface and depth channels due to the large distance between cells on the surface and at depth.

To be able to scrutinize the Epi-Intra device as a tool for neural coding and also to overcome the limitations related to cells large distances and their overall topology we have purposed investigation of composite receptive fields of neuron cells. In a recent study we have demonstrated that the brain perceives composite receptive fields of neurons with uniform distribution independent of the neurons' distance, location and, topology (Vahidi, 2018).

The stimulus-locked properties of recorded cells by the Epi-Intra device make them viable candidates for CRFs extraction. Maximum noise entropy model generates CRFs from stimulus-locked neural responses by searching for the highest mutual information between stimuli and the brain response in the form of CRFs ((Fitzgerald, 2011a) & (Kozlov & Gentner, 2016)). By utilizing the MNE model we have extracted CRFs from the cells and subsequently categorized them to facilitatory and suppressive responses. Finally, these facilitatory and suppressive CRFs are mapped to their recording sites on the Epi-Intra device.

From this map we can follow propagation of facilitatory and suppressive CRFs of many cells from deep brain to the surface of the cortex independent of neuron locations in a 3D volume of brain tissue. Consequently, we are suggesting the Epi-Intra device as a tool for future study of stimuli encoding and brain responses decoding in 3D volume of tissue. In addition, this device has a potential for chronic implants and recordings and can be used as BCI prosthetics.

5.6 Acknowledgments

Chapter 5, in full, is in preparation for publication as: Nasim W.Vahidi, Surabhi Nimbalkar, Elisa Castagnola, Srihita Rudraraju, Claudia Cea, Shadi A. Dayeh, Timothy Q. Gentner, and Sam Kassegne. "Epi-Intra device with glossy carbon electrodes: A tool for neural coding". The dissertation author was the primary investigator and author of this manuscript.

5.7 **References**

Ayala, Y. A., & Malmierca, M. S. (2012). Stimulus-specific adaptation and deviance detection in the inferior colliculus. *Frontiers in Neural Circuits*, *6*, 89. https://doi.org/10.3389/fncir.2012.00089

Bédard, C., Kröger, H., & Destexhe, A. (2004). Modeling extracellular field potentials and the frequency-filtering properties of extracellular space. *Biophysical Journal*, *86*(3), 1829–1842. https://doi.org/10.1016/S0006-3495(04)74250-2

Bialek, W., De Ruyter Van Steveninck, R. R., & Tishby, N. (2006). Efficient representation as a design principle for neural coding and computation. *2006 IEEE International Symposium on Information Theory*, 659–663. https://doi.org/10.1109/ISIT.2006.261867

Blackwell, J. M., Taillefumier, T. O., Natan, R. G., Carruthers, I. M., Magnasco, M. O., & Geffen, M. N. (2016). Stable encoding of sounds over a broad range of statistical parameters in the auditory cortex. *European Journal of Neuroscience*, *43*(6), 751–764. https://doi.org/10.1111/ejn.13144

Brown, E. N., Kass, R. E., & Mitra, P. P. (2004). Multiple neural spike train data analysis: state-of-the-art and future challenges. *Nature Neuroscience*, *7*(5), 456–461. https://doi.org/10.1038/nn1228

Castagnola, E., Winchester Vahidi, N., Nimbalkar, S., Rudraraju, S., Thielk, M., Zucchini, E., Kassegne, S. (2018). In Vivo Dopamine Detection and Single Unit Recordings Using Intracortical Glassy Carbon Microelectrode Arrays. *MRS Advances*, *3*(29), 1629–1634. https://doi.org/10.1557/adv.2018.98

Chung, J. E., Magland, J. F., Barnett, A. H., Tolosa, V. M., Tooker, A. C., Lee, K. Y., Greengard, L. F. (2017). A Fully Automated Approach to Spike Sorting. *Neuron*, *95*(6), 1381–1394.e6. https://doi.org/10.1016/j.neuron.2017.08.030

De Boer, R., & Kuyper, P. (1968). Triggered correlation. *IEEE Transactions on Bio-Medical Engineering*, *15*(3), 169–179. Retrieved from http://www.ncbi.nlm.nih.gov/pubmed/5667803

Destexhe, A., Contreras, D., & Steriade, M. (1999). Spatiotemporal analysis of local field potentials and unit discharges in cat cerebral cortex during natural wake and sleep states. *The Journal of Neuroscience : The Official Journal of the Society for Neuroscience*, *19*(11), 4595–4608. Retrieved from http://www.ncbi.nlm.nih.gov/pubmed/10341257

Eggermont, J. J., Epping, W. J. M., & Aertsen, A. M. H. J. (1983). Stimulus dependent neural correlations in the auditory midbrain of the grassfrog (Rana temporaria L.). *Biological Cybernetics*, *47*(2), 103–117. https://doi.org/10.1007/BF00337084

Ester, M., Kriegel, H.-P., Sander, J., & Xu, X. (1996). *A Density-Based Algorithm for Discovering Clusters in Large Spatial Databases with Noise*. Retrieved from www.aaai.org

Fitzgerald, J. D., Rowekamp, R. J., Sincich, L. C., & Sharpee, T. O. (2011). Second Order Dimensionality Reduction Using Minimum and Maximum Mutual Information Models. *PLoS Computational Biology*, *7*(10), e1002249. https://doi.org/10.1371/JOURNAL.PCBI.1002249

Fitzgerald, J. D., Sincich, L. C., & Sharpee, T. O. (2011). Minimal Models of Multidimensional Computations. *PLoS Computational Biology*, *7*(3), e1001111. https://doi.org/10.1371/journal.pcbi.1001111

Goshi, N., Castagnola, E., Vomero, M., Gueli, C., Cea, C., Zucchini, E., Fadiga, L. (2018). Glassy carbon MEMS for novel origami-styled 3D integrated intracortical and epicortical neural probes. *Journal of Micromechanics and Microengineering*, *28*(6), 065009. https://doi.org/10.1088/1361-6439/aab061

Harris, K. D., & Woolley, S. (2015). Cortical computation in mammals and birds. *Proceedings of the National Academy of Sciences of the United States of America*, *112*(11), 3184–3185. https://doi.org/10.1073/pnas.1502209112

Hirabayashi, M., Mehta, B., Nguyen, B., & Kassegne, S. (2015). DNA immobilization on high aspect ratio glassy carbon (GC-MEMS) microelectrodes for bionanoelectronics applications. *Microsystem Technologies*, *21*(11), 2359–2365. https://doi.org/10.1007/s00542-014-2332-3

Institute of Physics (Great Britain), S., Moon, K., Martín-Ramos, P., Majzoub, M., Őzturk, G., Desai, K., … Chamorro-Posada, P. (1990). Journal of micromechanics and microengineering. In *Journal of Micromechanics and Microengineering* (Vol. 22). Retrieved from https://www.academia.edu/13456424/Organic_MEMS_NEMS-based_high-efficiency_3D_ITO-less_flexible_photovoltaic_cells

Johnson, A., & Proctor, R. W. (2004). *Attention : theory and practice*. Sage Publications.

Kaardal, J. T., Theunissen, F. E., & Sharpee, T. O. (2017). A Low-Rank Method for Characterizing High-Level Neural Computations. *Frontiers in Computational Neuroscience*, *11*, 68. https://doi.org/10.3389/fncom.2017.00068

Karten, H. J. (2013). Neocortical Evolution: Neuronal Circuits Arise Independently of Lamination. *Current Biology*, *23*(1), R12–R15. https://doi.org/10.1016/j.cub.2012.11.013

Kozlov, A. S., & Gentner, T. Q. (2016). Central auditory neurons have composite receptive fields. *Proceedings of the National Academy of Sciences*, *113*(5), 1441–1446. https://doi.org/10.1073/pnas.1506903113

Lin, P.-C., Park, B. Y., & Madou, M. J. (2008). Development and characterization of a miniature PEM fuel cell stack with carbon bipolar plates. *Journal of Power Sources*, *176*(1), 207–214. https://doi.org/10.1016/j.jpowsour.2007.10.079

Maaten, L. van der, & Hinton, G. (2008). Visualizing Data using t-SNE. *Journal of Machine Learning Research*, *9*(Nov), 2579–2605. Retrieved from http://www.jmlr.org/papers/v9/vandermaaten08a.html

Martinez-Duarte, R., Gorkin III, R. A., Abi-Samra, K., & Madou, M. J. (2010). The integration of 3D carbon-electrode dielectrophoresis on a CD-like centrifugal microfluidic platform. *Lab on a Chip*, *10*(8), 1030. https://doi.org/10.1039/b925456k

Martinez-Duarte, R., Renaud, P., & Madou, M. J. (2011). A novel approach to dielectrophoresis using carbon electrodes. *ELECTROPHORESIS*, *32*(17), n/a-n/a. https://doi.org/10.1002/elps.201100059

Masamoto, K., & Kanno, I. (2012). Anesthesia and the Quantitative Evaluation of Neurovascular Coupling. *Journal of Cerebral Blood Flow & Metabolism*, *32*(7), 1233–1247. https://doi.org/10.1038/jcbfm.2012.50

Nimbalkar, S., Castagnola, E., Balasubramani, A., Scarpellini, A., Samejima, S., Khorasani, A., Kassegne, S. (2018). Ultra-Capacitive Carbon Neural Probe Allows Simultaneous Long-Term Electrical Stimulations and High-Resolution Neurotransmitter Detection. *Scientific Reports*, *8*(1), 6958. https://doi.org/10.1038/s41598-018-25198-x

Rossant, C., Kadir, S. N., Goodman, D. F. M., Schulman, J., Hunter, M. L. D., Saleem, A. B., Harris, K. D. (2016). Spike sorting for large, dense electrode arrays. *Nature Neuroscience*, *19*(4), 634–641. https://doi.org/10.1038/nn.4268

Schwartz, O., Chichilnisky, E. J., & Simoncelli, E. P. (2018). Characterizing neural gain control using spike-triggered covariance. *Advances in Neural Information Processing Systems 14*, pp. 269–276. https://doi.org/10.7551/mitpress/1120.003.0039

Schwartz, O., Pillow, J. W., Rust, N. C., & Simoncelli, E. P. (2006). Spike-triggered neural characterization. *Journal of Vision*, *6*(4), 13. https://doi.org/10.1167/6.4.13

Sharma, S., Sharma, & Swati. (2018). Glassy Carbon: A Promising Material for Micro- and Nanomanufacturing. *Materials*, *11*(10), 1857. https://doi.org/10.3390/ma11101857

Sharpee, T., Rust, N. C., & Bialek, W. (2004). Analyzing Neural Responses to Natural Signals: Maximally Informative Dimensions. *Neural Computation*, *16*(2), 223–250. https://doi.org/10.1162/089976604322742010

Theunissen, F. E., Sen, K., & Doupe, A. J. (2000). Spectral-temporal receptive fields of nonlinear auditory neurons obtained using natural sounds. *The Journal of Neuroscience :*

The Official Journal of the Society for Neuroscience, *20*(6), 2315–2331. Retrieved from http://www.ncbi.nlm.nih.gov/pubmed/10704507

Vahidi, N. W., Hirabayashi, M., Mehta, B., Rayatparvar, M., Wibowo, D., Ramesh, V., … Kassegne, S. (2014). Bionanoelectronics Platform with DNA Molecular Wires Attached to High Aspect-Ratio 3D Metal Microelectrodes. *ECS Journal of Solid State Science and Technology*, *3*(3), Q29–Q36. https://doi.org/10.1149/2.001403jss

Vahidi, N. W., Thielk, M., Gentner, Q.T. (2018). Composite receptive fields across neuronal populations in songbird auditory cortex. *Neuroscience Meeting Planner* (p. 394.30/EE4). San Diego, CA: Society for Neuroscience.

Vomero, M., Castagnola, E., Ciarpella, F., Maggiolini, E., Goshi, N., Zucchini, E., Ricci, D. (2017). Highly Stable Glassy Carbon Interfaces for Long-Term Neural Stimulation and Low-Noise Recording of Brain Activity. *Scientific Reports*, *7*(1), 40332. https://doi.org/10.1038/srep40332

Vomero, M., van Niekerk, P., Nguyen, V., Gong, N., Hirabayashi, M., Cinopri, A., Kassegne, S. (2016). A novel pattern transfer technique for mounting glassy carbon microelectrodes on polymeric flexible substrates. *Journal of Micromechanics and Microengineering*, *26*(2), 025018. https://doi.org/10.1088/0960-1317/26/2/025018

Wang, Y., Pham, L., Salerno De Vasconcellos, P., & Madou, M. (2010). Fabrication and characterization of micro PEM fuel cells using pyrolyzed carbon current collector plates. *Journal of Power Sources*, *195*, 4796–4803. https://doi.org/10.1016/j.jpowsour.2010.02.050

CHAPTER 6

Conclusion and Discussion to the Dissertation

Among the cells in our body, neuron cells have the ability to propagate signals rapidly between themselves over large distances. One technique to understand these neurons signal propagation mechanism and their relationship with the stimuli is population neural coding ((Brown, 2004) & (Johnson, 2000)). Neural Population coding is a technique to process populations of neurons responses to input stimuli. Each individual neuron has a unique distribution of output in response to input stimuli however studies have shown that it is the combination of neuron responses, in a population, that carry the most amount of information about the input stimuli ((Wu, 2002) , (Rieke, 1997), and (Machens, 2004)). Although studies have been done in this area still we lack the tools to comprehend the population coding mechanism (Yildiz, 2016) & (Badel, 2008). Recently, we have shown that neurons in secondary auditory cortical regions of European starling song birds have composite receptive fields (CRF) (Kozlov & Gentner, 2016).

In this study we investigated neural population encoding and decoding by CRFs for the first time. To begin, we have generated a population of 3080 CRFs from 154 cells recorded from the auditory brain region of European starling songbirds. To generate CRFs from neuron cells, Maximum noise entropy model (MNE) has been adopted (Fitzgerald., 2011a). The MNE quadratic model has proved most effective compared with some of the existing models such as STA, STC, and MID ((Bialek , 2005), (Steveninck, 1988), and (Sharpee, 2004)). The MNE model does not have a limitation working with natural stimuli and can extract a large number of receptive field features from cell responses ((Sharpee, 2004) & (Kell, 2018)).

To investigate the decoding and encoding mechanism active in a population of cells, first a spatial-temporal map was created from 154 cells and their 3080 assembled CRFs along the coronal depth plane of the subject brains in respect to bird song stimuli. This spatial-temporal map revealed novel information such as: 1) natural bird song can be encoded by populations of neurons.

2) Number of cells needed to encode the stimulus can be quantified. 3) This encoding mechanism and subsequently perception of sound by the brain appeared to be uniform and independent of cell locations. 4) Through this map, connectivity between cells as well as their plasticity in response to diverse stimuli can be obtained. 5) Furthermore, in this study, we demonstrated CRFs can be utilized as intermediate tools to reconstruct stimuli and predict brain responses.

Investigation of spatial-temporal maps of CRFs from cells recorded from the deep brain inspired us to further scrutinize neural coding and propagation and distribution mechanisms of CRFs on the brain surface. To be able to record high quality stimulus-locked cells from cortical surface, we have introduced a novel ECOG array which is made of a highly flexible parylene substrate with recording sites made of platinum nanoscale rods (PtNR). PtNRs are biocompatible and robust. Thin PtNRs microelectrode arrays implanted on the cortical surface have shown that they are capable of recording high quality neural data from cortical surface such as LFP, single cells, multi-units, and composite receptive fields. Thus, ECOG PtNR arrays can be used as a potential tool to create a 2D CRFs spatial-temporal map on the cortical surface to investigate neural coding and information distribution mechanisms on the brain surface.

In the past two experiments we demonstrate neural coding by depth shank and surface arrays independently. In our third experiment we attempted to combine the surface and depth electrodes in one device (Epi-Intra). This novel origami style device contains a polyimide flexible surface array and reinforced depth shank which unfold during implantation in the brain. The recording sites on surface array and depth shank are homogenous and made of glassy carbon (GC). GC sites are inert, biocompatible, and offer low impedance ((Vomero, 2017) & (Goshi, 2018)). Electrical recordings from this device demonstrated its' potential to record high quality LFP, single, and multi-unit stimulus-locked cells from both cortical surface and deep brain

simultaneously. Furthermore, in this study we have demonstrated the GC sites not only have unique potential to record high quality signals from bird brains but also are able to clearly record neurotransmitters such as dopamine (Castagnola, 2018). The pool of CRFs extracted from these stimulus-locked cells can be used in a future study to create a 3D spatial-temporal map that encompasses a volume of tissue from cortical surface to deep brain.

Overall, in this study, we have introduced composite receptive fields as a new computational tool for neural coding and investigation of brain information distribution mechanisms. Applying this computational tool to brain signals recorded via devices such as PtNR surface arrays and Epi-Intra combinations will not only expand our knowledge of neural coding, neural information distribution, and perception mechanism from deep brain to cortical surface, but also for possible application as BCI prosthetics.

6.1 References

Badel, L., Lefort, S., Berger, T. K., Petersen, C. C. H., Gerstner, W., & Richardson, M. J. E. (2008). Extracting non-linear integrate-and-fire models from experimental data using dynamic I–V curves. *Biological Cybernetics*, *99*(4–5), 361–370. https://doi.org/10.1007/s00422-008-0259-4

Bialek, W., & van Steveninck, R. R. de R. (2005). *Features and dimensions: Motion estimation in fly vision*. Retrieved from http://arxiv.org/abs/q-bio/0505003

Brown, E. N., Kass, R. E., & Mitra, P. P. (2004). Multiple neural spike train data analysis: state-of-the-art and future challenges. *Nature Neuroscience*, *7*(5), 456–461. https://doi.org/10.1038/nn1228

Castagnola, E., Winchester Vahidi, N., Nimbalkar, S., Rudraraju, S., Thielk, M., Zucchini, E., Kassegne, S. (2018). In Vivo Dopamine Detection and Single Unit Recordings Using Intracortical Glassy Carbon Microelectrode Arrays. *MRS Advances*, *3*(29), 1629–1634. https://doi.org/10.1557/adv.2018.98

Ester, M., Kriegel, H.-P., Sander, J., & Xu, X. (1996). *A Density-Based Algorithm for Discovering Clusters in Large Spatial Databases with Noise*. Retrieved from www.aaai.org

Fitzgerald, J. D., Rowekamp, R. J., Sincich, L. C., & Sharpee, T. O. (2011). Second Order Dimensionality Reduction Using Minimum and Maximum Mutual Information Models. *PLoS Computational Biology*, *7*(10), e1002249. https://doi.org/10.1371/JOURNAL.PCBI.1002249

Goshi, N., Castagnola, E., Vomero, M., Gueli, C., Cea, C., Zucchini, E., Fadiga, L. (2018). Glassy carbon MEMS for novel origami-styled 3D integrated intracortical and epicortical neural probes. *Journal of Micromechanics and Microengineering*, *28*(6), 065009. https://doi.org/10.1088/1361-6439/aab061

James, W., Burkhardt, F., Bowers, F., & Skrupskelis, I. K. (1981). *The principles of psychology*. Harvard University Press.

Johnson, A., & Proctor, R. W. (2004). *Attention : theory and practice*. Sage Publications.

Kell, A. J. E., Yamins, D. L. K., Shook, E. N., Norman-Haignere, S. V, & Mcdermott, J. H. (n.d.). *A Task-Optimized Neural Network Replicates Human Auditory Behavior, Predicts Brain Responses, and Reveals a Cortical Processing Hierarchy In Brief*. https://doi.org/10.1016/j.neuron.2018.03.044

Kozlov, A. S., & Gentner, T. Q. (2016). Central auditory neurons have composite receptive fields. *Proceedings of the National Academy of Sciences*, *113*(5), 1441–1446. https://doi.org/10.1073/pnas.1506903113

Maaten, L. van der, & Hinton, G. (2008). Visualizing Data using t-SNE. *Journal of Machine Learning Research*, *9*(Nov), 2579–2605. Retrieved from http://www.jmlr.org/papers/v9/vandermaaten08a.html

Machens, C. K., Wehr, M. S., & Zador, A. M. (2004). Linearity of Cortical Receptive Fields Measured with Natural Sounds. *Journal of Neuroscience*, *24*(5), 1089–1100. https://doi.org/10.1523/JNEUROSCI.4445-03.2004

Pascual-Leone, A., Amedi, A., Fregni, F., & Merabet, L. B. (2005). THE PLASTIC HUMAN BRAIN CORTEX. *Annual Review of Neuroscience*, *28*(1), 377–401. https://doi.org/10.1146/annurev.neuro.27.070203.144216

Rieke, F., Bodnar, D. A., & Bialek, W. (1995). Naturalistic stimuli increase the rate and efficiency of information transmission by primary auditory afferents. *Proceedings of the Royal Society of London. Series B: Biological Sciences*, *262*(1365), 259–265. https://doi.org/10.1098/rspb.1995.0204

Rieke, F. (1997). *Spikes : exploring the neural code*. MIT Press.

Sharpee, T., Rust, N. C., & Bialek, W. (2004). Analyzing Neural Responses to Natural Signals: Maximally Informative Dimensions. *Neural Computation*, *16*(2), 223–250. https://doi.org/10.1162/089976604322742010

Steveninck, R. B. (1988). Real-time performance of a movement-sensitive neuron in the blowfly visual system: coding and information transfer in short spike sequences. *Proceedings of the Royal Society of London. Series B. Biological Sciences*, *234*(1277), 379–414. https://doi.org/10.1098/rspb.1988.0055

Vahidi, N. W., Hirabayashi, M., Mehta, B., Rayatparvar, M., Wibowo, D., Ramesh, V., … Kassegne, S. (2014). Bionanoelectronics Platform with DNA Molecular Wires Attached to High Aspect-Ratio 3D Metal Microelectrodes. *ECS Journal of Solid State Science and Technology*, *3*(3), Q29–Q36. https://doi.org/10.1149/2.001403jss

Vahidi, N. W., Thielk, M., Gentner, Q.T. (2018). Composite receptive fields across neuronal populations in songbird auditory cortex. *Neuroscience Meeting Planner* (p. 394.30/EE4). San Diego, CA: Society for Neuroscience.

Vomero, M., Castagnola, E., Ciarpella, F., Maggiolini, E., Goshi, N., Zucchini, E., Ricci, D. (2017). Highly Stable Glassy Carbon Interfaces for Long-Term Neural Stimulation and Low-Noise Recording of Brain Activity. *Scientific Reports*, *7*(1), 40332. https://doi.org/10.1038/srep40332

Wu, S., Amari, S., & Nakahara, H. (2002). Population Coding and Decoding in a Neural Field: A Computational Study. *Neural Computation*, *14*(5), 999–1026. https://doi.org/10.1162/089976602753633367

Yildiz, I. B., Mesgarani, N., & Deneve, S. (2016). Predictive Ensemble Decoding of Acoustical Features Explains Context-Dependent Receptive Fields. *The Journal of Neuroscience*, *36*(49), 12338–12350. https://doi.org/10.1523/JNEUROSCI.4648-15.2016